UNIVERSITY OF OKLAHOMA

GRADUATE COLLEGE

AN EVALUATION OF RADAR- AND SATELLITE-DATA BASED PRODUCTS TO DISCRIMINATE BETWEEN TORNADIC AND NON-TORNADIC STORMS

A THESIS

SUBMITTED TO THE GRADUATE FACULTY

in partial fulfillment of the requirements for the

Degree of

MASTER OF SCIENCE IN METEOROLOGY

By

THEA N. SANDMAEL
Norman, Oklahoma
2017

Downloaded from SHAREOK. Persistent Handle URL: https://hdl.handle.net/11244/52775

AN EVALUATION OF RADAR- AND SATELLITE-DATA BASED PRODUCTS TO DISCRIMINATE BETWEEN TORNADIC AND NON-TORNADIC STORMS

A THESIS APPROVED FOR THE
SCHOOL OF METEOROLOGY

BY

Dr. Cameron Homeyer, Chair

Dr. Alan Shapiro

Dr. Corey Potvin

© Copyright by THEA N. SANDMAEL 2017
All Rights Reserved.

Acknowledgments

First of all, I would like to thank, from the bottom of my heart, the most amazing advisor the world has ever seen, Dr. Cameron Homeyer, who put me on the path of fulfilling my research life goals at the very beginning of my research career. I am very grateful that Dr. Homeyer decided to let me join his graduate student group, a group I consider to be my family away from home. Although I did not know Dr. Homeyer when he first approached me with a potential research assistantship, he has proved to be the perfect fit for an advisor. He has always been available to help and guide me through this project, or supporting me when I have needed a confidence boost. I am happy I got the chance to work with Dr. Homeyer, and I believe that any student would be lucky to work with him.

Further, I would like to thank all the wonderful people that I have been working with on this project for the past two years; Kristopher Bedka, Jason Apke, and John Mecikalski. Going in, I was pretty clueless about satellite observations beyond the very basics, but after several teleconferences and email exchanges with these people my knowledge has expanded quite a bit. The newest addition to our team, Elisa Murillo, has provided valuable research discussions and has become a great friend of mine.

I am also grateful to the rest of the tripp-C group – current and past members. You have all been willing to help with anything from coding to moral support when I was a new and confused graduate student. Grad school would not have been as fun without you guys.

I would also like to thank Dr. Harold Brooks for his helpful input on tornado warnings, and the evaluation and visualization of our objective short-term forecasts for tornadoes.

I would like to thank Dr. Alan Shapiro and Dr. Corey Potvin for agreeing to serve on my Master's committee. I have valued their inputs and perspective.

I would like to thank the country of Norway, my home, for the continued financial support to go to college in a foreign country, and also the United States of America for letting me come here.

Lastly, I would like to thank my beautiful and amazing family. Six years ago I left everyone and everything I have ever known to go the other side of the world to attend the University of Oklahoma's meteorology program. I have been determined to follow my dreams, and am forever grateful to my family, especially mamma and pappa, for the support to make this possible. Last, but not least, I would like to thank my "new" little Norwegian-American family, Daenerys and Michael. Daenerys has made my life complete, and I would like to thank her for being a wonderful baby, almost sleeping through the night from the very start, which made life a lot easier for two studying parents. She is growing into a independent, smart, funny, weird, and beautiful girl (thanks, Michael!) that I would do anything for. Michael is the love of my life and is the best husband I could ask for. I am thankful he eventually gave in to my advances and made me the happiest girl alive. I love them both with all of my heart.

Table of Contents

Acknowledgments **iv**

List of Tables **viii**

List of Figures **ix**

Abstract **xiii**

1 Introduction **1**

1.1 Motivation 1

1.2 Evolution of Tornadic Storms and Tornadoes 3

1.3 Radar and Satellite Observations of Tornadic Storms 5

2 Data and Methods **8**

2.1 Cases 8

2.2 Radar 11

2.3 Satellite 16

2.4 Lightning 26

2.5 NARR 26

2.6 Warnings 27

2.7 Tornado Reports 27

2.8 Supercell Classification 28

3 Results and Discussion **30**

3.1 Tornadic vs. Non-Tornadic Storms 32

3.1.1 Supercells and Non-Supercells 47

3.2 Evaluation of a Simple Objective Short-Term Forecast Product . . . 56

3.3 Super Outbreak of April 2011 61

3.4 Tornado Strength 64

4 Summary and Conclusions **75**

Reference List **78**

List of Tables

2.1 Overview of cases. 9

3.1 Number of data points per box for box plots in Sections 3.1-3.3. . . 31

3.2 Values of the performance metrics shown in Figures 3.36 and 3.40. NWS values are in parentheses. 59

3.3 Number of data points per box in box plots for tornado strength. . 65

List of Figures

2.1 Domains for all cases. 10

2.2 Storm tracks of at least 30 minutes in length from all 28 cases. Variation in color is arbitrary and meant to improve interpretation of overlapping storms. 16

2.3 Parallax correction illustration. 22

2.4 Parallax correction example for 11 May 2014 at 2300 UTC. The infrared brightness temperature is shaded by the scale below the plots. The magenta contours represent 5-dBZ echo-top altitudes greater than 13 km (thin lines) and 15 km (thick lines). 24

2.5 As in Figure 2.4, but for 12 June 2013 at 1940 UTC. 25

3.1 Box plot for maximum upper-level radar divergence. 33

3.2 Box plot for maximum upper-level satellite divergence. 34

3.3 Box plot for maximum low-level radar convergence. 34

3.4 Box plot for maximum upper-level radar divergence assuming an anelastic atmosphere. 35

3.5 Box plot for maximum upper-level satellite divergence assuming an anelastic atmosphere. 36

3.6 Box plot for maximum low-level radar convergence assuming an anelastic atmosphere. 36

3.7 Box plot for maximum 40-dBZ echo-top altitude from radar. 37

3.8 Box plot for relationship between visible texture rating and 10-dBZ tropopause-relative echo-top altitudes. Numbers at the base of each box and whisker show the total number of 1-min observations contributing to the distribution. 38
3.9 Box plot for maximum visible texture rating from satellite. 39
3.10 Box plot for minimum tropopause-relative IR brightness temperature from satellite. 39
3.11 Box plot for maximum upper-level radar rotation. 40
3.12 Box plot for maximum mid-level radar rotation. 40
3.13 Box plot for maximum low-level radar rotation. 41
3.14 Box plot for maximum ENTLN total lightning flash density. 42
3.15 Box plot for maximum column maximum spectrum width. 43
3.16 Box plot for maximum implied ascent. 43
3.17 Box plot for median implied ascent. 44
3.18 Box plot for area of implied ascent ≥ 10 m s^{-1}. 45
3.19 Box plot for minimum correlation coefficient. 45
3.20 Box plot for minimum differential reflectivity. 46
3.21 Box plot for maximum upper-level radar divergence for supercells and non-supercells. 48
3.22 Box plot for maximum low-level radar convergence for supercells and non-supercells. 49
3.23 Box plot for maximum 40-dBZ echo-top altitude for supercells and non-supercells. 49
3.24 Box plot for maximum column maximum spectrum width for supercells and non-supercells. 50
3.25 Box plot for maximum upper-level radar rotation for supercells and non-supercells. 50

3.26 Box plot for maximum mid-level radar rotation for supercells and non-supercells. 51
3.27 Box plot for maximum low-level radar rotation for supercells and non-supercells. 51
3.28 Box plot for maximum implied ascent for supercells and non-supercells. 52
3.29 Box plot for median implied ascent for supercells and non-supercells. 52
3.30 Box plot for maximum visible texture rating from satellite for supercells and non-supercells. 53
3.31 Box plot for minimum tropopause-relative IR brightness temperature from satellite for supercells and non-supercells. 53
3.32 Box plot for area of implied ascent $\geq$ 10 m s^{-1} for supercells and non-supercells. 54
3.33 Box plot for minimum correlation coefficient for supercells and non-supercells. 55
3.34 Box plot for minimum differential reflectivity for supercells and non-supercells. 55
3.35 Box plot for radar-derived upper-level divergence-rotation product. 57
3.36 Performance diagrams. 58
3.37 Box plot for maximum upper-level radar divergence for the Super Outbreak of April 2011. 62
3.38 Box plot for maximum upper-level radar rotation for the Super Outbreak of April 2011. 62
3.39 Box plot for divergence-rotation product for the Super Outbreak of April 2011. 63
3.40 Performance diagram for the Super Outbreak of April 2011. 63
3.41 Tornado strength box plot for maximum upper-level radar divergence. 66

3.42 Tornado strength box plot for maximum upper-level radar divergence, supercells only. 66
3.43 Tornado strength box plot for maximum low-level radar convergence. 67
3.44 Tornado strength box plot for maximum 40-dBZ echo-top altitude. 68
3.45 Tornado strength box plot for maximum 40-dBZ echo-top altitude, supercells only. 68
3.46 Tornado strength box plot for column-maximum spectrum width. . 69
3.47 Tornado strength box plot for maximum implied ascent from divergence. 70
3.48 Tornado strength box plot for median implied ascent from divergence. 70
3.49 Tornado strength box plot for area of implied ascent $\geq$ 10 m s^{-1} from divergence. 71
3.50 Tornado strength box plot for upper-level rotation from radar. . . . 72
3.51 Tornado strength box plot for mid-level rotation from radar. 73
3.52 Tornado strength box plot for low-level rotation from radar. 73
3.53 Tornado strength box plot for correlation coefficient. 74

4.1 Covariation of effective bulk wind shear and CAPE-estimated maximum vertical motion for tornadic and non-tornadic storms. 76

Abstract

Severe weather, and specifically tornadoes, can pose a significant threat to property and human life. Tornadic storms have been extensively studied using radar observations for decades, and some more recent studies have started to incorporate satellite-derived variables when investigating thunderstorms. In preparation for GOES-16 operations, characterized by increased temporal and spatial resolution over existing geostationary satellite imagery, a dataset of several thousand storms are analyzed using NEXRAD WSR-88D radar observations and 1-minute super-rapid scan GOES-14 observations from cases during 2011-2016. Radar-based storm tracks and parallax corrections (applied to GOES imagery) are used in order to facilitate detailed storm-based comparisons between the datasets, and to link individual storms to tornado reports from the National Centers for Environmental Information.

The goal of this study is to determine if tornadic storms exhibit any distinguishing features from non-tornadic storms in this combined dataset, and how far in advance of a tornado the data would display any distinctive characteristics. The variables examined include dynamical variables such as rotation and divergence (radar and satellite), implied ascent from single-Doppler radar winds, polarimetric radar signatures, and overshooting tops (radar and satellite). The project incorporates statistical methods for analysis. The data is partitioned into storm populations and modes based on linkages with observed tornadoes and distinct physical and/or dynamical characteristics. Assessments of convective updraft characteristics from the radar and satellite datasets are strong discriminators for

tornadic and non-tornadic storms. The data also exhibits differences for separate tornado intensities, where the storms that produce stronger tornadoes on the Enhanced Fujita scale have stronger updrafts during the tornadoes.

The results were tested with a simple, objective threshold method and compared to the National Weather Service's tornado warnings for the same storms, which resulted in higher probability of detection and lead time at a comparable false alarm ratio and skill for the objective method. A more sophisticated method of utilizing these results could be incorporated into nowcasting algorithms in order to improve lead time for tornadoes or increase the confidence of a tornado being present when observations are limited.

Chapter 1

Introduction

1.1 Motivation

Tornadic storms have been extensively studied using ground-based weather radar observations and satellite observations during the past four decades. A common goal of historical efforts has been enabling improvements in tornado prediction, which can save lives. Substantial efforts are almost always underway to improve tornado warnings, including ongoing projects like Warn-on-Forecast and PROB-SEVERE (Stensrud et al., 2009; Cintineo et al., 2014). Despite these efforts, the time from a warning being issued to a tornado occurring (commonly known as the warning lead time) has stayed the same from 1986-2011, averaging 18.5 minutes (Stensrud et al., 2013; Brooks and Correia, 2016).

There are different types of tornadic storms, but most varieties generally have a strong updraft (Bluestein, 2013). The storms that are the most likely to be able to produce tornadoes are supercells, which are categorized by a rotating updraft (Doswell and Burgess, 1993). These are able to produce tornadoes of all intensities. It is also possible to generate tornadoes without a rotating updraft. For example, one of the mechanisms for tornadogenesis in mesoscale convective systems (MCSs) allows tornadoes to be created due to preexisting vertical rotation in low-levels (Wakimoto and Wilson, 1989). These tornadoes are commonly weaker than those

produced by supercells, but have been known to still reach strengths of EF2 on the Enhanced Fujita Damage Scale, which ranges from 0 to 5. Tornadoes are not resolved by operational radars, but some of the characteristics of tornado-producing storms are routinely observed, such as hook echoes, bounded weak-echo regions (BWER), or debris signatures. More recently, tornadic storms have also been investigated by satellites, and signatures such as overshooting tops and cloud-top cooling rates are currently being associated with severe storms, but not tornadoes alone (e.g., Cintineo et al., 2013; Bedka et al., 2015).

Forecasting severe and tornadic storms hours to days in advance has largely been accomplished using predicted or measured properties of the near-storm environment (e.g., Parker, 2014). These include winds, temperature, moisture, and related variables such as convective available potential energy (CAPE) and vertical wind shear. While both individual environmental variables and unique combinations of different variables have proven to be useful predictors of tornadoes, it is difficult to utilize such data in the tornado-warning process given the limited number of observations available at scales necessary to resolve the near-storm variability (Parker, 2014; Thompson et al., 2003). In addition, the near-storm variability in environmental conditions (regardless of whether or not it is properly resolved) leads to considerable overlap in the parameter spaces occupied by tornadic and non-tornadic storms, which makes it challenging for a forecaster to determine which storms will and will not be tornadic within a given environment (Anderson-Frey et al., 2016).

Observing systems in the United States provide unparalleled measurements of storms at high spatial and temporal resolution and for long time periods. A network of ground-based weather radars known as the Next-Generation Weather Radar (NEXRAD) program provides three-dimensional observations of storms at approximately 5-minute increments (Crum and Alberty, 1993). Satellite imagery

from the Geostationary Operational Environmental Satellite (GOES) constellation provides cloud-top visible and infrared (IR) wavelength measurements of storms at frequencies of 15 minutes or less (Menzel and Purdom, 1994). As of December 2017, GOES-16 provides imagery with temporal resolutions of 30 seconds to 1 minute over 1000×1000 km regional domains, and every 5 minutes over much of North America (Schmit et al., 2005). Prior to GOES-16, GOES-14 was used in experimental mode to acquire 1-minute resolution data, with a focus on severe-storm analyses (Schmit et al., 2013). GOES-13 and -14 datasets are used in this study. GOES satellite observations are expected to increase in value with the upcoming addition of GOES-16 to operations, which has 4 times finer spatial resolution and as much as 2 times finer temporal resolution than the GOES-14 super rapid scan experiments used here.

This study is a part of a collaborative effort between National Aeronautics and Space Administration Langley Research Center (NASA LaRC), the University of Alabama, Huntsville, and the University of Oklahoma to keep improving current understanding of tornadic storms using high temporal remote sensing instruments. Nowcasting algorithms have become an important tool for forecasters when predicting severe weather, and this study aims to examine the usefulness of high-resolution radar and satellite observations near cloud top.

1.2 Evolution of Tornadic Storms and Tornadoes

It has long been known that tornadoes require a few specific ingredients to develop in supercells, but tornadoes seldom occur even when all of the necessary ingredients exist. In order for a tornadic supercell to form, the environment needs to be moist and unstable, air must be lifted to form storms, and there has to be strong vertical wind shear (Markowski and Richardson, 2009). These ingredients can result in deep, rotating updrafts that have been associated with tornadoes for decades (e.g.,

Lemon and Doswell III, 1979; Klemp, 1987; Doswell and Burgess, 1993). Although this is true and these conditions are required, they are not necessarily sufficient to produce tornadoes as storms can exist in these conditions without ever producing a tornado.

Current understanding of tornadogenesis in a supercellular storm starts by the updraft tilting horizontal vorticity (as a result of the wind shear) into the vertical, which creates a mid-level mesocyclone (Davies-Jones, 1984). The rear-flank downdraft (RFD) further tilts horizontal vorticity into the vertical in the low-levels. Strong convergence, and hence a strong updraft, is needed to increase this ground-level vorticity through stretching. Friction has also recently been found to be important in the generation of tornadoes, where it is needed for the rotating column to contract further when cyclostrophic balance is reached (Davies-Jones, 2015).

For non-supercells, the process of tornadogenesis may occur through other mechanisms or there could be a supercell embedded within if the storm is a mesoscale convective system. One mechanism that can explain tornadogenesis in storms with no mesocyclone is the stretching of preexisting vertical vorticity near the ground. This vertical vorticity can be generated by boundaries where there is existing shearing instability and is stretched by converging air near the ground as a result of a strong non-rotating updraft (Wakimoto and Wilson, 1989). Another mechanism that is thought to contribute to non-supercell tornadogenesis is a process happening along an outflow boundary with perpendicular environmental flow (Bluestein, 2013). Smaller vortices are created and pair up and merge into a stronger, bigger vortex. As in supercell tornadogenesis, friction is thought to be of importance for non-supercell tornadogenesis (Xu et al., 2015).

1.3 Radar and Satellite Observations of Tornadic Storms

To distinguish tornadic storms from non-tornadic storms, meteorologists have examined unique radar signatures that often precede tornadogenesis, such as hook echoes, weak echo regions, inflow notches, bowing line segments, and low-level rotation, which were key to early improvements in tornado warnings (Fujita, 1958; Browning and Donaldson, 1963; Lemon and Doswell III, 1979; Przybylinski, 1995). The first observation of a hook echo happened in April of 1953 (Stout and Huff, 1953), which was later analyzed by Fujita (1958) where he explored the hook echo in relation to the storm's rotation and linked it to tornadoes. Hook echoes usually appear in the lowest radar scans and are caused by the wrapping of hydrometeors into the rotating updraft near the RFD. Although hook echoes are commonly observed with tornadic supercells, it is possible to have a non-tornadic storm with a hook echo (e.g., Forbes, 1981) or for the hook echo to be non-existent prior to tornadogenesis (e.g., Garrett and Rockney, 1962).

Weak echo regions (bounded or unbounded) are also associated with supercells and often tornadoes. They are characterized by regions of low reflectivity surrounded or partly surrounded by high reflectivity. Weak echo regions are typically evident in the low-levels, while bounded weak echo regions are found in the mid-levels. The weak echo regions are caused by strong updrafts lofting particles of all sizes to higher altitudes, keeping them from falling to the surface within the updraft (Browning, 1965).

Bowing line segments are often severe and book-end vortices can be an indicator of a tornadic storm (Parker, 2014). These are caused by a rear-inflow jet pushing a line of storms ahead of a broader translating storm system. Inflow notches show up in radar imagery as notches of weak echo on the rear end of a bow echo, and

are a result of a strong rear-inflow jet. Inflow notches can also be an indicator of severe weather (Przybylinski, 1995).

Perhaps one of the most commonly identifiable radar signatures for tornadoes is the tornado vortex signature, which is evident as a radial velocity couplet (strong and adjacent outbound and inbound velocities) in the low-levels (Burgess et al., 1975). This is a sign of strong rotation, and while the WSR-88D radars cannot resolve the tornado itself, the low-level rotation is a good indicator of a tornado.

More recently, studies have examined polarimetric variables in tornadic storms, where areas of low differential reflectivity and correlation coefficient within the low-level vortex, which are indicators of non-meteorological scatterers, can signify debris signatures from tornadoes (e.g., Ryzhkov et al., 2005).

Tornado detection has largely focused on low-level observations from ground-based weather radars to date, as the low-levels are where tornadoes occur, but recent work has increasingly focused on satellite imagery of severe storms (e.g., Bedka et al., 2015; Gravelle et al., 2016). Satellite-observed cloud-top features associated with severe storms include the "Enhanced-V" signature, rapid cloud-top cooling, anomalous cloud-top flow characteristics (strong divergence and couplets of high positive and negative vorticity), overshooting storm tops (OTs), and above-anvil cirrus plumes (McCann, 1983; Cintineo et al., 2013; Bedka et al., 2015; Line et al., 2016; Apke et al., 2016; Homeyer et al., 2017). All of these features are in one way or another produced by strong upward motion within severe storms.

OTs have been studied in relation to severe weather using satellite since the late 1970s - early 1980s after the launch of the first GOES satellite (e.g., Reynolds, 1980; Heymsfield and Blackmer Jr, 1988). OTs are characterized by relatively low infrared brightness temperatures and "cauliflower-like" texture in visible imagery.

The Enhanced-V signature was first linked to severe weather by McCann (1983), and is identified by relatively cold IR brightness temperatures in the shape of a

"V" around a region of warmer temperatures. The mechanisms behind this signature have had several hypotheses that were recently investigated by Homeyer (2014), where it was found that the most likely explanation for the Enhanced-V signature is above-anvil cirrus clouds. Above-anvil cirrus have also been linked to severe storms without the accompanying Enhanced-V (Bedka et al., 2015), and have proved to be a robust predictor of hazardous weather. Homeyer et al. (2017) found that above-anvil cirrus are likely clouds that are injected into the lower stratosphere. These cloud features are often referred to as "plumes" given their chimney plume-like appearance in visible satellite imagery.

Winds have been calculated from tracking clouds in satellite imagery for decades (e.g., Hubert and Whitney, 1971), but have only recently been used to analyze severe weather. Analyses of severe storms have only been possible due to increased temporal resolution of satellite imagery, which makes it possible to resolve higher-density atmospheric motion vectors (at meso scales) for storm tops (Bedka and Mecikalski, 2005; Apke et al., 2016). Apke et al. (2016) found that signatures of strong cloud-top divergence and vorticity couplets are indicators of severe storms.

Increased resolution and the development of objective identification and tracking of some of these signatures have provided valuable information in the now-casting of severe storms. For example, Mecikalski et al. (2008) evaluated fields of developing cumulus from satellite in order to predict convective initiation, while Cintineo et al. (2013) investigated several metrics to identify severe storms using satellite.

This study combines the radar and satellite datasets, as has been done previously by e.g., Wexler and Blackmer Jr (1982); Dworak et al. (2012); Cintineo et al. (2013); Bedka et al. (2015). However, the examination of a large sample of storms, the inclusion of upper-level radar metrics, and the focus of this work on distinguishing between tornadic and non-tornadic storms makes this study novel.

Chapter 2

Data and Methods

2.1 Cases

This study examined 29 severe weather days in the United States during 2011-2016 that comprised more than 8000 storms, of which 335 produced tornadoes (Table 2.1). Severe weather days were chosen to represent a wide range of environmental conditions, tornado frequencies, and tornado strengths. Nine of the 29 days were chosen due to the availability of GOES-14 super rapid scan data (1-minute frequency), which is necessary to calculate satellite-based cloud-top divergence (Apke et al., 2016). The days where GOES-14 data was available are bolded in Table 2.1.

The domain of the combined cases is shown in Figure 2.1. The cases are clustered mainly in the central U.S., but extend through most of the eastern United States and the Mississippi Valley.

The southeast United States "Super Outbreak" of April 2011 was included in this study, but has been excluded from the overall analyses because an event of this magnitude is extremely rare and included over 1000 storms (>10% of the entire 29-day dataset), which (if included) could skew the results of the analysis. However, it was analyzed separately to confirm the general results of this study.

Table 2.1: Overview of cases.

Date	No. Storms (No. Tornadic)	No. Supercells (No. Tornadic)	No. Tornadoes	Max Day-1 SPC Tornado Risk (%)	Analysis Domain Coordinates [lon0, lat0, lon1, lat1] (°W and °N)
*26-27 April 2011	1098 (62)	49 (34)	267	30/45	[97.0, 30.0, 81.0, 37.0]
22 May 2011	469 (21)	28 (13)	59	15	[95.5, 35.5, 87.0, 46.5]
24 May 2011	450 (24)	29 (18)	64	45	[101.5, 32.0, 92.5, 39.0]
9 April 2012	30 (1)	5 (1)	6	5	[101.0, 33.5, 95.0, 37.5]
13 April 2012	97 (3)	12 (3)	14	10	[100.5, 34.5, 95.0, 37.0]
14 April 2012	313 (23)	17 (14)	96	45	[101.0, 36.0, 95.5, 41.5]
20 May 2013	246 (16)	23 (13)	35	10	[99.0, 31.5, 93.0, 40.0]
31 May 2013	391 (14)	27 (8)	36	15	[99.0, 34.5, 87.0, 40.5]
12 June 2013	555 (10)	0 (0)	21	15	[96.0, 38.0, 80.0, 45.0]
27 April 2014	223 (8)	10 (7)	21	30	[99.0, 34.0, 91.5, 42.0]
10 May 2014	112 (2)	18 (2)	5	5	[99.0, 36.0, 90.0, 43.0]
11 May 2014	330 (10)	15 (6)	41	15	[102.0, 36.0, 92.0, 44.5]
21 May 2014	54 (2)	1 (1)	5	10	[106.0, 37.5, 101.0, 41.0]
16 June 2014	406 (10)	10 (4)	40	15	[100.0, 41.0, 89.0, 44.0]
17 June 2014	155 (7)	14 (7)	16	10	[106.0, 41.5, 94.5, 48.0]
18 June 2014	79 (5)	7 (5)	13	10	[100.0, 43.5, 98.0, 46.5]
13 October 2014	707 (17)	0 (0)	24	15	[95.5, 29.5, 84.5, 40.5]
6 May 2015	202 (23)	30 (18)	52	10	[100.0, 32.5, 95.5, 41.5]
19 May 2015	329 (13)	35 (12)	36	5	[103.0, 29.0, 94.0, 37.0]
24 May 2015	123 (1)	2 (1)	10	5	[105.0, 36.0, 97.0, 41.0]
25 May 2015	669 (18)	0 (0)	28	10	[105.0, 25.0, 89.0, 41.0]
27 May 2015	387 (8)	25 (8)	18	5	[104.0, 29.5, 96.0, 41.5]
4 June 2015	290 (3)	12 (3)	23	5	[108.0, 34.0, 93.0, 43.0]
23 December 2015	137 (7)	4 (3)	26	15	[92.5, 33.5, 84.0, 42.0]
15 April 2016	160 (4)	4 (3)	12	5	[104.0, 34.5, 99.0, 40.5]
9 May 2016	199 (10)	13 (10)	26	10	[100.0, 33.0, 94.0, 41.5]
24 May 2016	150 (11)	18 (10)	44	10	[104.0, 35.5, 97.0, 41.0]
25 May 2016	17 (2)	4 (2)	6	5	[99.5, 35.5, 95.0, 40.0]
Total	**8378 (335)**	**412 (206)**	**1044**	–	–

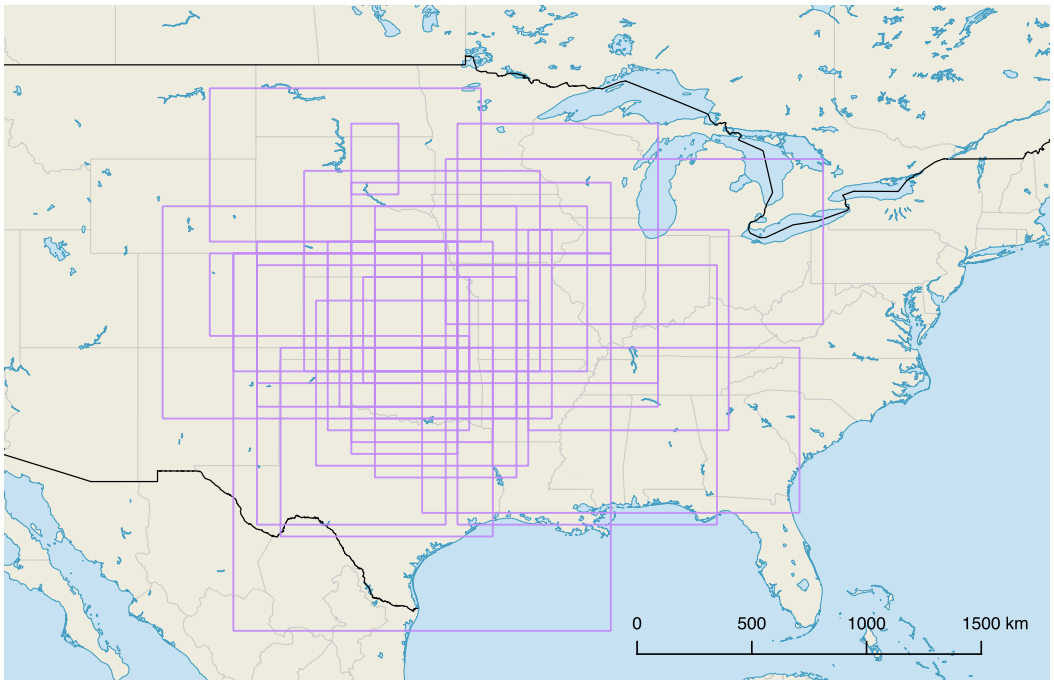

Figure 2.1: Domains for all cases.

Four of the 29 cases contained storms that produced EF5 tornadoes. The leading motivation for picking these cases was due to the rarity of the strongest tornadoes. Though stronger tornadoes usually last longer than the weaker ones, the number of data points per tornado strength category in this study is smaller for EF5 tornadoes, while data counts for the remaining categories (EF0 to EF4) are comparable.

Mesoscale convective systems (MCSs) were the dominant storm mode for six of the 29 severe weather days; the rest were dominated by discrete convection. MSCs are associated with weaker tornadoes and MCS tornadogenesis has a different evolution than that for supercells (Markowski and Richardson, 2009). Tornadoes are sometimes hard to forecast for MSCs, but it is demonstrated that the methods of this study can distinguish between tornadic and non-tornadic storms regardless of storm mode.

In addition to selection based on GOES-14 data availability and tornado strength, some events were chosen because they were high-profile cases, some due to visual

confirmation of tornadoes by a team member, and others because there were specific storms that were not warned prior to producing a tornado.

58-104 different variables were calculated for or linked to the storms for each case depending on what data was available. Some were calculated for quality control (e.g., location of divergence signatures from satellite) or as potential variables for studies of a different focus (e.g., wind or hail reports), while others are being omitted from discussion due to little-to-no difference between tornadic and non-tornadic populations.

2.2 Radar

Next-Generation Weather Radar (NEXRAD) Level II (i.e., volume) data was retrieved from the National Centers for Environmental Information (NCEI). The NEXRAD network consists of more than 100 WSR-88D S-band (10-11 cm wavelength) radars that observe clouds and precipitation on a polar grid in range, azimuth, and elevation relative to the location of the radar. All NEXRAD observations used in this study were obtained at a range resolution of 250 m, an azimuthal resolution of 0.5 degrees for the lowest 3-4 elevations and 1.0 degree otherwise, and typically at 14 elevations per volume. Each Level II volume includes (at a minimum) the radar reflectivity at horizontal polarization Z_H that is proportional to the size and/or density of cloud- and precipitation-sized particles in a radar volume and is in units of dBZ, and the radial velocity (V_R), a measure of the motion of cloud- and precipitation-sized particles toward and away from the radar location, in units of m s^{-1}.

The radar data was processed using the four-dimensional space-time merging methods described in Homeyer et al. (2017) and references therein, which resulted in volumes of the radar variables at 2-km horizontal resolution, 1-km vertical resolution, and 5-minute temporal resolution over the entire extent of each analysis

domain (see also information available at `http://gridrad.org`). Merging of V_R from multiple radar volumes onto a common grid is challenging, largely due to the fact that V_R is a measure of the motion of scatterers toward and away from the radar, such that any given measurement has a unique geometry and thus is incomparable to a measurement made at the same location from a different radar. In order to overcome this challenge, derivatives of V_R must be merged instead. For this study, the radial derivative (in spherical coordinates) of V_R (radial divergence) and the azimuthal derivative (azimuthal shear or rotation) are merged, both of which are computed using centered differencing.

Merging of the V_R derivatives requires multiple quality-control steps. First, since V_R is prone to large errors in magnitude and sign due to aliasing (i.e., winds that exceed the maximum detectable V_R at a given operating frequency – the Nyquist velocity – and become "folded"), the winds must be de-aliased prior to computing the derivatives. De-aliasing is performed using the Python ARM Radar Toolkit (Py-ART; Helmus and Collis, 2016). For use in this merging procedure, a Py-ART routine was invoked that does not require a reference atmospheric wind profile and is more computationally efficient than alternative approaches – dealias_region_based, which accomplishes de-aliasing by modeling the problem as a dynamic network reduction (see `http://arm-doe.github.io/` for additional detail).

Following de-aliasing, random fluctuations of V_R in each azimuthal sweep (a 360-degree scan made at a single elevation) are further suppressed first by using a 3×3 median filter and second by using a 5-gate running-mean range filter prior to computing the radial and azimuthal derivatives (divergence and rotation). The derivatives are then calculated using the quality controlled V_R and merged into the large-area, multi-radar dataset following the procedure in Homeyer et al. (2017). In order to avoid potential artifacts within weak radar echo, V_R derivatives are

only analyzed within $Z_H \geq 30$ dBZ in this study. The divergence maximum above an altitude of 8 km (upper-level) and the convergence maximum – or divergence minimum – below 3 km (lower-level) were calculated for each storm at each time step. Maximum cyclonic rotation was also calculated for the lower- and upper-level altitudes, as well as for the mid-levels (4-7 km).

Relationships between the horizontal divergence and vertical velocity are made for the atmosphere using the mass continuity assumption. For an incompressible atmosphere (one with negligible changes in density with altitude), the equation for mass continuity is as follows:

$$\frac{\partial u}{\partial x} + \frac{\partial v}{\partial y} + \frac{\partial w}{\partial z} = 0 \tag{2.1}$$

where u, v, and w are the x, y, and z components of the three-dimensional wind. The first two terms in Equation 2.1 comprise the horizontal divergence. Rearranging Equation 2.1 and integrating in altitude provides the vertical velocity w. Mass continuity for an incompressible atmosphere is a good approximation for shallow motions on Earth, so it is not a good quantitative measure when considering deep convection since the density decreases approximately logarithmically in Earth's atmosphere with increasing altitude. It can still give a satisfactory picture of the qualitative vertical motion, but a more accurate approach for deep convection is to use the anelastic approximation for mass continuity:

$$\rho\frac{\partial u}{\partial x} + \rho\frac{\partial v}{\partial y} + \rho\frac{\partial w}{\partial z} + w\frac{\partial \rho}{\partial z} = 0 \tag{2.2}$$

where the atmospheric density ρ is a function of altitude, and the product of ρ and the horizontal divergence is known as the "mass flux divergence", typically expressed in units of kg m^{-3} s^{-1} rather than s^{-1}. Both the flow divergence (the terms from Equation 2.2) and the mass flux divergence (the product of flow divergence and observed atmospheric density) are shown in this study. Mass flux divergence

is computed for radar data using the atmospheric density at the altitude of the radar measurement.

Implied ascent was calculated using the incompressible version of the continuity equation (Equation 2.1) by integration in altitude between low-level convergence and upper-level divergence maxima in each grid column, which introduces several potential errors, but is still shown here to be interpreted qualitatively. The median and maximum implied ascent values for each storm were calculated within 10 km of the storm location, as well as the area of ascent exceeding 10 m s^{-1}. The area of strong implied ascent is synonymous to updraft width.

Spectrum width, or the standard deviation of velocity estimates within a radar volume, is extracted from the radar data where the radar reflectivity is greater than 30 dBZ. Spectrum width is influenced by different factors including shear from the radial velocity and turbulence (Doviak and Zrnić, 1993). The turbulence component has been linked to updraft strength (Feist et al., 2017). The column maximum spectrum width and its maximum value below 3 km are calculated for analysis of each storm.

Echo-top altitudes are computed for this study using multiple Z_H thresholds, though the 40-dBZ echo-top altitudes are used for analysis. The echo-top altitudes are computed at every horizontal grid point by finding the highest altitude where Z_H exceeds the specified threshold, provided that Z_H was also greater than the threshold in the next two lowest altitude layers.

The dual-polarization variables considered in this analysis are correlation coefficient and differential reflectivity. The column minimum for each variable was calculated for each storm where the reflectivity is at or above 45 dBZ in order to reduce influence by non-meteorological targets and identify possible large hail signatures. Correlation coefficient (or ρ_{HV}) is a measure of the variety of the hydrometeor shape, orientation, or phase within the sample volume, where lower

values signify a larger variation. Reductions in ρ_{HV} below a value of about 0.97 are indicative of mixed-phase regions (e.g., melting layers) or non-meteorological echoes. The differential reflectivity (or Z_{DR}) is the difference between the horizontal and vertical reflectivity factors, where values near zero signify spherical shape of hydrometeors within the radar sample volume. Z_{DR} values near zero are therefore often a good indicator of large hail and negative Z_{DR} values are often indicative of large wet hail (Balakrishnan and Zrnić, 1990). Columns of high Z_{DR} values can be created by lofting of supercooled liquid above the freezing level and are indicative of a strong updraft (Kumjian et al., 2014).

Analyses of all datasets on an individual storm basis in this study was facilitated through objective radar-based storm tracking. In particular, individual storm tracks were computed for each severe weather day using an echo-top algorithm described in Homeyer et al. (2017). Local maxima in echo-top altitudes are identified in each 5-minute radar volume and linked together in time if they lie within close proximity to each other. For this study, tracking is accomplished through time linking of $Z_H = 40$ dBZ echo-top maxima, filtered by the convective echo classification output by the Storm Labeling in 3 Dimensions (SL3D) algorithm (Starzec et al., 2017). The objectively tracked storms were reviewed to manually identify and merge discontinuous tracks that correspond to the same storm. The quality-controlled storm tracks were then used to extract maximum values from each dataset within a 10-km radius of the storm location at 1-minute intervals, with observations made at coarser resolution than 1-minute interpolated linearly in space and time to the storm track location. Such interpolation was only performed for data with time coverage gaps less than or equal to 5 minutes. Figure 2.2 shows the resulting tracks from all storms exceeding 30 minutes in length analyzed in this study.

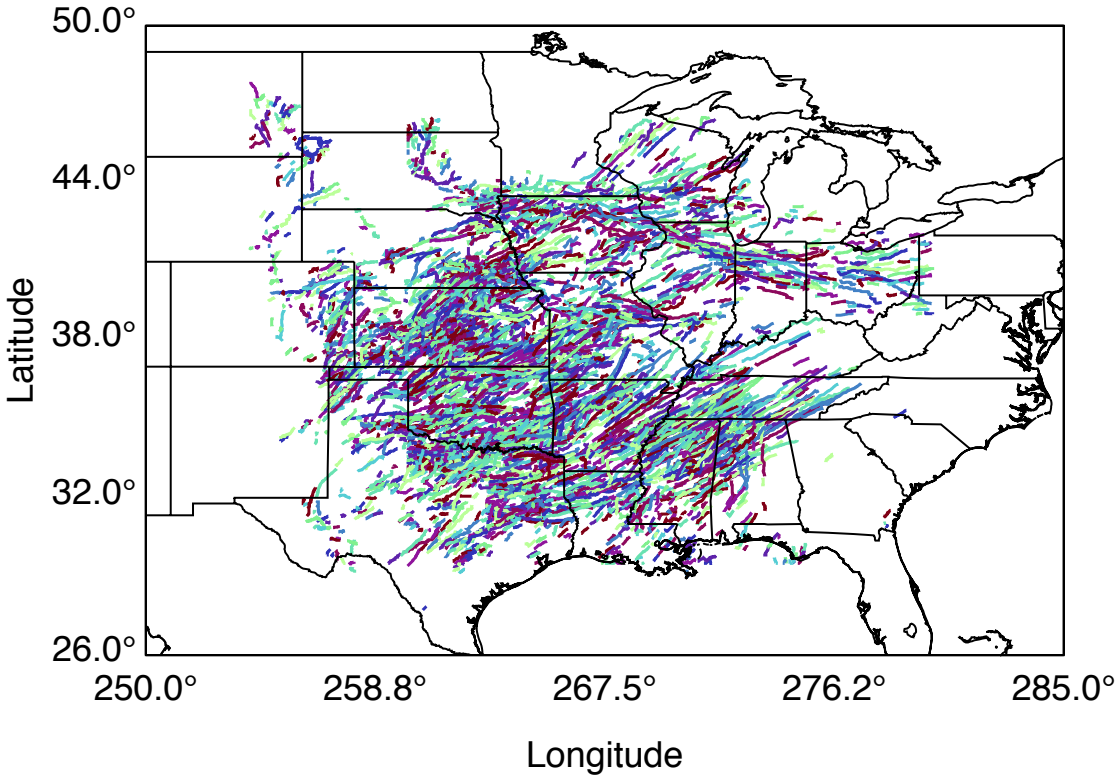

Figure 2.2: Storm tracks of at least 30 minutes in length from all 28 cases. Variation in color is arbitrary and meant to improve interpretation of overlapping storms.

2.3 Satellite

Geostationary Operational Environmental Satellite (GOES) imagery was also retrieved from NCEI. GOES is primarily a constellation of two operational satellites that continuously monitor the weather over the United States: GOES-West stationed at 135°W and GOES-East at 75°W nadir longitudes. For the time period analyzed in this study, GOES-15 was operational in the West position and GOES-13 was operational in the East position. GOES-13 and -15 provide visible and infrared (IR) imagery at 5- to 15-minute intervals. A spare GOES satellite (GOES-14), positioned at 105°W, has been used for experimental super rapid scan

observations in preparation for GOES-R (1-minute frequency; SRSOR) during various periods since late summer 2012 (Schmit et al., 2013). For nine severe weather days (bolded in Table 2.1), 1-minute imagery from GOES-14 was used for analysis. For the remaining severe weather days, imagery from GOES-13 was used. The visible imager aboard the GOES-13 and -14 satellites has a horizontal resolution of 1 km at nadir, while the IR imager has a horizontal resolution of 4 km at nadir and an absolute accuracy of $\leq$1 K (Menzel and Purdom, 1994).

Convective updrafts of sufficient strength to penetrate through a thunderstorm anvil, known as overshooting tops, produce texture in GOES visible-channel imagery due to turbulent flow and shadowing induced by the updraft penetration. An algorithm to detect and quantify this texture has recently been developed that produces a "visible texture rating" product (Bedka and Khlopenkov, 2016). Anvil clouds are identified using a two-step process and then a search is performed within the anvils to identify texture associated with penetrative updrafts. The first step in anvil detection is based on thresholding of GOES visible reflectance based upon an empirical model used to define how bright an anvil should be at given time of day and day of year. Spatial and statistical analysis of the pixels that meet the day/time-dependent threshold is performed to eliminate singular pixels and preserve those within a broad area (greater than or equal to approximately 10 km^2) of near-uniform reflectance characteristic of anvil clouds. Fourier-transform analysis of visible reflectance within small (32 pixel) windows is then performed, yielding a power spectrum for varying wavelengths in a 32$\times$32-pixel domain. Typical OT signatures and concentric gravity waves that often surround OTs produce the strongest signal in a ring-like pattern with a wavelength of $\sim$4-8 km. Pattern recognition is applied to the power spectrum to identify ring patterns within this wavelength range. The results of the pattern recognition analysis define the

unitless visible texture rating; the most coherent ring patterns are assigned a high rating.

Infrared brightness temperature from satellite is also examined. The minimum within a storm is calculated and compared with the temperature at the tropopause from NARR in order to investigate the minimum tropopause-relative temperature of the cloud tops, which can be indicative of the vertical extent of a storm into the stratosphere.

The derivation of mesoscale atmospheric motion vector (mAMV) flow grids begins by identifying targets such as maxima, minima and gradients in GOES visible, IR and water vapor imagery (Bedka and Mecikalski, 2005). Point-source motion is quantified by tracking targets through a series of three satellite images spaced 1 minute apart in SRSOR imagery. Tracking is achieved by identifying the minimum sum-of-square error values for targets in permissible search regions within the images. The tracked motions are height assigned using IR and water vapor imagery comparisons to Global Forecasting System (GFS) numerical model output. All point-source winds assigned to altitudes above 500 hPa are assumed to be on a two-dimensional flat plane, to which an objective analysis is used to retrieve $0.02^\circ \times 0.02^\circ$ longitude-latitude grids of horizontal flow at the cloud top. The final retrieved product is termed the Super Rapid Scan Anvil Level flow system (SRSAL; see Apke et al. (2016) and references therein). This study employs version 2.2 of SRSAL, which is an updated version from Apke et al. (2016) that uses targets 5×5 pixels in size and a low permissible gradient threshold of 4 for mAMV target gradient identification. SRSAL v2.2 utilizes a recursive filter (RF; Hayden and Purser, 1995) instead of a Barnes (Barnes, 1973) analysis to perform the objective analysis of derived flow. The specific default settings for the RF are detailed in Table C1 in Hayden and Purser (1995), though SRSAL v2.2 uses modified settings for mAMV

analysis. The two background RF analyses are performed on GFS tropopause-level flow with the default settings from Hayden and Purser (1995). The second background analysis and observation analysis use a wind error tolerance of 25 m s^{-1}. For the RF observation analysis, the RF is applied on the grid five times, with three smoothing iterations per pass. Initial and final characteristic spatial scales are set to 16 km and 10 km respectively. The RF background wind weight in the observation analysis is set to 0.01 and the observation weight is set to 1. The smoothness degree (parameter f in 34) is set to 1 for the initial four observation passes and 0.5 for the final observation pass. When wind observations are not available for flow derivation, the RF analysis interpolates to GFS tropopause-level flow.

Centered finite differencing of the mAMVs from satellite is used to retrieve cloud-top vertical vorticity (CTV) and cloud-top horizontal divergence (CTD). When associating GOES CTD with individual storms, only data points with final smoothing parameter (α) values less than 0.5 were considered for analysis, as points with higher values were not densely sampled by mAMVs. In order to mitigate cirrus contamination (the masking of cloud-top flow in a desired storm by thin cirrus lying above), the data points for CTD, as well as visible texture rating, were filtered by using only those points with a maximum visible texture rating greater than 7, which is indicative of an overshooting convective top (Bedka and Khlopenkov, 2016). CTV in the immediate vicinity of a large sample of deep convection is frequently largest at or near cloud-edges with the SRSAL flat plane assumption, and thus will require more filtering and perhaps a separate three dimensional analysis prior to implementation on a statistical basis, which is currently beyond the scope of this project. Once completed, analysis of storm-related CTV can be compared to the findings here of the radar-based upper level vorticity prior

to the formation of tornadoes in severe thunderstorms. The maximum CTD is calculated for each storm.

Mass flux divergence is computed for the satellite data using the atmospheric density at the cloud-top altitude (approximated using the tropopause altitude from NARR). The maximum cloud-top mass flux divergence for each storm is also extracted for analysis.

In order to extract satellite data along the path of the radar-based storm tracks, corrections for parallax error (that owing to the viewing geometry of the satellite) are required. Parallax error increases as the cloud top altitude increases. Methods typically used to correct for parallax involve converting IR cloud-top temperature to cloud-top altitude using a reference tropospheric temperature profile. However, these methods are prone to large errors for deep convective anvils because high-altitude clouds may either be: i) thermally adjusted to stratospheric temperatures that are warmer than the upper troposphere, or ii) be optically thin and thus mostly transparent in IR. In this study, the merged radar observations are used to correct for parallax error. In particular, the $Z_H = 5$ dBZ echo top is used as a proxy for cloud-top height to estimate parallax. These estimates were used to correct the coordinates of the satellite imagery in order to extract values coincident with the storm tracks.

Only the position of the satellite, the cloud-top height, and the coordinates of the correct position of a particular data point are needed to calculate the radar-based parallax. The traditional satellite-based parallax is similarly calculated using the position of the points to be corrected. Some studies that compare satellite and radar data have used a radar-based parallax correction to align radar data with the satellite data (Radová and Seidl, 2008), but due to the additional and varied datasets used in this study, parallax corrections for only the satellite data were necessary. Linking the satellite data points to the correct location was done by

using basic trigonometric equations. Once the parallax estimate of a cloud field was found, it was interpolated from the radar grid to the given satellite grid, which was different for the SRSAL and OT datasets.

The first step in calculating the radar-based parallax is to find the central angle between the satellite and the correct point from radar (α_{cc}) by using Equation 2.3 (for illustration, see Figure 2.3).

$$\alpha_{cc} = 2 \cdot \arcsin \sqrt{\left(\sin \frac{y_s - y_c}{2} \right)^2 + \cos y_s \cdot \cos y_c \cdot \left(\sin \frac{x_s - x_c}{2} \right)^2} \tag{2.3}$$

where y_s is the latitude of the satellite, y_c is the latitude of the correct point from radar, x_s is the longitude of the satellite, and x_c is the longitude of the correct point from radar. The central angle is then used to calculate the satellite viewing distance between the satellite and the cloud top (d) using the Law of Cosines, which in turn is used to find the satellite viewing angle (α_{sv}) using Equations 2.4 and 2.5.

$$d = \sqrt{h_s^2 + h_{ct}^2 - 2 \cdot h_s \cdot h_{ct} \cdot \cos \alpha_{cc}} \tag{2.4}$$

$$\alpha_{sv} = \arccos \frac{h_s^2 + d^2 - h_{ct}^2}{2 \cdot h_s \cdot d} \tag{2.5}$$

The satellite viewing angle is used to deduce the central angle for the satellite in reference to the point that needs parallax correction (α_c) by Law of Sines using Equations 2.6 and 2.7.

$$\alpha_p = \arcsin \frac{h_s \cdot \sin \alpha_{sv}}{r_E} \tag{2.6}$$

$$\alpha_c = \pi - \alpha_p - \alpha_{sv} \tag{2.7}$$

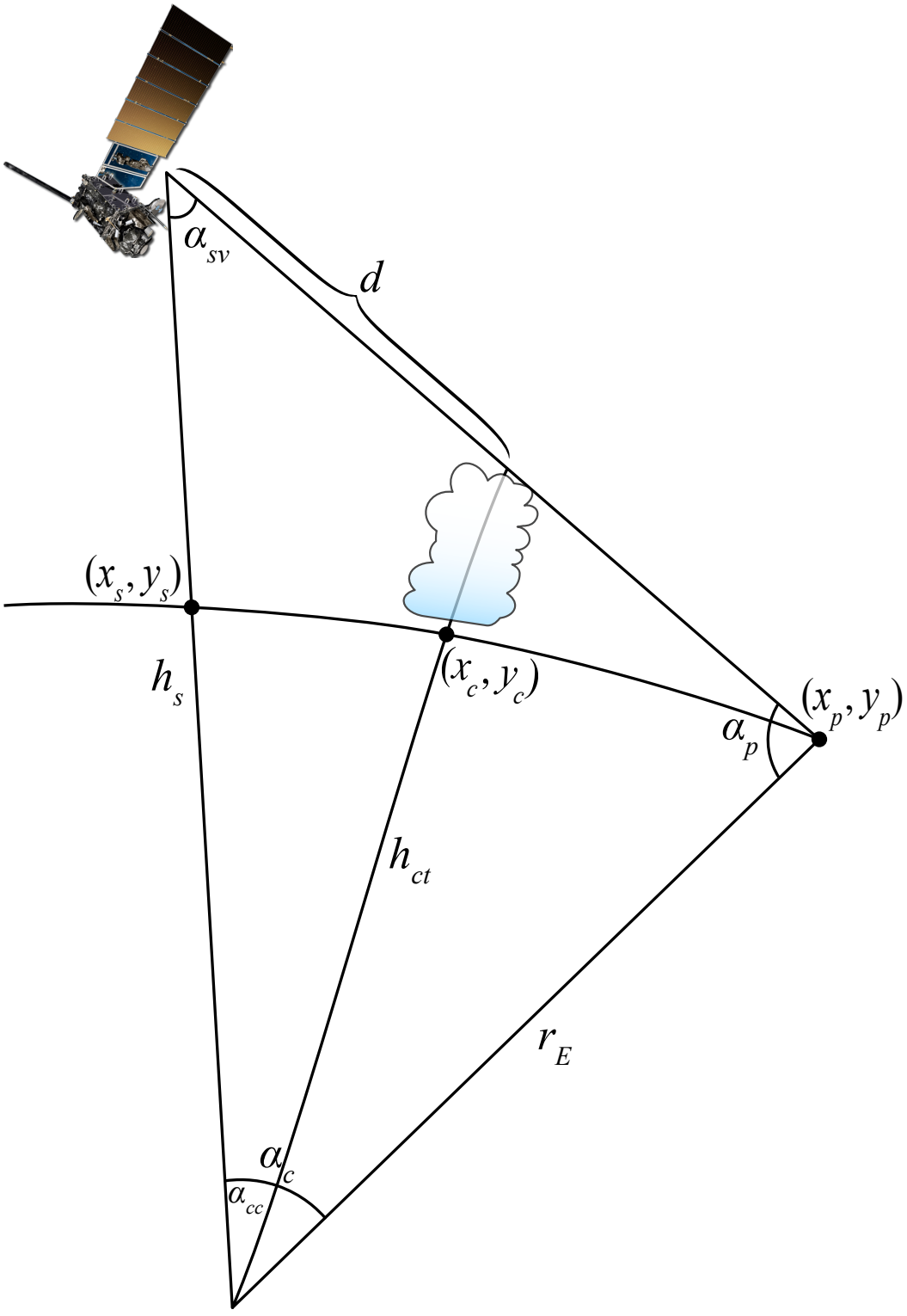

Figure 2.3: Parallax correction illustration.

where α_p is the angle between the radius of the Earth and the full satellite viewing distance, and r_E is the radius of the Earth. The same process from Equations 2.5, 2.6, and 2.7 is repeated for latitude instead of angles in order to find the latitude of the point that should be linked to the given correct point (y_p). The final step is to compute the longitude of the point that needs to be parallax corrected (x_p), which is done using Equation 2.8. The sign of the second term of the equation depends on whether the storm is to the east or the west of the satellite.

$$x_p = x_s \pm 2 \cdot \arcsin \sqrt{\frac{\left(\sin \frac{\alpha_c}{2}\right)^2 - \left(\sin \frac{y_s - y_p}{2}\right)^2}{\cos y_s \cdot \cos y_p}} \tag{2.8}$$

Examples of the resulting parallax correction are shown in Figures 2.4 and 2.5. Colder temperatures generally indicate higher cloud tops. Echo-top altitudes are used as a proxy for cloud-top height, so the coldest IR brightness temperatures should line up with the tallest echo-top heights.

Figure 2.4 shows an example of a storm from 11 May 2014 at 2300 UTC. At this time, no parallax correction was available from the satellite dataset, which further demonstrates the need for a radar-based parallax correction (i.e., often poor data availability for satellite-based parallax corrections). The left panel depicts the raw data from radar and satellite, and focusing on the white areas of IR brightness temperature and the edges of the storm it is evident that the datasets are differing in the actual location of the storm. In the panel on the right, the radar-based parallax correction has been applied, and the areas of colder temperatures now fall mostly within the 15-km echo-top altitude contours and all the echo tops are contained within the satellite-observed cloud shield.

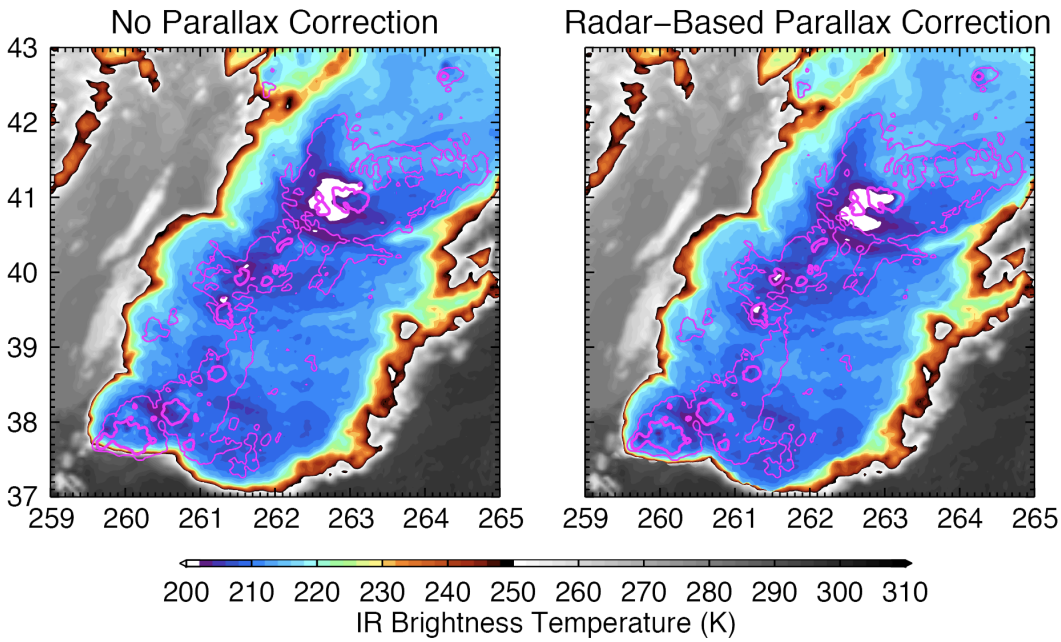

Figure 2.4: Parallax correction example for 11 May 2014 at 2300 UTC. The infrared brightness temperature is shaded by the scale below the plots. The magenta contours represent 5-dBZ echo-top altitudes greater than 13 km (thin lines) and 15 km (thick lines).

Another example is presented in Figure 2.5 from 12 June 2013 at 1940 UTC where satellite-based parallax correction was available for a few hours of the case. The satellite-based parallax-corrected data in the middle panel shows similarities to the radar-based correction in the center of the largest cloud feature (an MCS), but it provides no correction for the smaller cloud features in the southeastern portion of the domain.

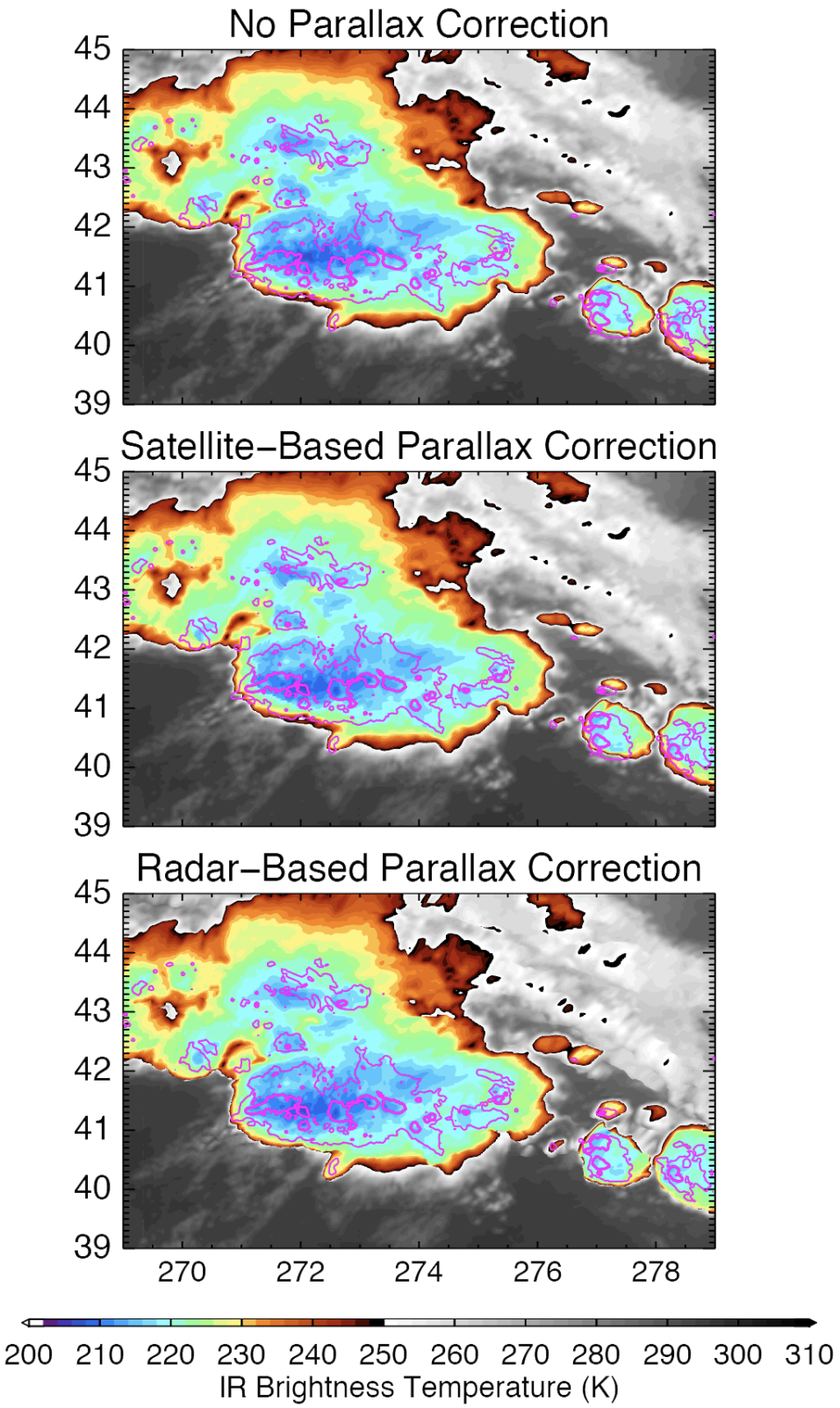

Figure 2.5: As in Figure 2.4, but for 12 June 2013 at 1940 UTC.

2.4 Lightning

The Earth Networks Total Lightning Network (ENTLN) detects lightning using pulses in vertical electric field measurements from parts of the 1 Hz to 12 MHz frequency range from over 700 sites across the contiguous United States (Liu and Heckman, 2011). Individual pulses are located in space and time by statistically solving over-determined electrical signal time-of-arrival equations using measurements from at least 5 stations. Sources close together in space and time are grouped into flashes, which are binned into $0.08^\circ \times 0.08^\circ$ longitude-latitude ($\sim$64 km^2) flash density grids for analysis.

Lightning flash density data was extracted from the ENTLN dataset. The maximum of the total lightning flash density, which consists of both cloud-to-ground and intracloud flash density, within a storm is calculated.

2.5 NARR

Characteristics of the atmospheric environment (tropopause altitude and temperature, CAPE, and effective bulk wind shear) were extracted from North American Regional Reanalysis (NARR) output. NARR aims to provide best estimates of the atmospheric state over the United States at a horizontal resolution of 32 km, 29 vertical levels, and a time increment of 3 hours. NARR output for this study was retrieved from NCEI and the National Center for Atmospheric Research (NCAR) Research Data Archive (RDA). Environmental variables from NARR were linearly interpolated to the radar-based storm tracks in space and time for analysis.

Several variables were extracted, including tropopause height and temperature, most-unstable CAPE, the u- and v-components of the wind, and cloud-base and

cloud-top altitudes. Bulk effective shear is calculated using the winds at the cloud-base and cloud-top. Upward motion (w) is estimated from most-unstable CAPE using Equation 2.9.

$$w = \sqrt{2 \cdot \text{CAPE}} \tag{2.9}$$

2.6 Warnings

Tornado warnings from the National Weather Service (NWS) are used for performance comparisons and were obtained from the online archive maintained by Iowa State University (`https://mesonet.agron.iastate.edu/request/gis/watchwarn.phtml`). The warnings are provided as shapefiles, with each warning consisting of a start (issuance) and end (expiration) time and coordinates of a polygon outlining the warned area. Warnings were linked with individual storms using the coordinates of the radar-based storm tracks. If a storm track passed through a warning polygon during the time the warning was valid, the warning was documented at all valid times along the track.

2.7 Tornado Reports

Severe Weather Data Inventory (SWDI) tornado reports from NCEI were also added to the dataset and linked to the nearest storm within 3 km of the tornado path. Weak tornadoes have been known to be under-reported in the past, and there has been a clear population bias in reporting tornadoes (Doswell III et al., 1999). More recently, there has been a decline in the population bias in the Central Plains, where more tornadoes outside of the bigger cities in the Plains have been reported (Elsner et al., 2013). Elsner et al. (2013) hypothesize that the increasing number of and technology available to storm chasers have positively influenced this bias.

Although this may be true, there are still many tornadoes that go unreported in rural areas (e.g., Anderson et al., 2007), introducing possible bias. However, since the reports used in this study are only from the 21st century and mostly from the Plains, it was deemed sufficient to make no efforts towards minimizing population bias. Therefore, some tornadic storms may have been incorrectly placed in the non-tornadic storm population, which could cause less separation between tornadic and non-tornadic storms in this study.

2.8 Supercell Classification

Supercell storms were identified using radar observations for all 29 severe weather days via a combination of objective and subjective methods. First, 15 storms were subjectively identified as supercells out of a sample size of 330 storms. The lowest values of maximum and mean upper-level divergence, maximum mid- and upper-level rotation, $Z_H = 40$ dBZ echo-top altitudes, and lifetimes for these 15 supercells were used as objective thresholds for identifying candidate supercell storms in the remaining cases in order to limit the number of storms to be subjectively analyzed. The threshold values used for objective identification are 5.5 and 3.5 $\cdot 10^{-3}$ s^{-1}, 4.5 and 4 $\cdot 10^{-3}$ s^{-1}, 12 km, and 60 min, respectively. Following the objective identification, entire lifetimes of the candidate storms were subjectively analyzed to confirm or deny supercellular characteristics. In particular, several conditions were examined to aid the classification of a supercell: If a storm was discrete, characterized by deviant motion relative to neighboring storms, contained a hook echo, or contained a bounded weak echo region (Doswell and Burgess, 1993; Fujita, 1958; Browning and Donaldson, 1963; Lemon and Doswell III, 1979). If most of these conditions were met, the storm was categorized as a supercell. This classification method resulted in 412 confirmed supercells, half of which produced tornadoes (Table 2.1). The fraction of supercells that produced tornadoes might

have been biased by the classification criteria, where weak supercells, as well as supercells embedded within an MCS, are possibly missed. The tornadic storms were subjectively examined for supercellular characteristics regardless of whether they were identified by this classification algorithm. This bias could lead to more overlap in certain variables between tornadic and non-tornadic storm populations, since potentially weak, tornadic supercells were identified, but some weak non-tornadic supercells might have been missed.

Chapter 3

Results and Discussion

Although time series analyses of individual storms were performed, no conclusive trends in time variation of different variables were seen in association with tornadoes. This may be due to the storms that were examined, or that the tracking algorithm does not identify storms until a storm is sufficiently strong in order to be able to produce a 40-dBZ echo top. Instead, statistical analyses comparing tornadic and non-tornadic storms were executed in order to evaluate the potential differences between the two populations. The notched box-and-whiskers throughout the analyses presented in this chapter show the 5th, 25th, 50th, 75th, and 95th percentiles of each metric and for all severe weather days for which data is available. Notches in the boxes emanating from the median values represent the 95% confidence interval for the median values. When the notches of different boxes within the same subplot do not overlap, the medians are significantly different (Krzywinski and Altman, 2014).

The leftmost box in each subplot shows distributions based on the entire lifetimes of non-tornadic storms. The five remaining boxes in Sections 3.1-3.3 show distributions for tornadic storms at 30 and 15 minutes prior to the first tornado of each storm, during the lifecycle of all tornadoes, and 15 and 30 minutes after the last tornado of each storm, from left to right. The tornadic storms are analyzed

Table 3.1: Number of data points per box for box plots in Sections 3.1-3.3.

Figure	Non-tornadic	30 min before first tornado	15 min before first tornado	During tornado	15 min after last tornado	30 min after last tornado
3.1	268089	184	228	6130	201	155
3.2	33873	22	27	541	19	10
3.3	208793	159	193	5244	166	131
3.4	266758	184	225	6133	200	156
3.5	33873	22	27	541	19	10
3.6	207039	159	191	5192	166	133
3.7	276127	185	228	6210	204	160
3.9	45168	38	43	977	32	22
3.10	90702	52	65	1419	49	42
3.11	209988	170	211	5834	179	138
3.12	234541	169	207	5690	188	146
3.13	209304	160	193	5279	166	133
3.14	80934	37	41	844	39	25
3.15	276127	185	228	6210	203	160
3.16	264725	180	223	6006	201	158
3.17	264725	180	223	6006	201	158
3.18	192091	167	205	5692	167	132
3.19	222511	139	171	4045	152	121
3.20	222511	139	171	4045	152	121
3.21A	27560	142	163	5042	146	127
3.21B	240529	42	65	1088	55	28
3.22A	23111	126	141	4389	120	106
3.22B	185982	33	52	855	46	25
3.23A	27624	142	163	5059	146	127
3.23B	248503	43	65	1151	58	33
3.24A	27624	142	163	5059	146	127
3.24B	248125	43	65	1151	57	33
3.25A	25858	138	159	4947	135	116
3.25B	184130	32	52	887	44	22
3.26A	25231	132	150	4681	135	117
3.26B	209310	37	57	1009	53	29
3.27A	23212	126	141	4412	122	107
3.27B	186092	34	52	867	44	26
3.28A	26992	141	161	4968	145	126
3.28B	237733	39	62	1038	56	32
3.29A	26992	141	161	4968	145	126
3.29B	237733	39	62	1038	56	32
3.30A	5755	24	29	768	22	16
3.30B	39413	14	14	209	10	6
3.31A	10009	35	44	1123	35	34
3.31B	80693	17	21	296	14	8
3.32A	24805	134	155	4825	127	114
3.32B	167286	33	50	867	40	18
3.33A	21137	101	117	3226	106	94
3.33B	201374	38	54	819	46	27
3.34A	21137	101	117	3226	106	94
3.34B	201374	38	54	819	46	27
3.35	209617	170	211	5830	179	138
3.37	35371	43	48	2204	37	31
3.38	32530	43	47	2194	36	32
3.39	32411	43	47	2185	36	31

prior to tornadogenesis to investigate possible lead time on separation between tornadic and non-tornadic storms. They are also analyzed after the last tornado in order to determine whether or not these variables can determine when the tornado threat is over. The number of observations contributing to each box for each plot in Sections 3.1-3.3 can be found in Table 3.1.

3.1 Tornadic vs. Non-Tornadic Storms

Severe storms are known to be characterized by strong upward motion, with many radar- and satellite-based indications of severe storms related to this characteristic. Upward motion within storms can be assessed in these datasets through a variety of established dynamical and physical metrics. Dynamical approaches typically involve using the divergence of the horizontal wind through a column with the assumptions of an anelastic atmosphere (O'Brien, 1970). Strong upper-level divergence located at altitudes above low-level convergence implies strong upward motion due to the conservation of mass in the atmosphere. While the radar and satellite observations can only measure winds within and atop storms, respectively, upward motion can be assessed by analyzing one of these components alone (typically upper-level divergence because the signal is often stronger). Physical metrics to identify and diagnose upward motion include radar-observed weak echo regions and cloud and radar echo-top altitudes (often referenced to a stable boundary such as the tropopause).

The maximum upper-level divergence estimated from both radar and satellite is stronger for tornadic storms, especially when there is a tornado on the ground (Figures 3.1 and 3.2). Time periods prior to only the first tornado in each storm are shown (rather than those prior to all tornadoes) to best isolate unique evolutionary characteristics of tornadic storms before they produce a tornado. Otherwise, time periods between successive tornadoes within a single storm may bias the perceived

evolution in storm-based analyses and corresponding observational indicators of tornado potential. The contrast between the tornadic and non-tornadic storms is greater for the radar-estimated divergence, with clear and consistent differences at times 15 and 30 minutes prior to first tornado occurrence. The divergence declines after the last tornado to values below those prior to the tornadic period. Not only does divergence from radar separate the tornadic and non-tornadic storms, but it can also diagnose when the tornadic storm is no longer a threat. Low-level convergence from radar displays an analogous tendency to the upper-level divergence, but with more overlap between the tornadic and non-tornadic populations (Figure 3.3). This might be due to intermittent or otherwise poor low-level radar coverage.

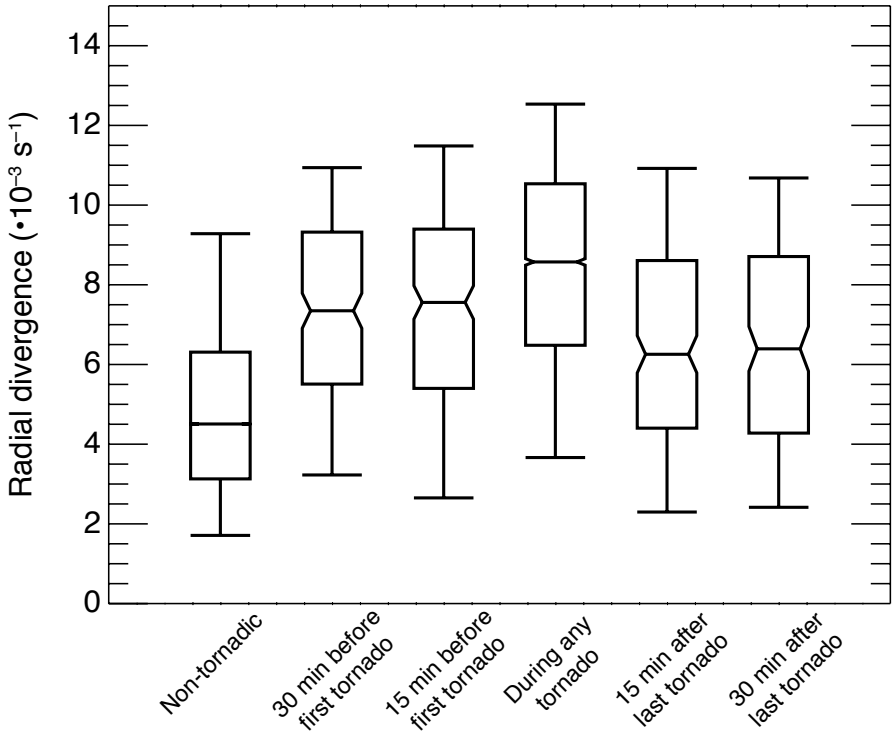

Figure 3.1: Box plot for maximum upper-level radar divergence.

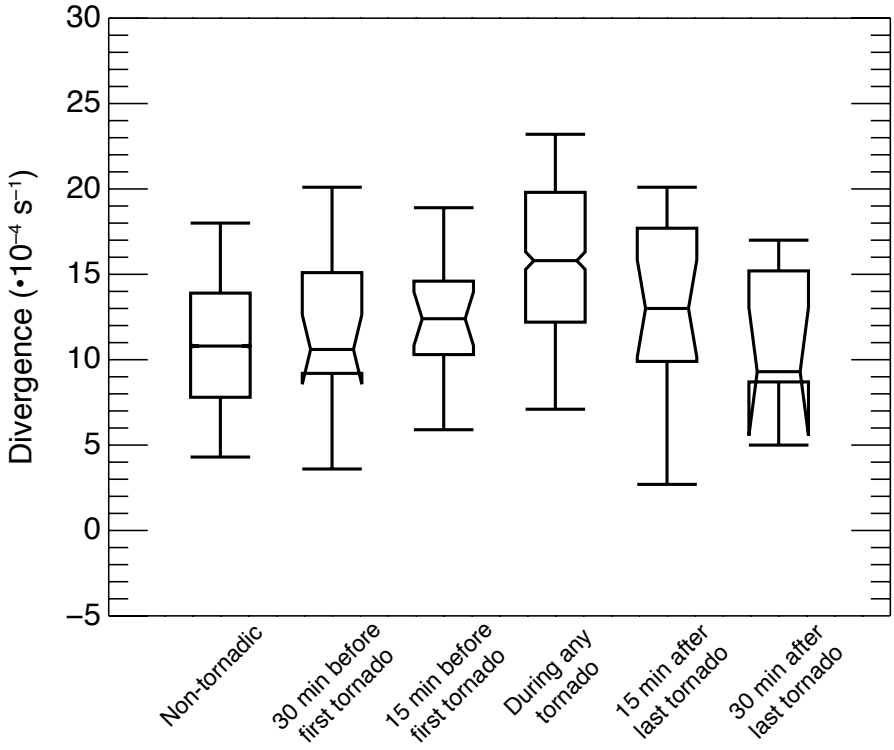

Figure 3.2: Box plot for maximum upper-level satellite divergence.

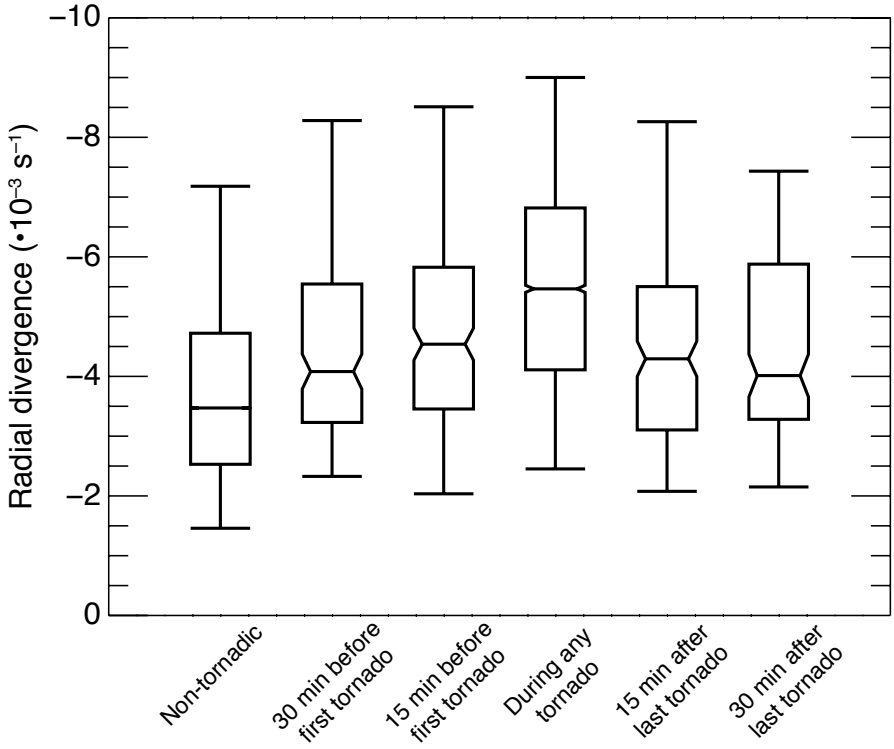

Figure 3.3: Box plot for maximum low-level radar convergence.

Divergence estimates are computed assuming an incompressible atmosphere, which is not precisely representative of the real atmosphere. However, assuming an anelastic atmosphere (scaling by observed atmospheric density with height, which decreases with increasing altitude) provides consistent results, although the mass flux convergence signal is weak (Figures 3.4, 3.5, and 3.6). The process of computing divergence assuming an incompressible atmosphere is slightly faster than when assuming an anelastic atmosphere, which could be of importance when translating the results into a possible nowcasting algorithm. The incompressible assumption might not provide meaningful quantities, but the relative values for tornadic and non-tornadic storms are sufficient to distinguish between the populations. Nevertheless, differences between the divergence estimated from ground-based radar and satellite imagery are likely due to both the limited information detected by satellite (i.e., at cloud top only and the low number of data points) and the differences in the spatial resolution of the two datasets.

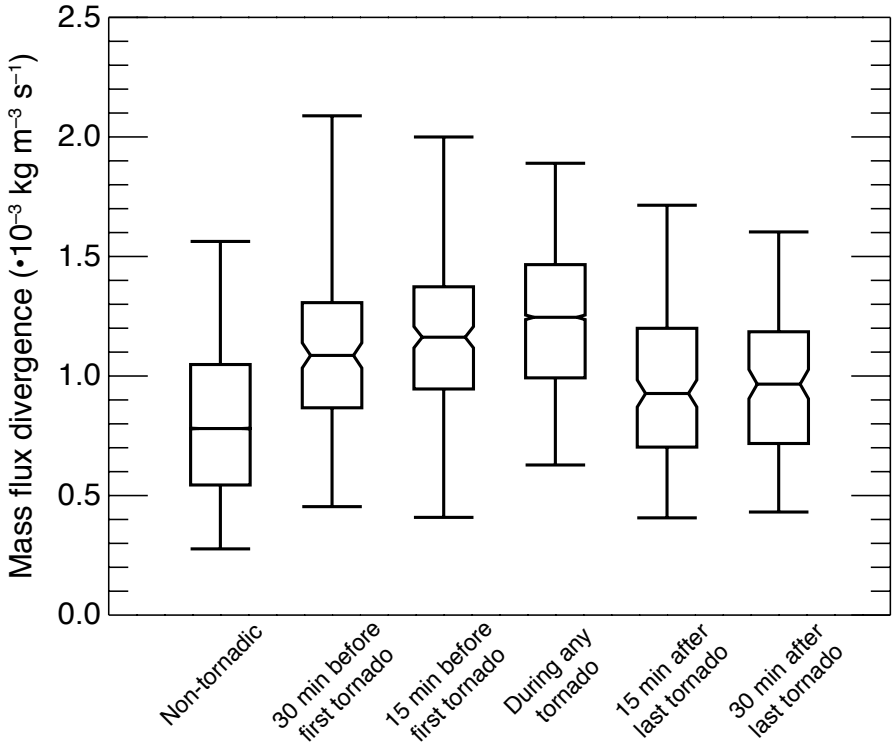

Figure 3.4: Box plot for maximum upper-level radar divergence assuming an anelastic atmosphere.

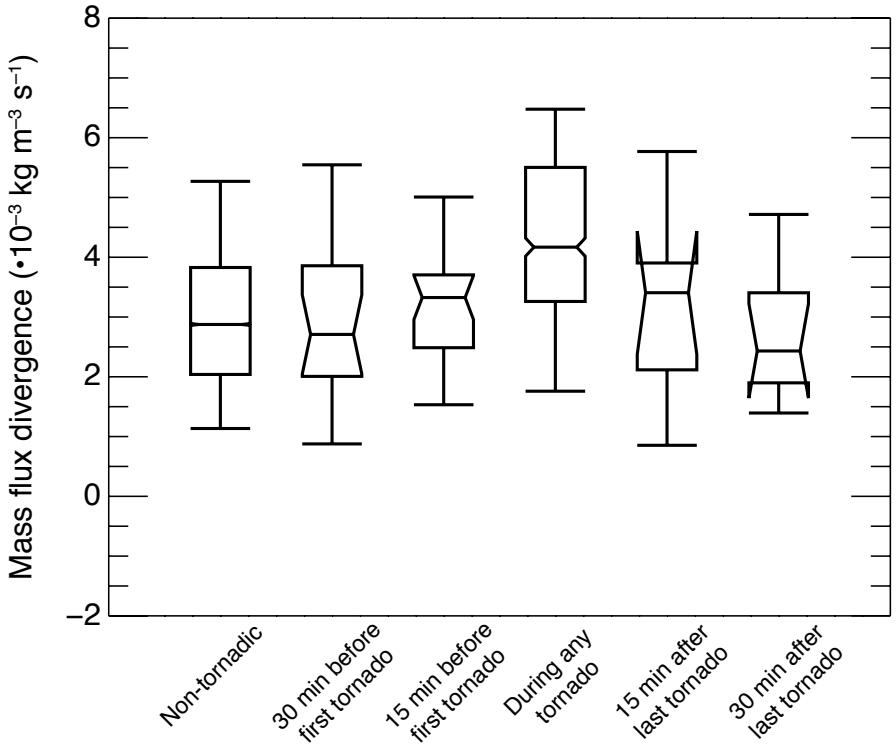

Figure 3.5: Box plot for maximum upper-level satellite divergence assuming an anelastic atmosphere.

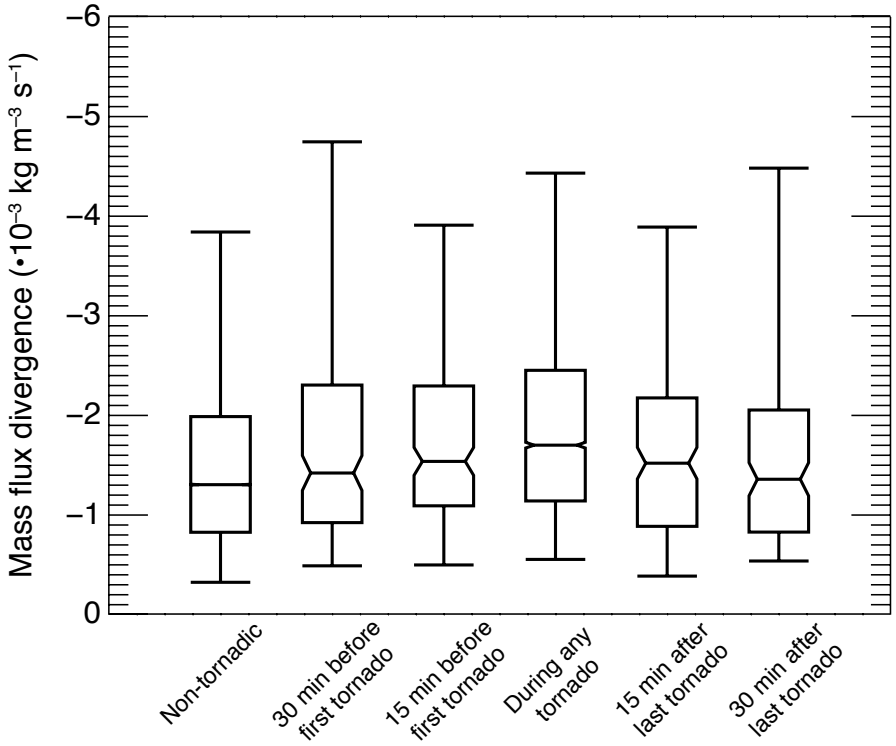

Figure 3.6: Box plot for maximum low-level radar convergence assuming an anelastic atmosphere.

Physical metrics show behavior consistent with that observed from radar and satellite divergence. Radar-observed 40-dBZ echo-top altitudes (the maximum altitude reached by radar-indicated precipitation of considerable size – e.g., large rain drops or ice particles such as hail) imply that tornadic storms have stronger updrafts (Figure 3.7). This is because larger precipitation particles have faster fall speeds, meaning stronger in-cloud vertical motion is required to loft them to higher altitudes. Identifying cloud-top altitudes from satellite is challenging when storms reach the tropopause (commonly the case for storms analyzed in this study) due to the higher temperatures encountered by the cloud top extending into the lower stratosphere, which can bias IR-based cloud-top retrievals low. Alternatively, it is possible to measure the visible texture of the cloud top from satellite to indicate the tropopause-relative depth of OTs (Bedka and Khlopenkov, 2016). A high visible texture rating implies a more complex texture, which has been linked to stronger upward motion and higher cloud tops (Figure 3.8). Indeed, the visible texture rat-

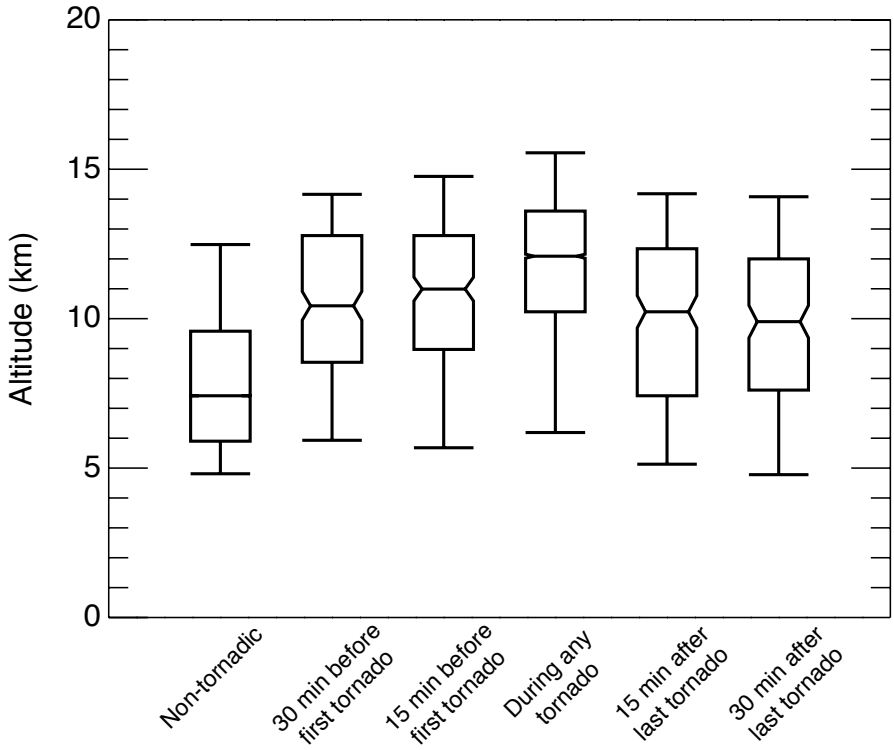

Figure 3.7: Box plot for maximum 40-dBZ echo-top altitude from radar.

ing is also highest in the tornadic storms examined here, providing further evidence of stronger upward motion (Figure 3.9). Tropopause-relative IR cloud-top temperatures show similar characteristics, but less contrast likely due to the 16 times poorer spatial resolution of the IR imagery (compared to the visible imagery) from GOES used in this study (Figure 3.10).

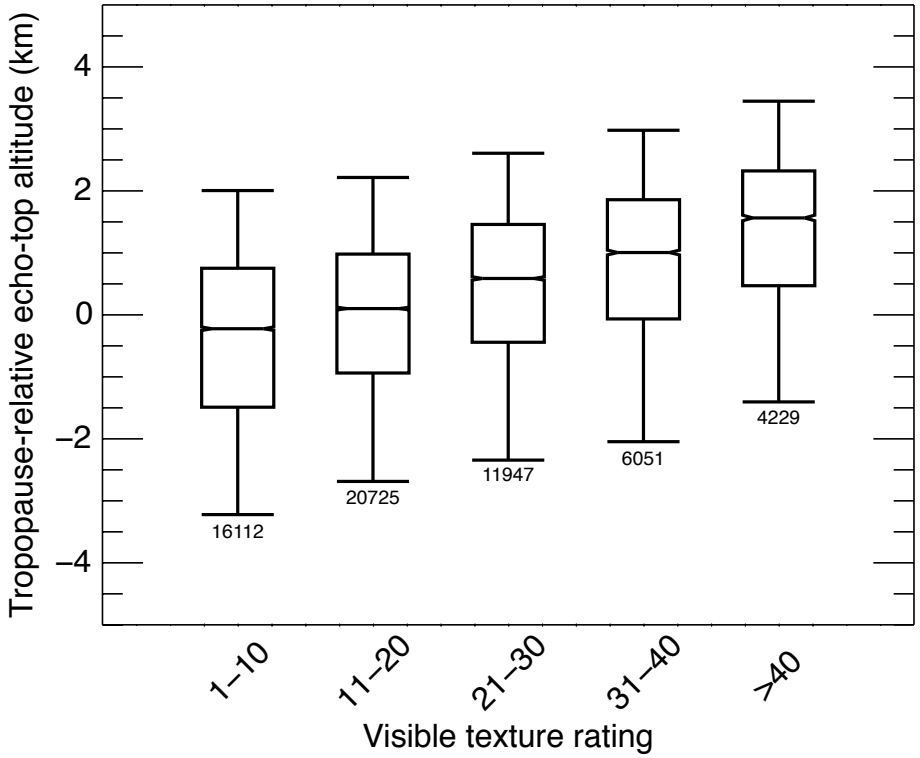

Figure 3.8: Box plot for relationship between visible texture rating and 10-dBZ tropopause-relative echo-top altitudes. Numbers at the base of each box and whisker show the total number of 1-min observations contributing to the distribution.

Two additional metrics that are related to upward motion in storms are shown to provide further evidence of a unique relationship between tornadic storms and upward motion. As upward motion increases within a storm, stretching of air within the main storm updraft leads to increases in vertical vorticity relative to storms with weaker updrafts (Markowski and Richardson, 2009), which is demonstrated well in the radar observations of rotation, especially in the upper-levels

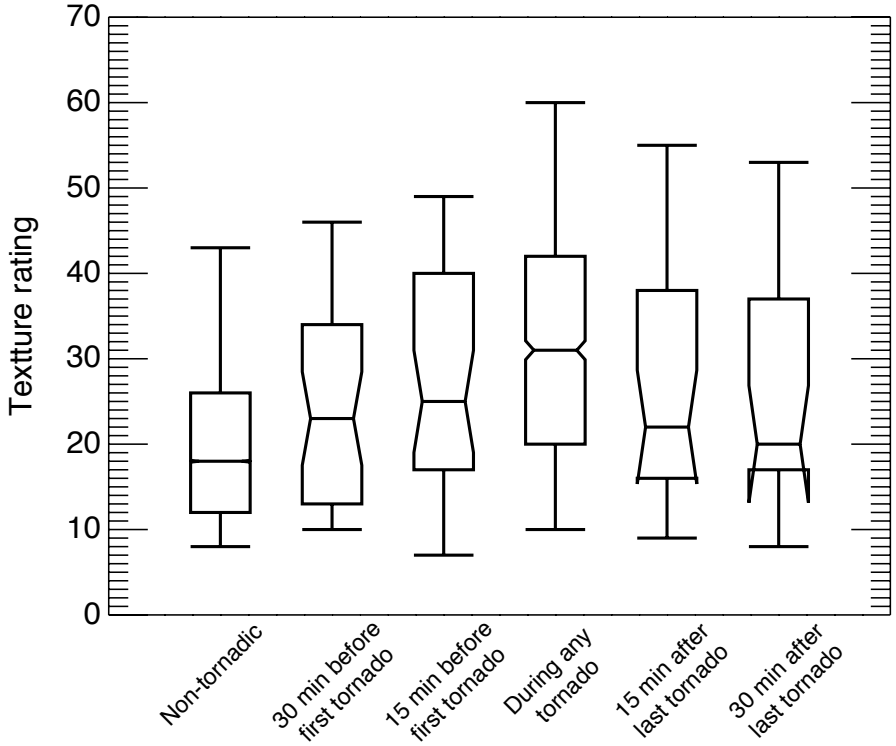

Figure 3.9: Box plot for maximum visible texture rating from satellite.

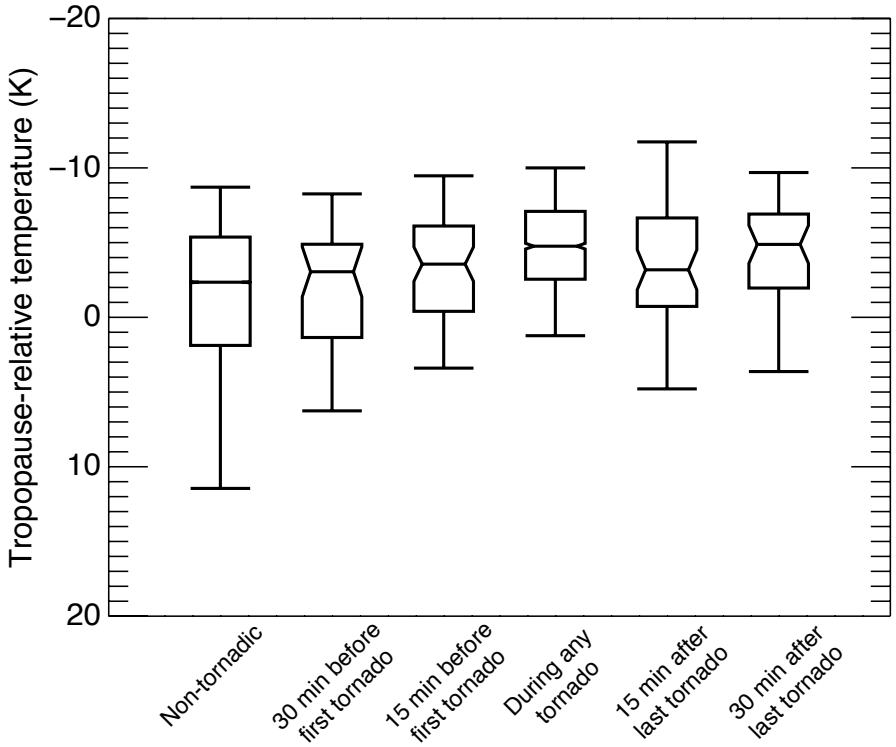

Figure 3.10: Box plot for minimum tropopause-relative IR brightness temperature from satellite.

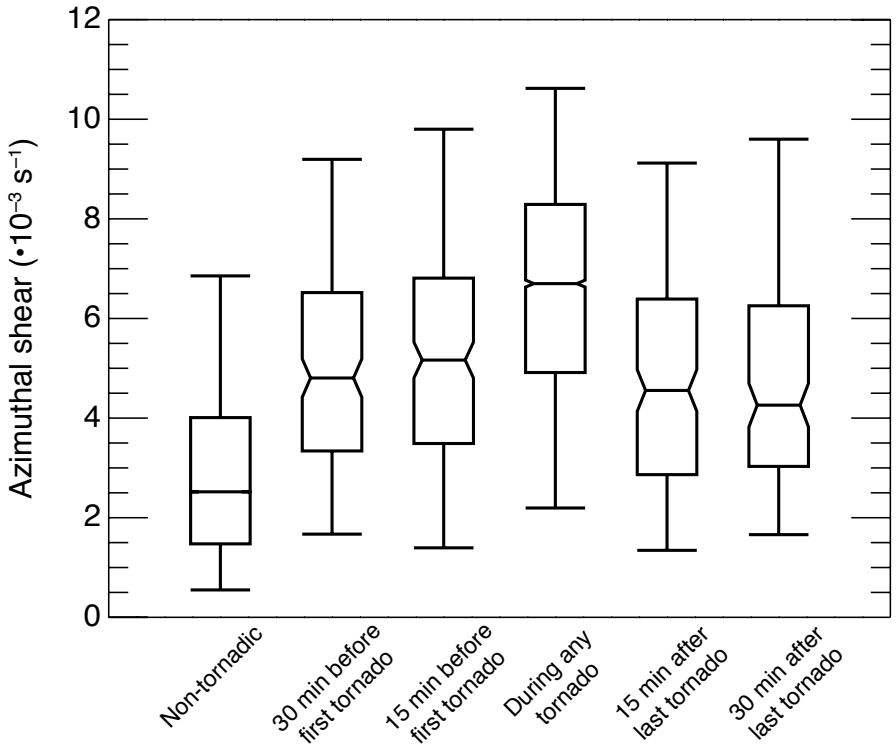

Figure 3.11: Box plot for maximum upper-level radar rotation.

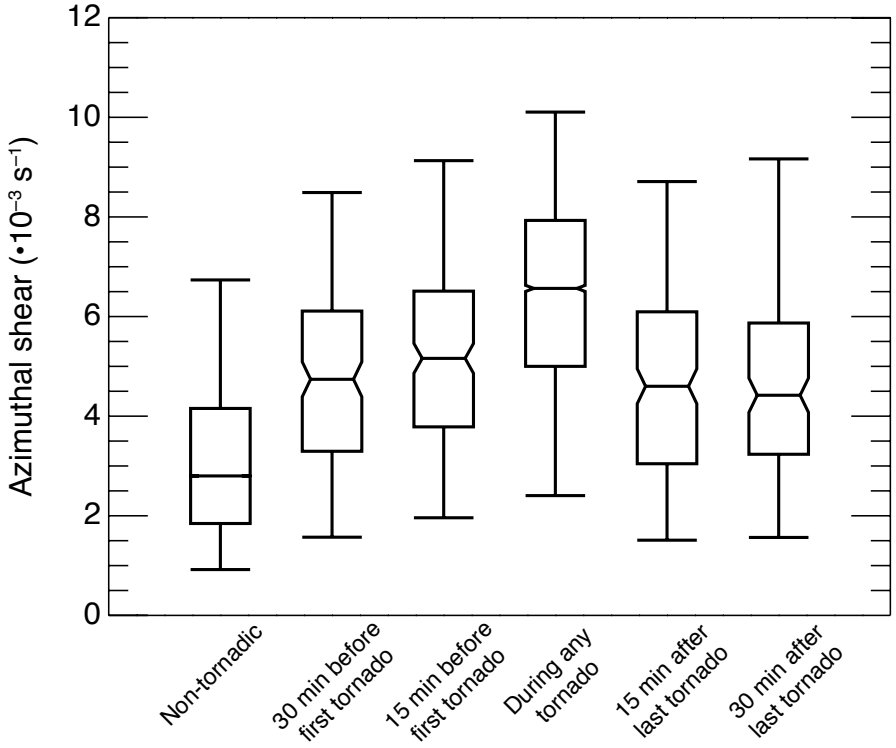

Figure 3.12: Box plot for maximum mid-level radar rotation.

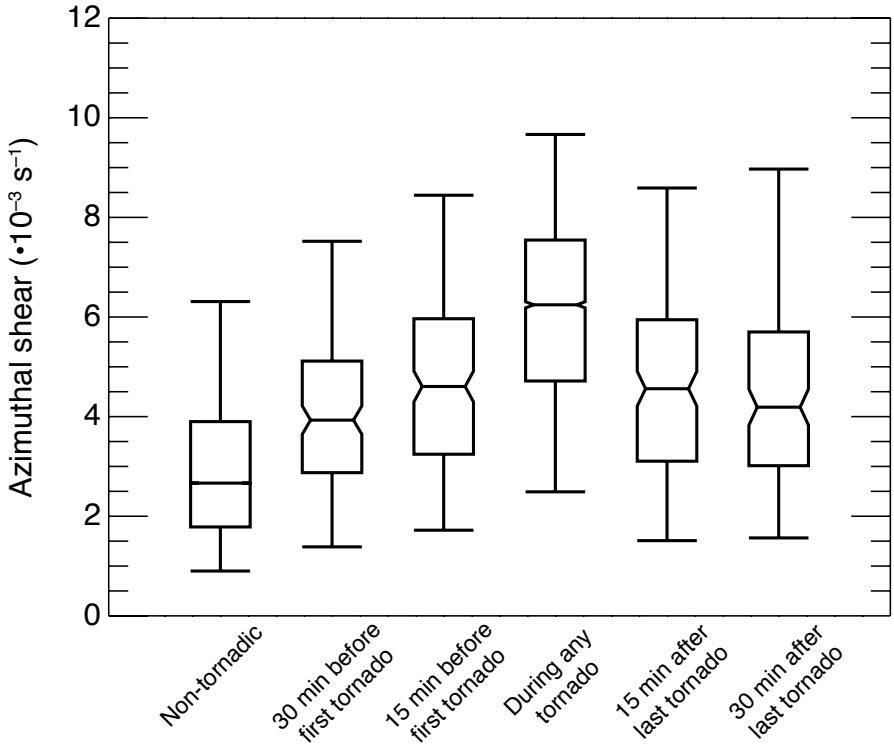

Figure 3.13: Box plot for maximum low-level radar rotation.

(Figures 3.11, 3.12, and 3.13). Stronger upward motion also has implications for lightning activity. When upward motion in the mixed-phase (liquid and ice) region of a cloud increases, the non-inductive charging mechanism typically becomes more efficient and thus, lightning flashes become more frequent (Deierling and Petersen, 2008). Data from the Earth Networks Total Lightning Network (ENTLN) in the United States (Liu and Heckman, 2011) for eight of the GOES-14 severe weather days evaluated here show that flash density is indeed greater in tornadic storms, especially during tornadoes (Figure 3.14). This result is comparable to the so-called "lightning jump" discussed in previous studies (Williams et al., 1999; Schultz et al., 2009). Increased lightning activity and low-to-mid-altitude rotation are currently being used as variables of interest for probabilistic forecasts of tornadoes (Smith et al., 2016). However, the upper-level metrics of upward motion and rotation used here show greater separation between non-tornadic and tornadic storms at longer lead times (compare 30 and 15 minutes prior to first tornado in

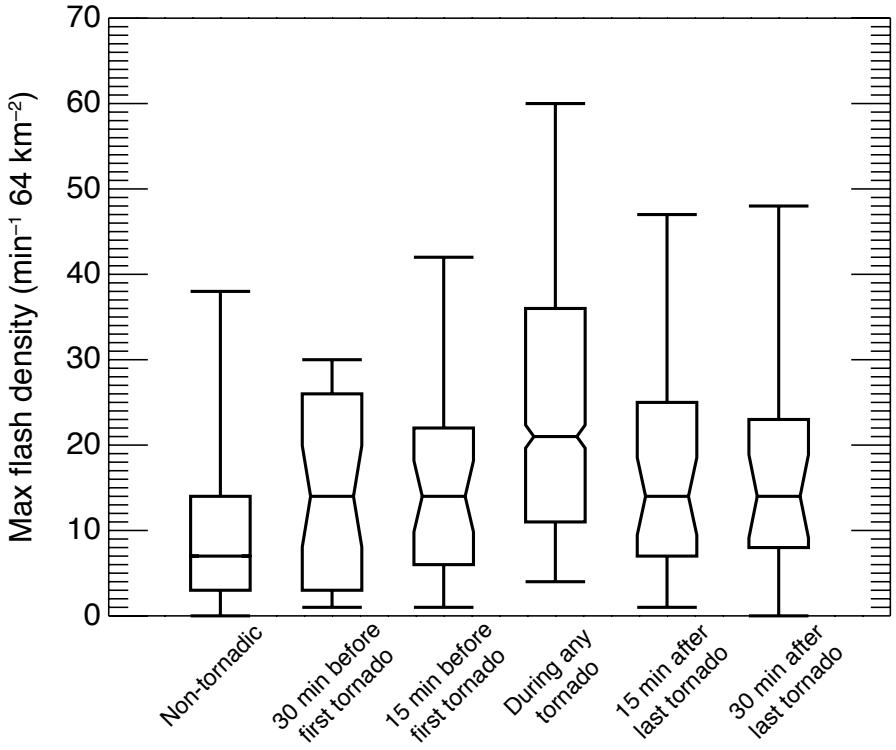

Figure 3.14: Box plot for maximum ENTLN total lightning flash density.

Figures 3.1 and 3.11 to that in Figures 3.12, 3.13, and 3.14). The overall rotation is also less useful than radar divergence when judging whether a tornadic storm is done producing tornadoes or not, though the upper-level rotation is the most helpful of the three.

Another quantity that can be related to the updraft strength is the velocity spectrum width. High velocity spectrum width will occur near wind shifts or in areas of high turbulence (such as that which occurs within convective updrafts). Indeed, the column maximum velocity spectrum width mirrors the behavior of the divergence and rotation for the tornadic and non-tornadic storms (Figure 3.15).

The updraft strength itself is also evaluated, both for the maximum and median within a storm calculated from the divergence profile using the incompressible assumption (Figures 3.16 and 3.17). The maximum and median implied ascent from divergence are very similar, but the maximum for tornadic storms is slightly more separated from the non-tornadic population than the median.

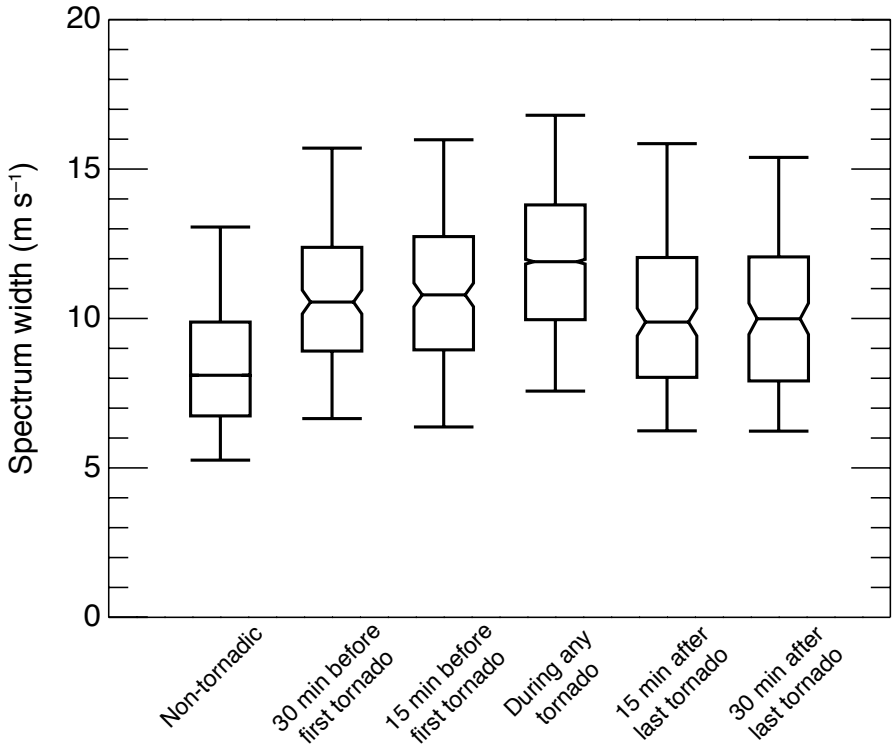

Figure 3.15: Box plot for maximum column maximum spectrum width.

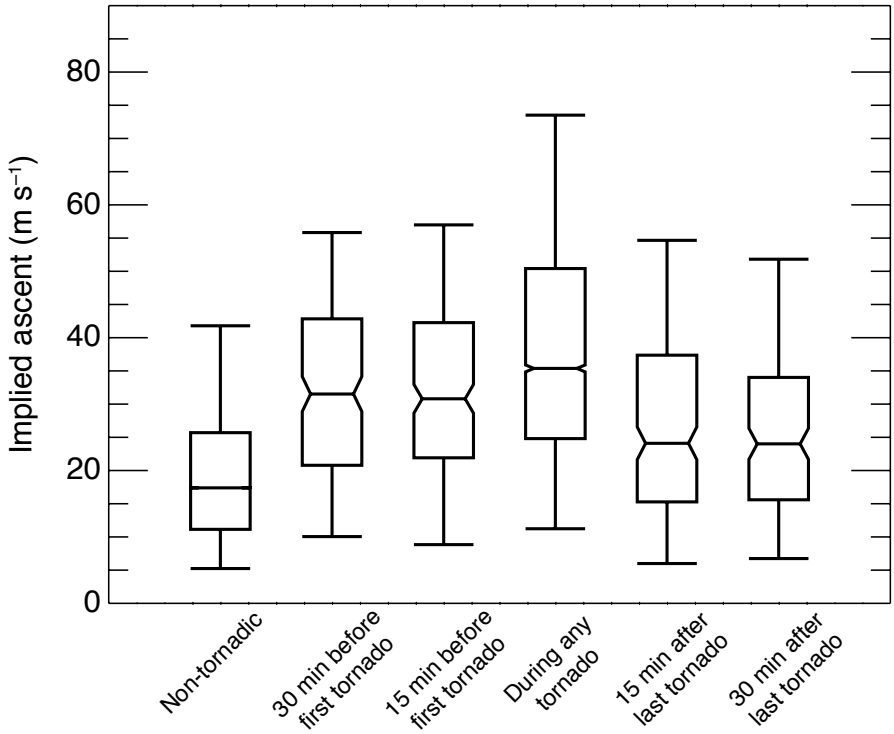

Figure 3.16: Box plot for maximum implied ascent.

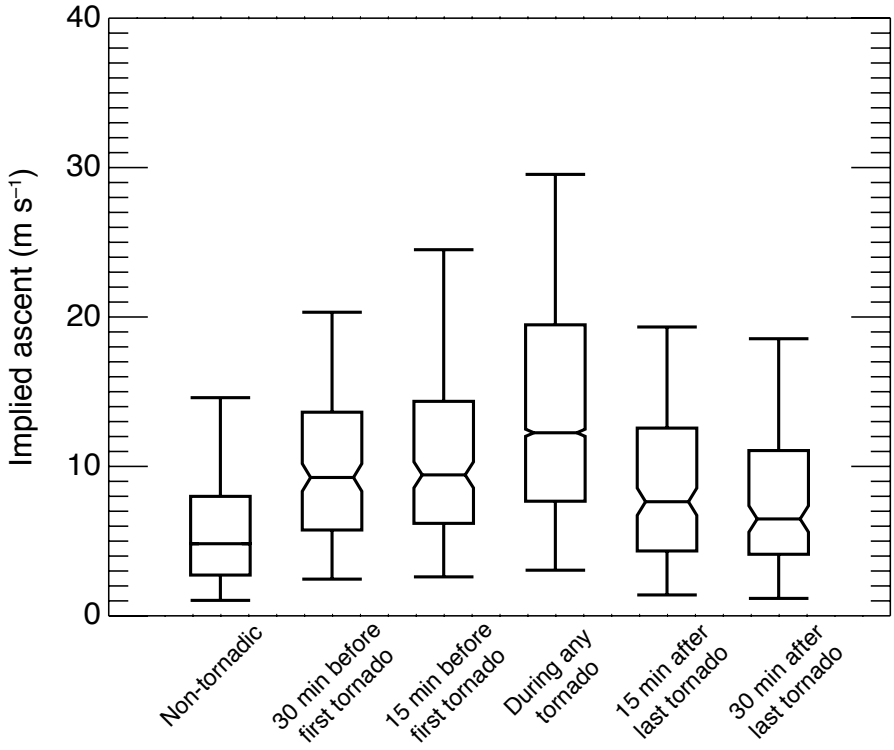

Figure 3.17: Box plot for median implied ascent.

Updraft width, here quantified by the area of implied ascent exceeding a certain threshold, was examined as well (Figure 3.18). Due to the 10-km radius restriction in the data belonging to a specific storm, there is an upper limit to the implied ascent area just below 400 km^2. This analysis shows that a storm with a wider updraft is more likely to be able to produce a tornado.

Correlation coefficient is lower for tornadic periods, which can be a sign of a stronger updraft (Figure 3.19). However, the signal is not very strong, and there is no way to tell if a tornadic storm no longer has a potential for producing a tornado within a reasonable time frame. Differential reflectivity is also lower for tornadic storms, and shows a larger gap in the values for non-tornadic and tornadic storms (Figure 3.20). This could just be an indication that hail is more likely when a storm is capable of producing a tornado, which is usually a microphysical indication of a stronger updraft, since large hail stones require an updraft of a certain strength to form (e.g., Nelson, 1983).

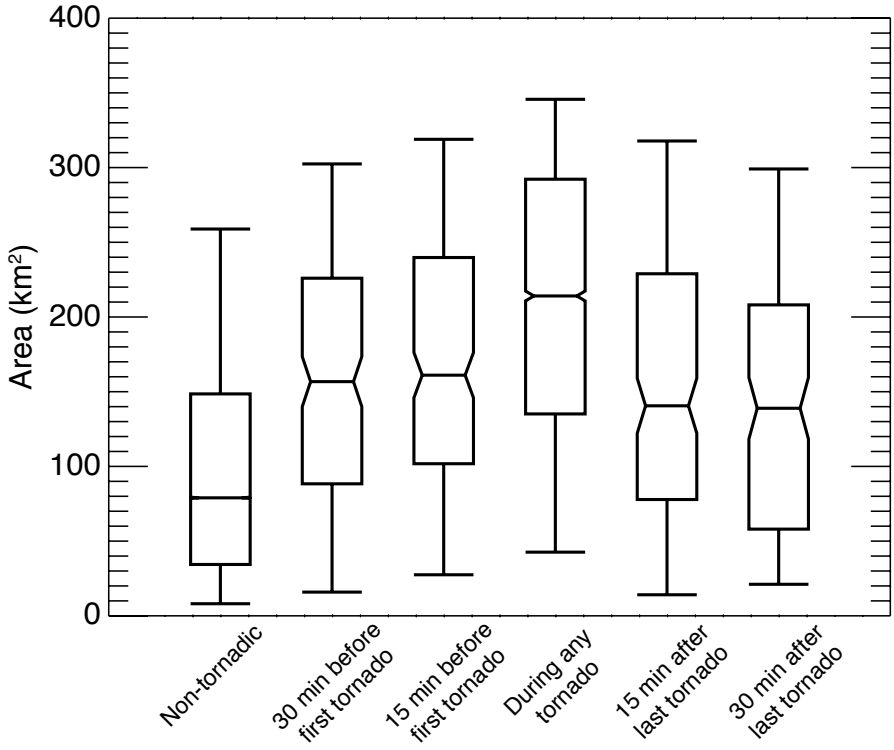

Figure 3.18: Box plot for area of implied ascent ≥ 10 m s^{-1}.

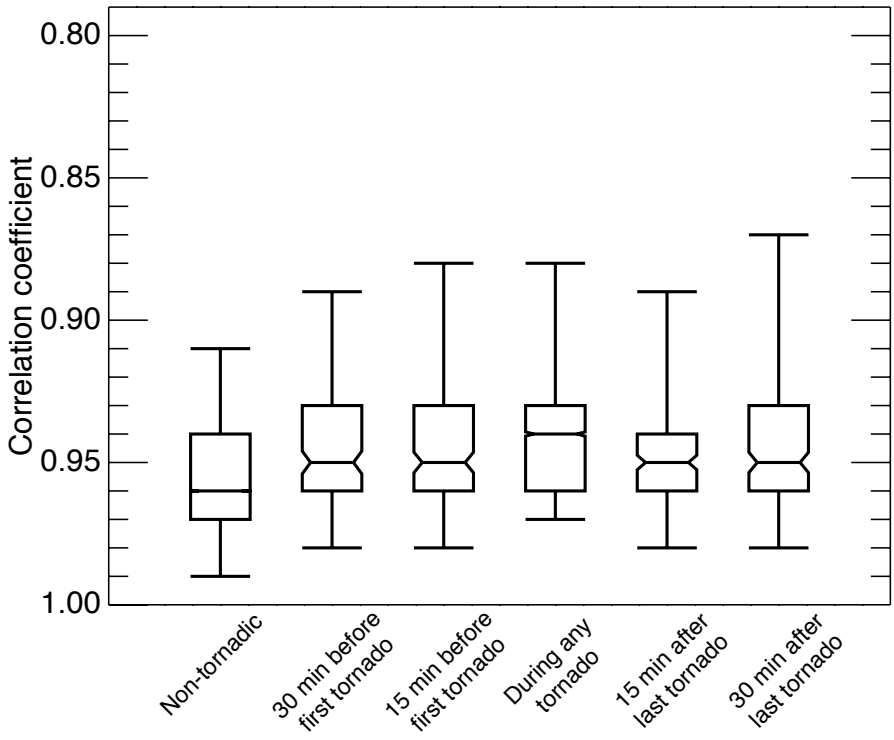

Figure 3.19: Box plot for minimum correlation coefficient.

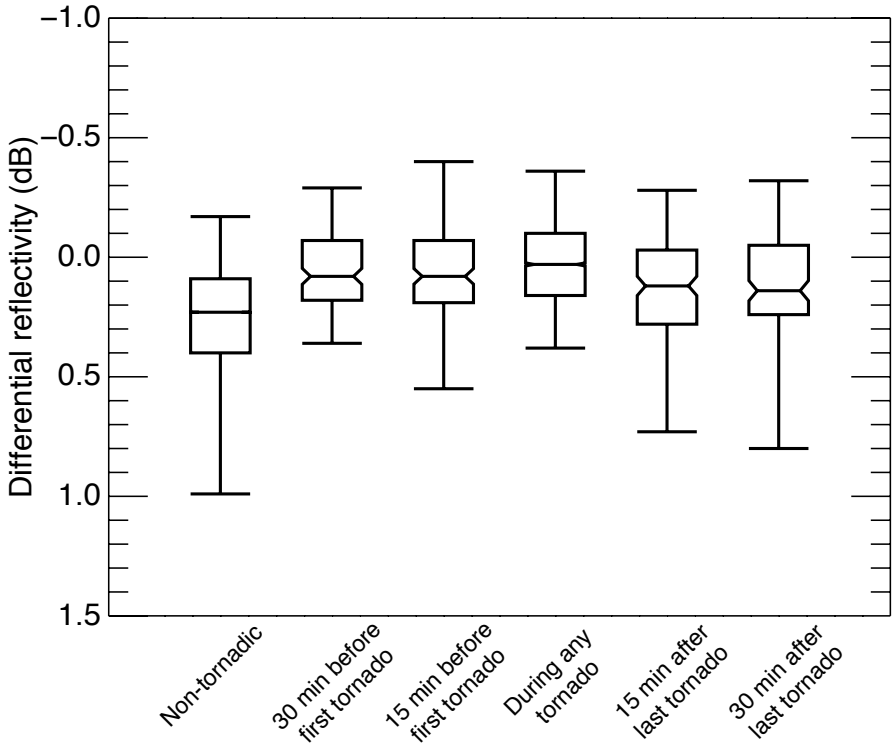

Figure 3.20: Box plot for minimum differential reflectivity.

Some of the variables have certain limitations or conditions associated with them. The farther the distance from the radar, the more error is possibly introduced in the variables, especially the wind derivatives and the polarimetric variables. As the distance from the radar increases, the radar beam height increases, making the derivative less of a horizontal derivative with distance from the radar. In addition, dual-polarization variables become less indicative of particle shape and the winds will gain more of an vertical component as the elevation increases. Also, the low-level coverage suffers from the increase in beam height with distance. Due to the definition of the upper levels being at or above 8 km, upper-level measurements will be missing for storms that do not exceed 8 km. This might introduce potential missed observations of tornadic storms, especially for non-supercell storms that might be relatively shallow. Additionally, the visible texture rating only applies to storms with an overshooting top, and while many severe storms have overshooting tops, Dworak et al. (2012) found that the number

of overshooting tops only adds up to less than half of the storms linked to severe weather reports. Another factor that can bias these results is under-reporting of tornadoes, especially in rural areas (e.g. Anderson et al., 2007). If storms were incorrectly categorized as non-tornadic, the separation between the tornadic and non-tornadic populations might have been smaller than the reality.

3.1.1 Supercells and Non-Supercells

A majority of the storms that produce tornadoes are supercells, which are typically isolated storms that are characterized by deep, rotating updrafts (Doswell and Burgess, 1993). This is true for the population of tornadic storms analyzed in this study (see Table 2.1), where 206 out of 335 tornadic storms were identified as discrete supercells. For this section, where the Super Outbreak of April 2011 is excluded, 273 tornadic storms were analyzed, where 172 were supercells, with 363 supercells overall. Not all supercell storms produce tornadoes, and non-tornadic supercell storms are typically stronger than non-tornadic, non-supercell storms. It is therefore appropriate to separately examine supercell and non-supercell storms to confirm that the differences in upward motion inferred from the analyses of the entire storm population are qualitatively similar. Due to the limited 1-minute satellite data for supercells available to this study, comparisons of supercell and non-supercell storms are accomplished using data that was available for a majority of the cases only.

Tornadoes produced by non-supercell systems like mesoscale convective systems (MCSs) are notoriously hard to forecast, with a recent example of the EF2 Tulsa tornado in August 2017 that was not warned prior to the tornadogenesis. Several of the metrics evaluated here show separation between tornadic and non-tornadic storms for even non-supercell storms half an hour before tornadogenesis. Notably, both dynamical and physical metrics within each storm population show consistent

behavior with the overall analysis (i.e., stronger upper-level divergence and rotation and higher echo-top altitudes in tornadic storms), with greater values overall observed within supercell storms (Figures 3.21 through 3.31). While there is more of a contrast in low-level rotation between tornadic and non-tornadic supercell storms when there is a tornado present, the upper-level rotation values for the tornadic supercell storms start to diverge from the general non-tornadic values at an earlier time relative to the first tornado (Figures 3.25 and 3.27). Interestingly, visible texture rating from satellite gives a longer lead time for non-supercell storms, and the minimum IR brightness temperature shows more promise for isolating the tornadic supercells from non-tornadic supercells than separating the populations overall (Figures 3.30 and 3.31).

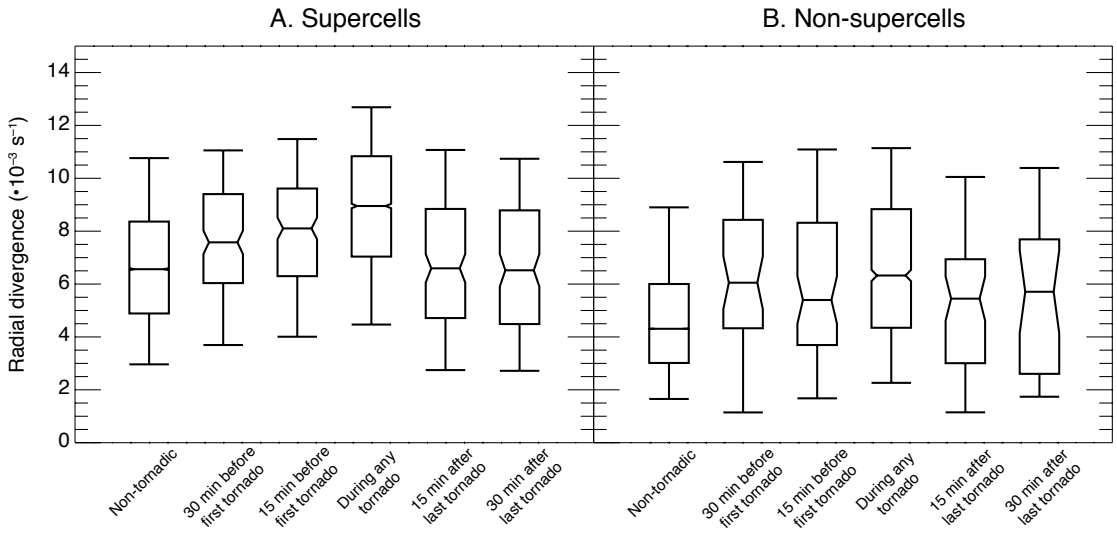

Figure 3.21: Box plot for maximum upper-level radar divergence for supercells and non-supercells.

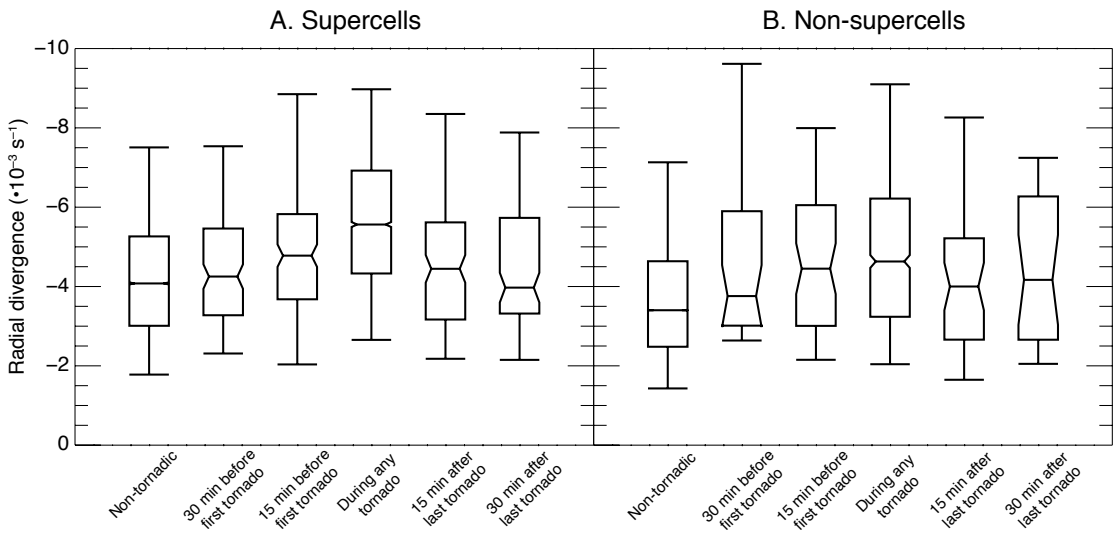

Figure 3.22: Box plot for maximum low-level radar convergence for supercells and non-supercells.

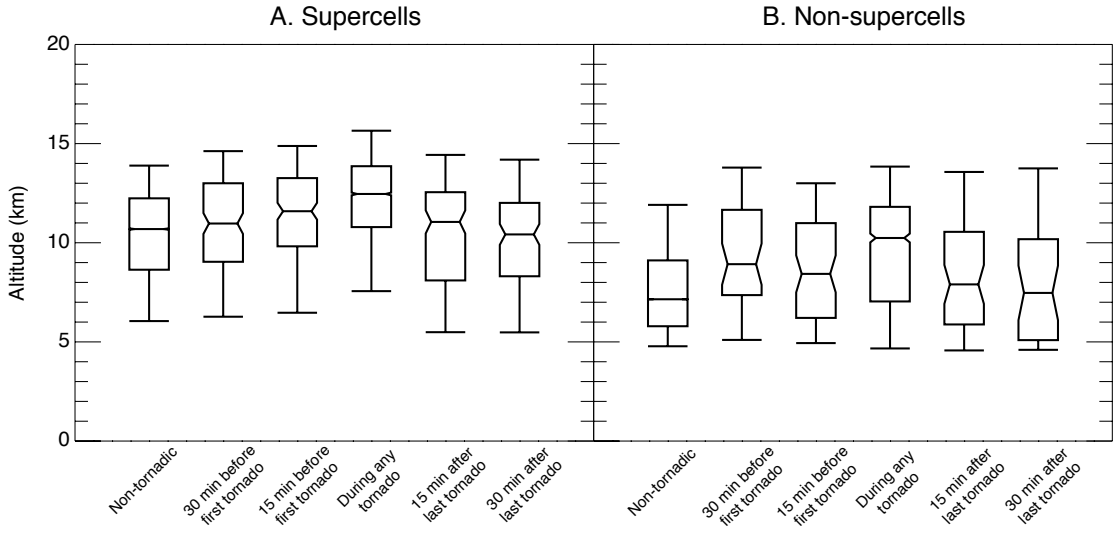

Figure 3.23: Box plot for maximum 40-dBZ echo-top altitude for supercells and non-supercells.

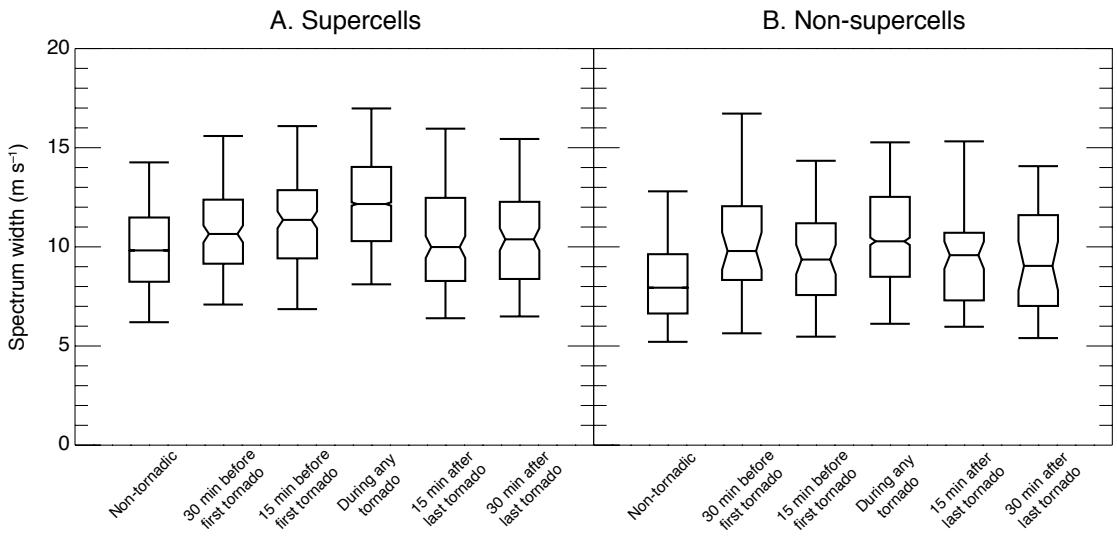

Figure 3.24: Box plot for maximum column maximum spectrum width for supercells and non-supercells.

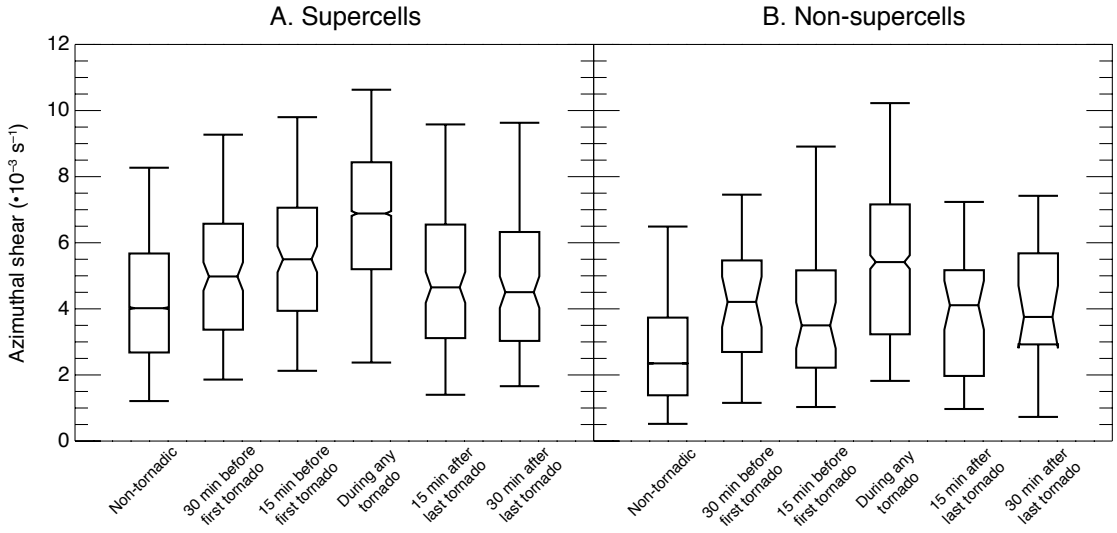

Figure 3.25: Box plot for maximum upper-level radar rotation for supercells and non-supercells.

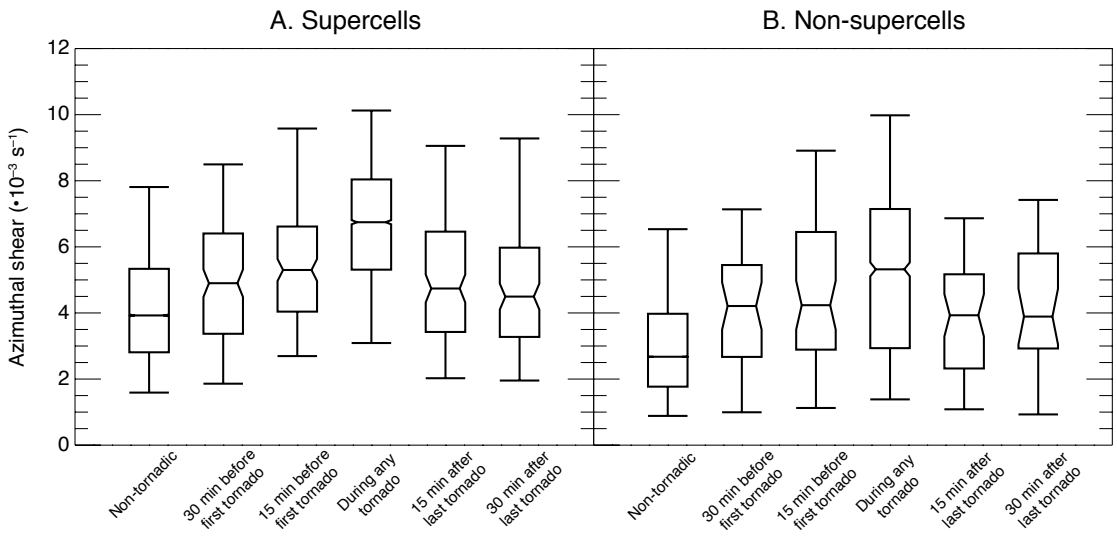

Figure 3.26: Box plot for maximum mid-level radar rotation for supercells and non-supercells.

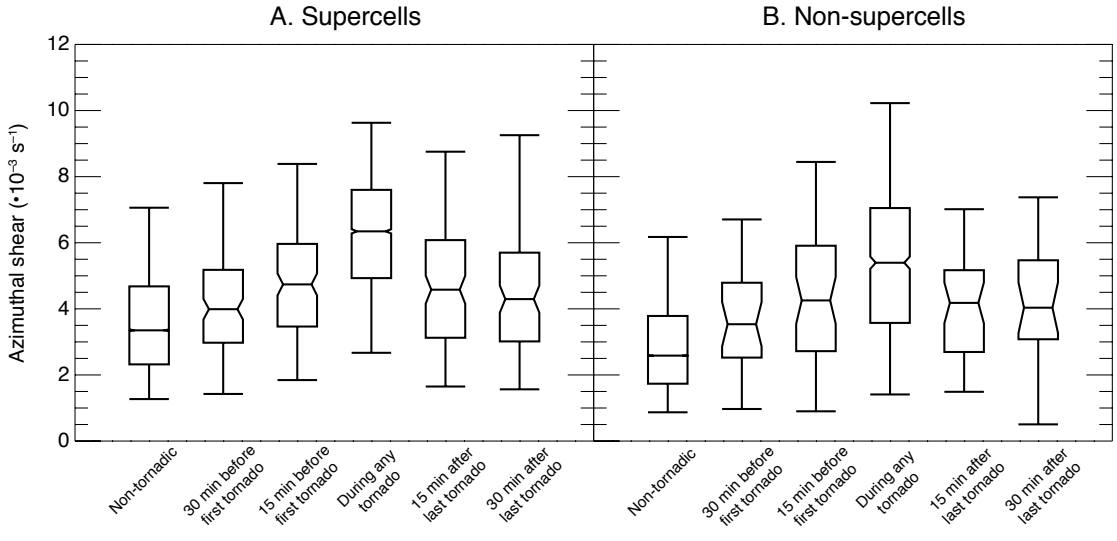

Figure 3.27: Box plot for maximum low-level radar rotation for supercells and non-supercells.

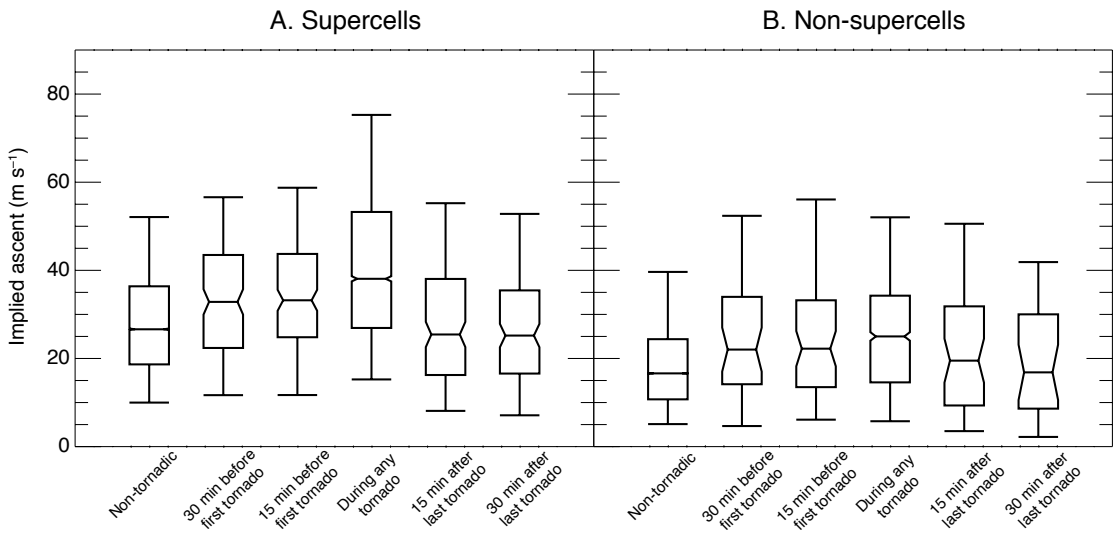

Figure 3.28: Box plot for maximum implied ascent for supercells and non-supercells.

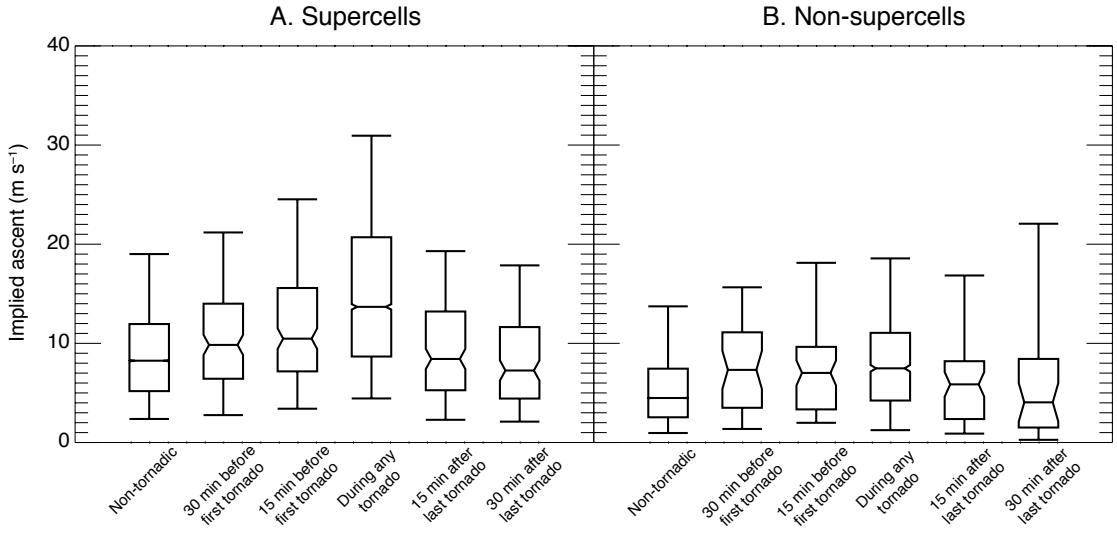

Figure 3.29: Box plot for median implied ascent for supercells and non-supercells.

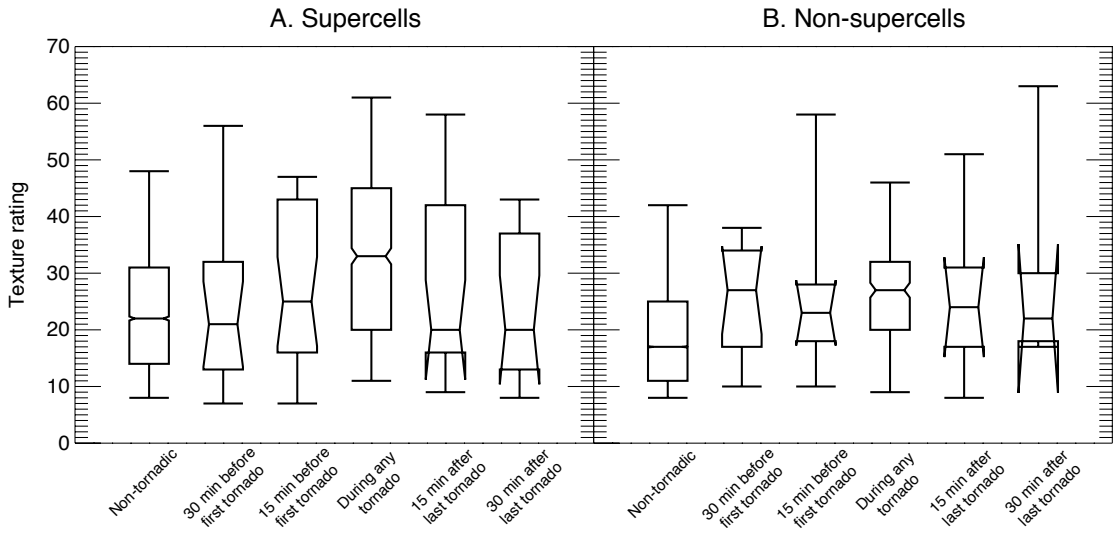

Figure 3.30: Box plot for maximum visible texture rating from satellite for supercells and non-supercells.

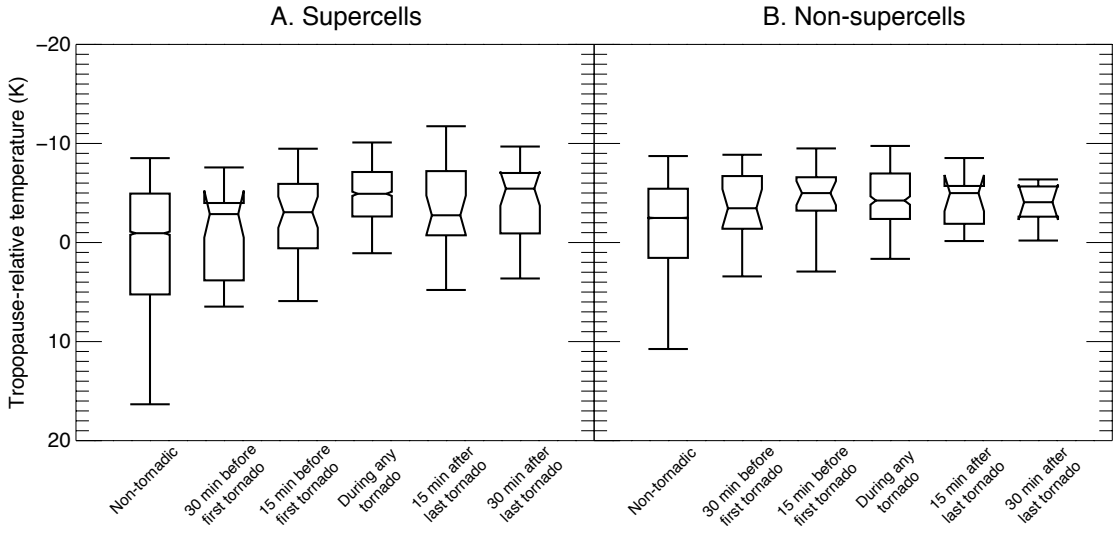

Figure 3.31: Box plot for minimum tropopause-relative IR brightness temperature from satellite for supercells and non-supercells.

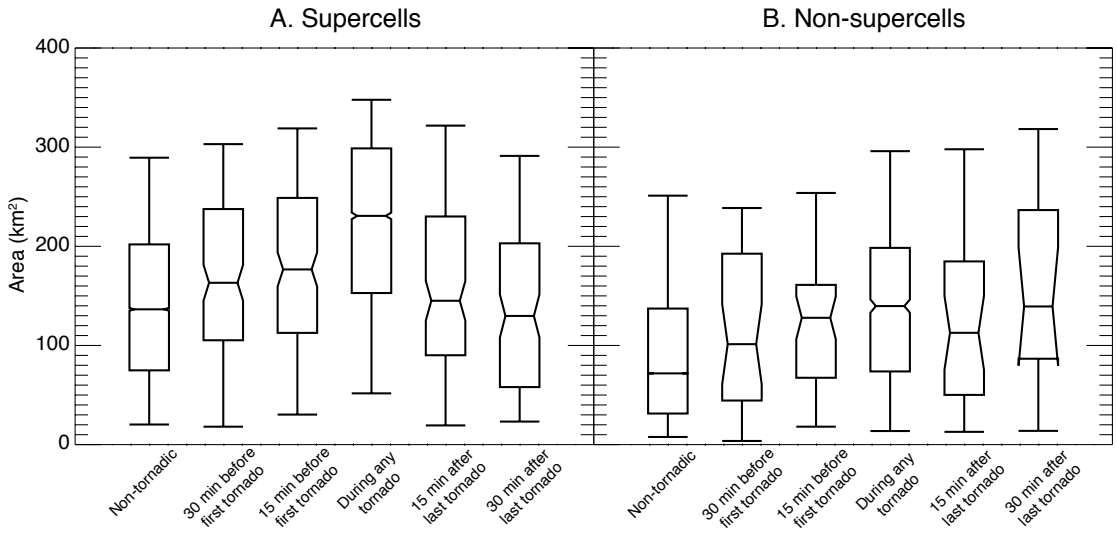

Figure 3.32: Box plot for area of implied ascent ≥ 10 m s^{-1} for supercells and non-supercells.

While the results for the updraft width for supercells are consistent with the overall storms, it is not as clear for non-supercells (Figure 3.32). Updraft width for non-supercells could perhaps benefit from a smaller implied ascent threshold for the calculation of the area, as it has shown promise in subjective analyses of individual storms as a discriminator for tornadic storms when compared to surrounding non-tornadic storms.

The tendency in minimum correlation coefficient was also similar for the overall analysis and the supercells, but the tornadic non-supercells show much lower minima (Figure 3.33). This indicates that correlation coefficient could be a good discriminator for tornadic storms in non-supercells, but a problem with using a pure minimum threshold in ρ_{HV} to identify tornadic storms alone is that it could also be a sign of unrelated non-meteorological scatterers. This is addressed in this study by only analyzing ρ_{HV} in areas where the reflectivity is greater than 45 dBZ. Whereas the correlation coefficient show different results for supercells and non-supercells, the other polarimetric variable, Z_{DR}, is showing similarities for all the analyses (Figure 3.34).

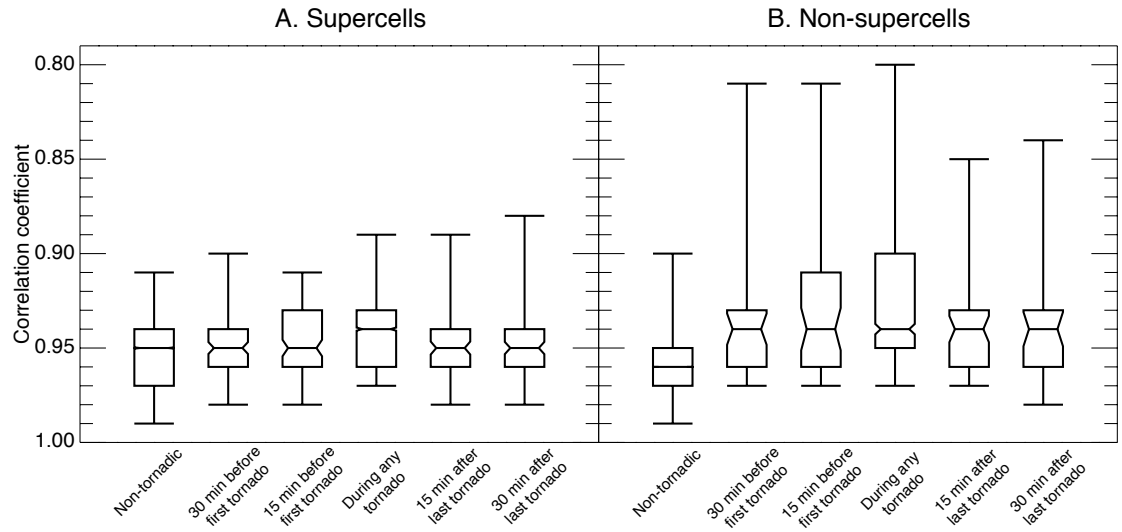

Figure 3.33: Box plot for minimum correlation coefficient for supercells and non-supercells.

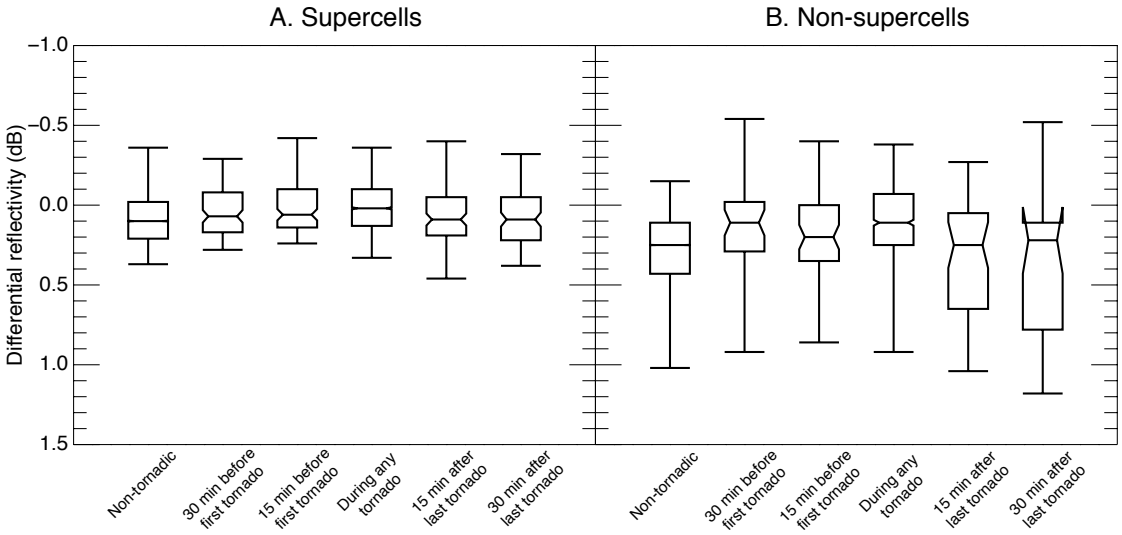

Figure 3.34: Box plot for minimum differential reflectivity for supercells and non-supercells.

3.2 Evaluation of a Simple Objective Short-Term Forecast Product

The observed relationship between strong upward motion and tornadic storms at times prior to and during the occurrence of tornadoes motivates an evaluation of the ability of a simple objective technique to identify storms capable of producing tornadoes before they occur. Toward this end, the product of two radar-observed dynamical metrics is computed: upper-level divergence and rotation (Figure 3.35). Storms that exceed a single threshold value of this product for a specified time period are flagged as potentially tornadic and the time at which the condition is met is recorded. For a predictive model, the resulting probability of detection (POD) and false alarm ratio (FAR) forecast skill metrics for the storm population are then computed by Equations 3.1 through 3.4.

$$\text{POD} = \frac{\text{No. correctly flagged storms}}{\text{No. tornadic storms}} \tag{3.1}$$

$$\text{FAR} = \frac{\text{No. incorrectly flagged storms}}{\text{No. storms flagged}} \tag{3.2}$$

$$\text{CSI} = \left(\frac{1}{1-\text{FAR}} + \frac{1}{\text{POD}} - 1\right)^{-1} \tag{3.3}$$

$$\text{Bias} = \frac{\text{POD}}{\text{1 - FAR}} \tag{3.4}$$

Mean and median lead times of the potentially-tornadic flag relative to the first occurrence of a tornado (hereafter the flag lead time) within each storm are also computed. To provide context for this objective method, results are compared with the first tornado warning given to each storm by the responsible National Oceanic

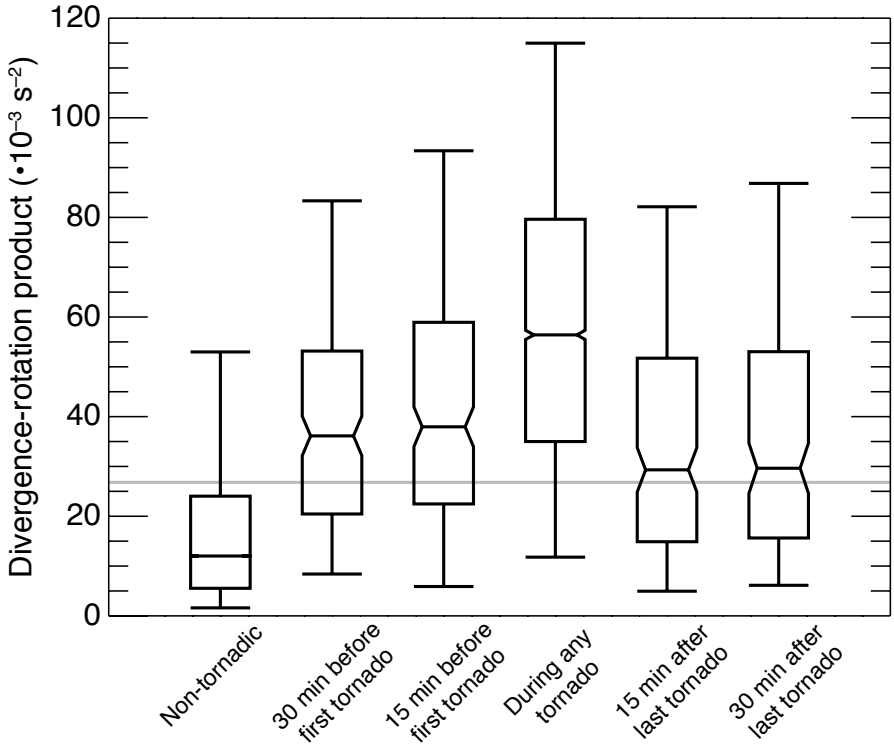

Figure 3.35: Box plot for radar-derived upper-level divergence-rotation product.

and Atmospheric Administration (NOAA) National Weather Service (NWS) forecast office, which serves as a metric of the first public recognition that a storm was potentially tornadic by forecasters.

The single radar-derived rotation-divergence product threshold used for comparison with NWS performance was chosen to match the skill (or critical success index – CSI) of the NWS for the cumulative performance of all 27 severe weather days ($34{\cdot}10^{-3}$ s^{-2}; see Figures 3.35 and 3.36A), though many other configurations were investigated. A 5-minute time period of exceedance was deemed sufficient for the objective technique, since the product did not appear to be affected negatively by random time variations (compare multiple time periods of exceedance in Figure 3.36A).

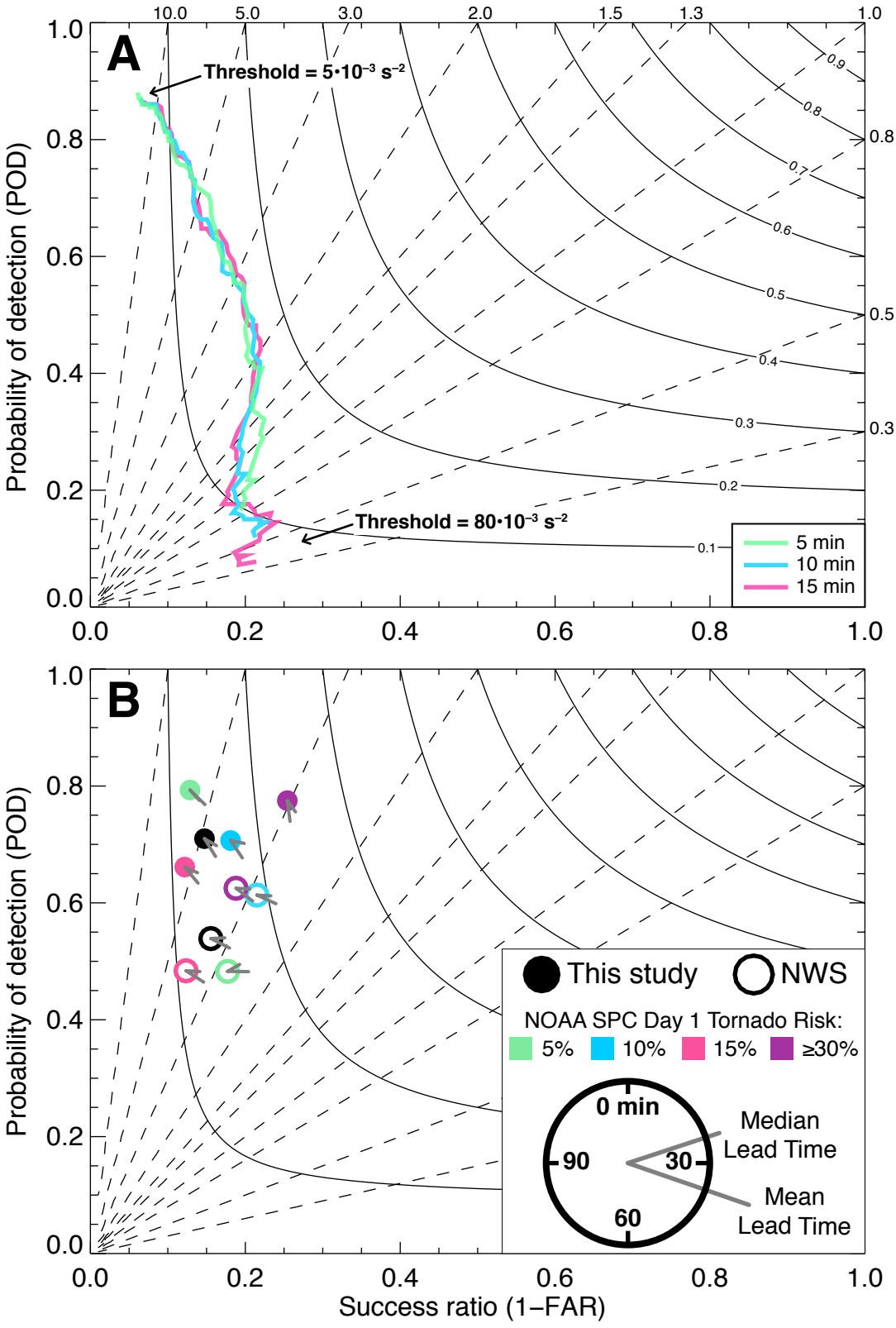

Figure 3.36: Performance diagrams.

Figure 3.36 shows performance diagrams for the objective and NWS warning-based methods. Solid black lines are lines of constant CSI. The dashed lines represent bias, where values >1 signify over-forecasting and values <1 signify under-forecasting. Subplot A shows performance of the objective method at multiple time periods of exceedance for divergence-rotation product threshold values ranging from $5 \cdot 10^{-3}$ to $80 \cdot 10^{-3}$ s^{-2}. Subplot B compares the equivalent-CSI objective method (filled circles) to the performance of the NWS warning-based method (open circles). Black circles show the cumulative performance for all severe weather days, while the colored circles show the performance for days grouped by NOAA Storm Prediction Center (SPC) Day 1 outlook for tornado risk (the forecast probability of a tornado occurring within 25 miles of any point). Gray lines atop each circle represent median and mean lead times. (See Table 3.2 for point values in panel B.)

Table 3.2: Values of the performance metrics shown in Figures 3.36 and 3.40. NWS values are in parentheses.

	POD (%)	FAR (%)	Mean flag lead time (min)	Median flag lead time (min)
27 cases	70.98 (53.89)	85.28 (84.45)	49.4 (38.9)	40 (29)
5% risk	79.31 (48.28)	87.15 (82.28)	44.7 (30.3)	46 (20)
10% risk	70.67 (61.33)	81.91 (78.50)	48.7 (38.1)	34 (31)
15% risk	66.13 (48.38)	87.83 (87.65)	46.8 (40.9)	38 (31)
≥30% risk	77.50 (62.50)	74.59 (81.20)	57.5 (42.5)	48 (31)
Super Outbreak	77.08 (87.50)	72.40 (82.35)	72.6 (63.6)	56 (51)

A perfect forecast has a 100% POD, 0% FAR, and a CSI of 1. For objective upper-level divergence-rotation thresholds ranging from $5{\cdot}10^{-3}$ s^{-2} to $80{\cdot}10^{-3}$ s^{-2} applied to data from all 27 severe weather days, the CSI largely varies between 0.1 and 0.2 (Figure 3.36A). In comparison, the CSI based on NWS performance was

0.137. The objective method achieved a comparable CSI to the NWS performance at a POD of approximately 71% and an FAR of approximately 85%, while the POD and FAR based on NWS performance were approximately 54% and 84%, respectively. The mean lead time is 49.4 minutes using the objective method (10.5 minutes greater than the NWS), while the median lead time was 40 minutes (11 minutes greater).

Performance comparisons can also be made for varying storm environments, which is done here using the maximum NOAA Storm Prediction Center (SPC) Day 1 outlook for tornado risk. In particular, severe weather days are grouped by maximum SPC Day 1 tornado risks of 5%, 10%, 15%, and 30% or greater and the single-value upper-level divergence-rotation threshold from all days is applied to each (Figure 3.36B). For severe weather days with SPC Day 1 tornado risks less than 30%, the results are comparable to the 27-day performance comparison between the objective method and NWS warning-based method (i.e., similar CSI, higher POD, and longer lead times for the objective method). However, severe weather days with high tornado risk (30% or greater) show a substantial increase in skill (CSI) for the objective method, while also showing increases in POD and lead time compared to the NWS and in agreement with the 27-day performance comparison.

From the analysis of supercells versus non-supercells, improvements could perhaps be increased further by using different thresholds for different storm modes. Supercells generally have higher values for these updraft characteristics than even tornadic non-supercells, but there is still separation between tornadic and non-tornadic non-supercell storms. As a result, the POD for tornadoes from non-supercells could be lower than necessary or the FAR from supercells could be erroneously high. However, for the purpose of this study, a simple evaluation of the results was deemed sufficient. Future research that incorporates these results

in operational forecasts would likely utilize more advanced techniques, perhaps employing methods like machine learning and a more probabilistic approach.

3.3 Super Outbreak of April 2011

It was earlier mentioned that the Super Outbreak of April 2011 was excluded from the overall analyses due to being a very rare event accounting for a high percentage of the overall data. Additionally, it was a highly anticipated event, which may have led forecasters to perform differently than normal, i.e., warn most storms shortly after initiation, causing both a higher-than-usual POD and potentially, FAR. The analysis of tornadic and non-tornadic storms mirrors the analysis in Section 3.1, only the tornadic storms have generally higher values of the metrics (Figures 3.37-3.39). Further analyses were performed for short-term forecasts for the Super Outbreak alone, which show increased performance of the NWS warning-based method (slightly higher CSI and a large increase in POD compared to that in Figure 3.36B) and similar performance for the objective method compared to the 30% 1 Day tornado risk days, though with a slightly higher skill and lower FAR (Figure 3.40). The improvements for these storms, many of which produced tornadoes on the stronger end of the spectrum, in the objective method led to a hypothesis that stronger tornadoes may require stronger updrafts, which is explored in the next section.

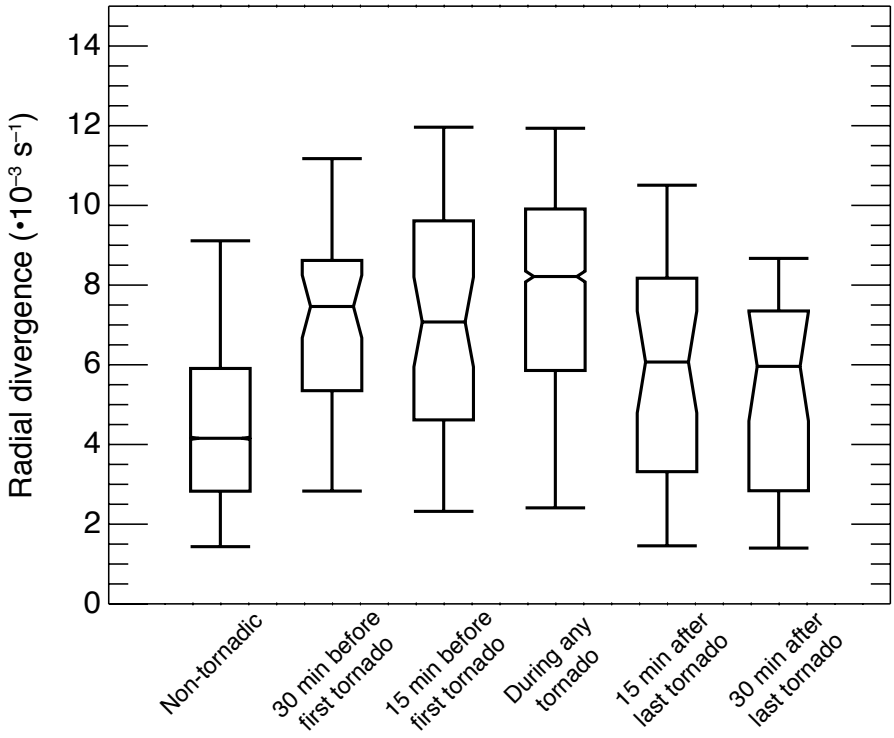

Figure 3.37: Box plot for maximum upper-level radar divergence for the Super Outbreak of April 2011.

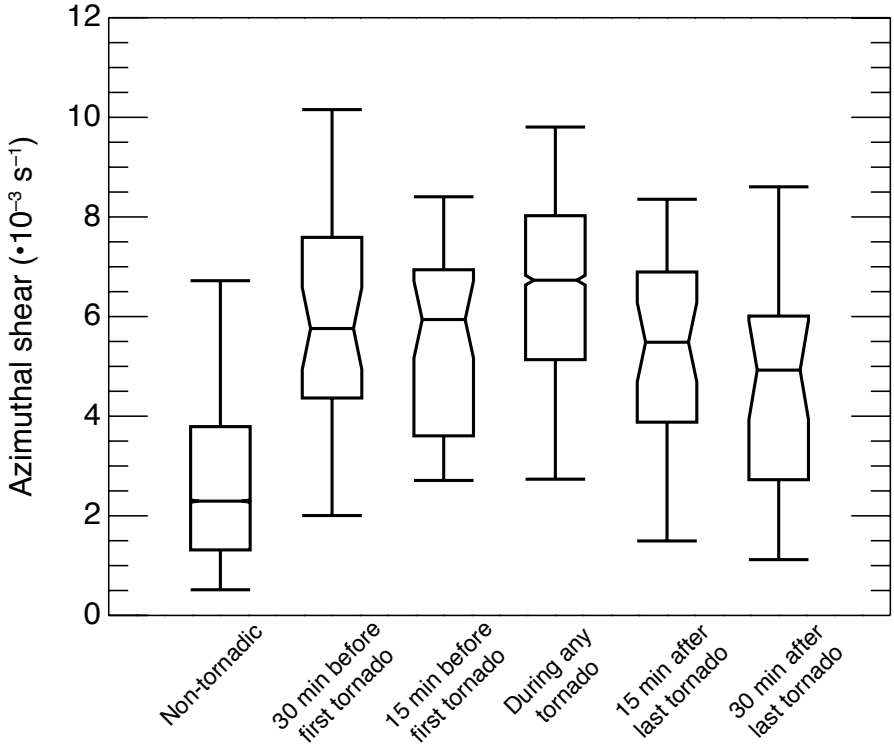

Figure 3.38: Box plot for maximum upper-level radar rotation for the Super Outbreak of April 2011.

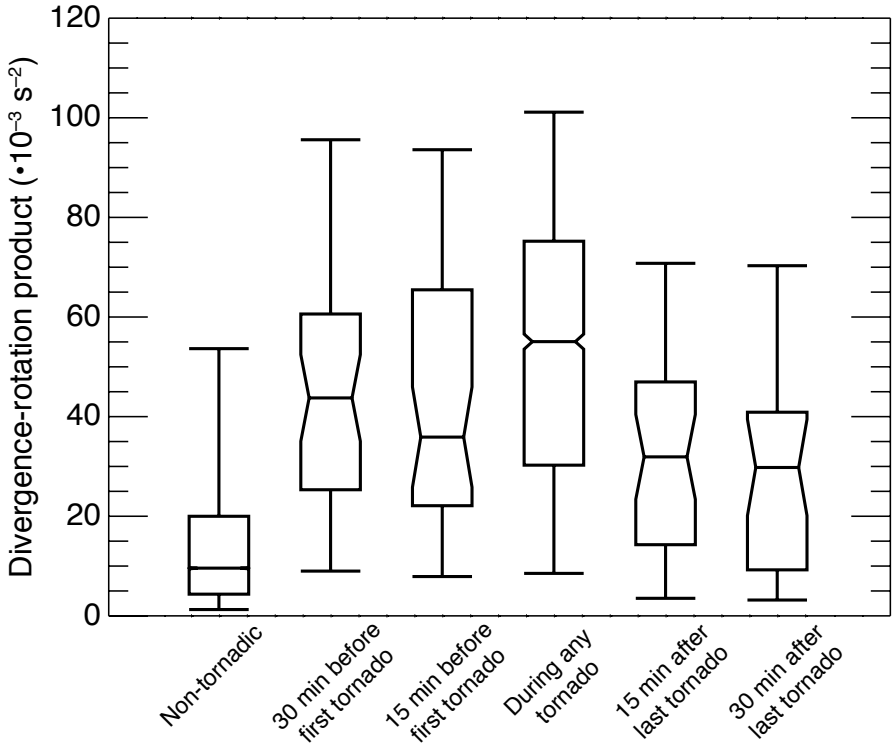

Figure 3.39: Box plot for divergence-rotation product for the Super Outbreak of April 2011.

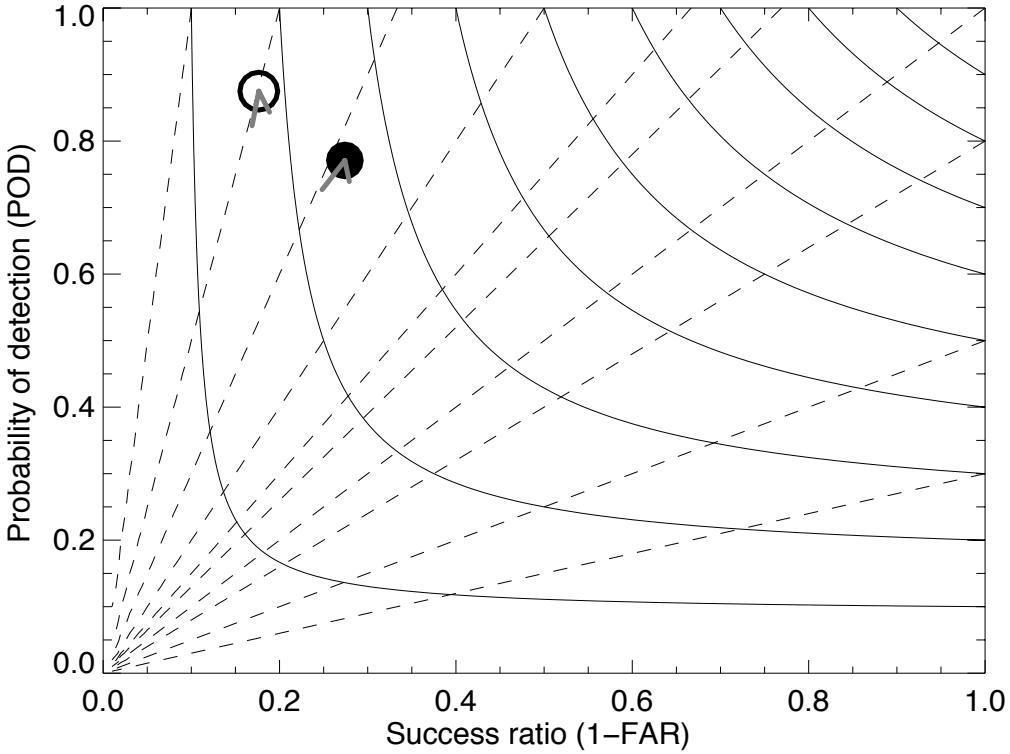

Figure 3.40: Performance diagram for the Super Outbreak of April 2011.

3.4 Tornado Strength

The storm-based analysis fundamental to this study was taken one step further by breaking down the tornadic storm category by the strength of the tornadoes to see if the strength could be predicted or detected indirectly. A few different approaches were investigated, including separating the storms by the strength of the strongest tornado associated with the storm and simply examining the different variables during the tornadoes of different intensity, the latter of which is presented here. Recently, the addition of the "unknown category" (EFU) for reported tornadoes has led to the exclusion of some tornadoes for this specific analysis, as some of the tornadoes in this study are of the category EFU (tornadic storms that only produced EFU tornadoes were not included in the non-tornadic category). In addition, only radar data was used in this section due to insufficient satellite data for the older cases, when the majority of the stronger tornadoes occurred. Due to limited data for EF4 and EF5 tornadoes, the Super Outbreak of April 2011 is included in this analysis.

In Figures 3.41 to 3.53, the leftmost box still represents the full lifetime of the non-tornadic storms. The remaining boxes represent the different variables when the tornado of the denoted strength is occurring, from EF0 on the left increasing to EF5 on the right. The number of data points used to create each box is listed in Table 3.3.

The maximum upper-level radar divergence is mostly the same for EF0 to EF2 tornadoes, with a shallow dip in magnitude for EF1 tornadoes (Figure 3.41). It was hypothesized that this dip would be mostly due to non-supercellular tornadoes, which could be evaluated by isolating the supercells. Figure 3.42 shows the radar divergence for supercells only, where the three lowest categories of tornadoes are now more similar. Further examining Figure 3.41, it is evident that the EF3 to EF5 tornadoes generally have higher values of upper-level divergence than the

weaker tornadoes. The median upper-level divergence is gradually increasing with tornado strength for the stronger half of the tornado categories, and the data for each category is less variable, which is especially clear for EF5 tornadoes.

Table 3.3: Number of data points per box in box plots for tornado strength.

Figure	Non-tornadic	EF0	EF1	EF2	EF3	EF4	EF5
3.41	303460	1605	2372	1663	1518	906	270
3.42	29534	1327	1749	1242	1262	906	270
3.43	246632	1386	2181	1532	1376	859	270
3.44	313999	1631	2498	1739	1535	906	270
3.45	29613	1331	1755	1249	1262	906	270
3.46	313621	1631	2498	1739	1535	906	270
3.47	302597	1622	2459	1674	1444	906	270
3.48	302597	1622	2459	1674	1444	906	270
3.49	215935	1494	2128	1520	1397	901	270
3.50	242518	1544	2210	1611	1487	906	270
3.51	272404	1550	2316	1608	1435	871	270
3.52	247158	1409	2187	1538	1376	859	270
3.53	222511	899	1266	820	697	331	32

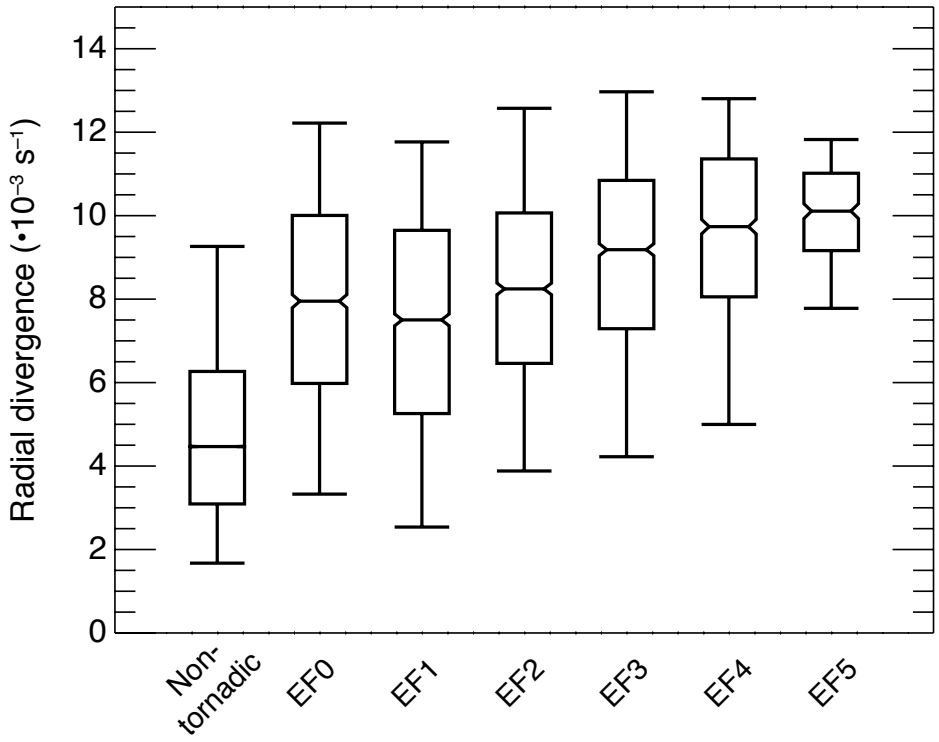

Figure 3.41: Tornado strength box plot for maximum upper-level radar divergence.

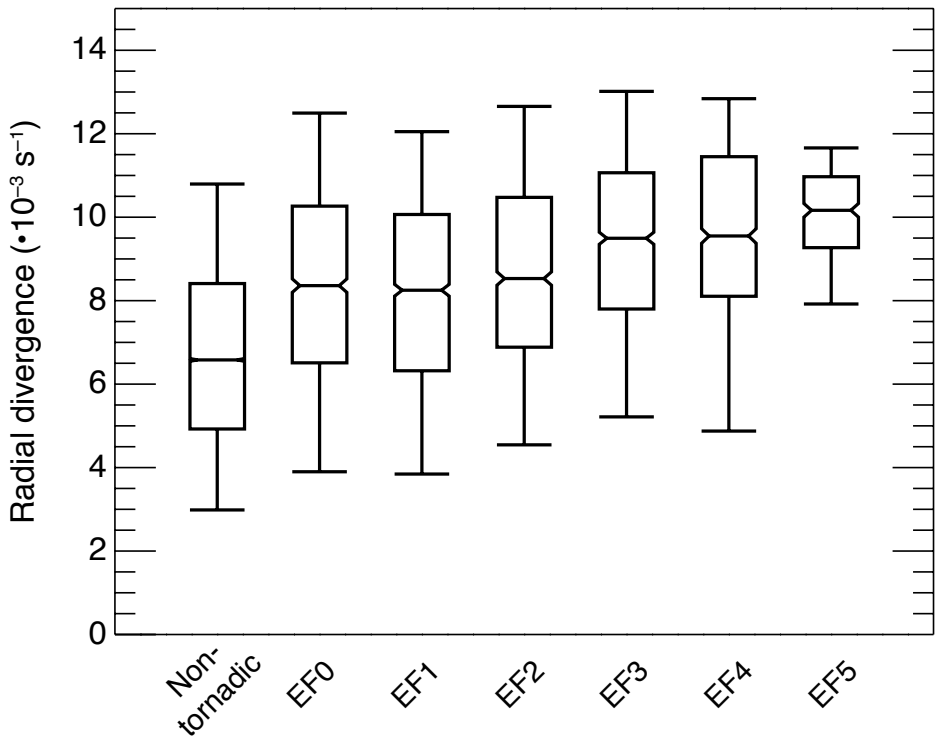

Figure 3.42: Tornado strength box plot for maximum upper-level radar divergence, supercells only.

When repeated for low-level convergence maximum, the analysis shows much less meaningful results (Figure 3.43). Although there is a tiny uptick in the peak value of convergence with increasing tornado strength, it is not as prominent as the difference in convergence between tornadic and non-tornadic storms.

40-dBZ echo-top altitudes in Figure 3.44 show a similar tendency to the upper-level divergence, though the slightly larger separation between the non-tornadic storms and the tornadic periods seen in the previous analysis is also apparent in Figures 3.41 and 3.44. There is a greater separation between the E4+ tornadoes and the rest for 40 dBZ echo-top altitude, and the dip for the EF1 tornadoes remains. Again, isolating the supercells it seems the negative bias in EF1 tornadoes is mostly gone for the 5th, 25th, and 50th percentiles, indicating that non-supercellular tornadoes might require a less strong updraft than their supercellular counterparts (Figure 3.45).

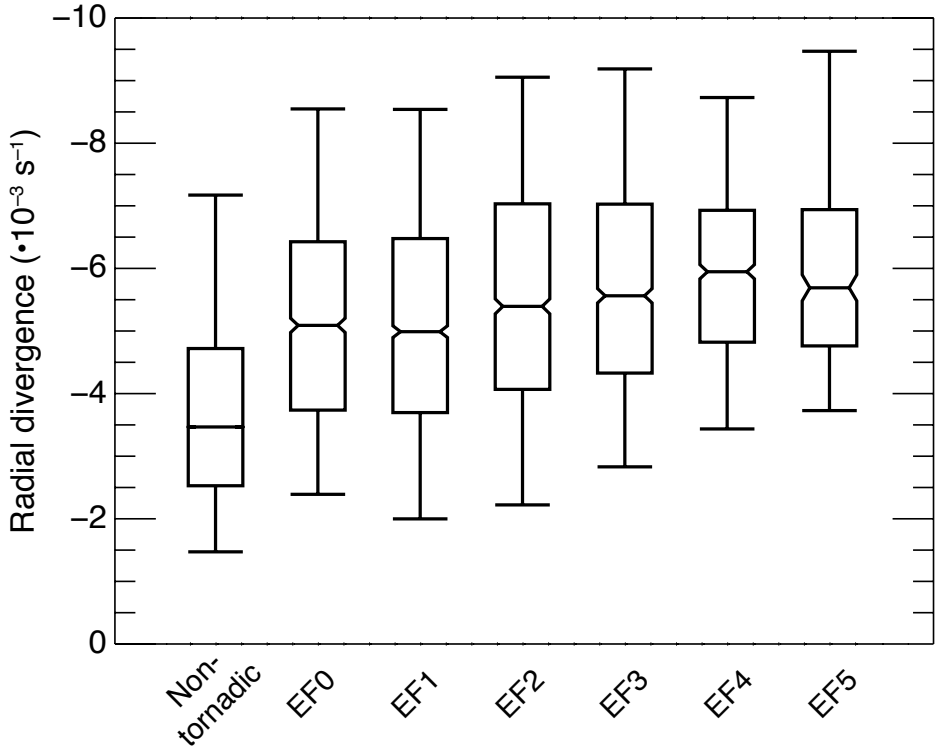

Figure 3.43: Tornado strength box plot for maximum low-level radar convergence.

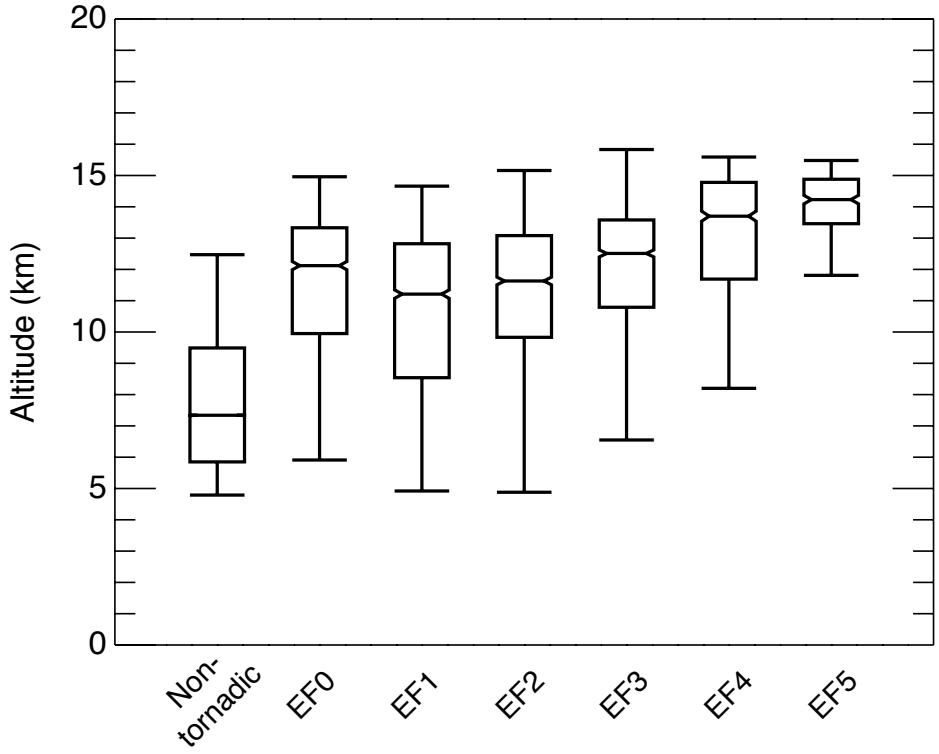

Figure 3.44: Tornado strength box plot for maximum 40-dBZ echo-top altitude.

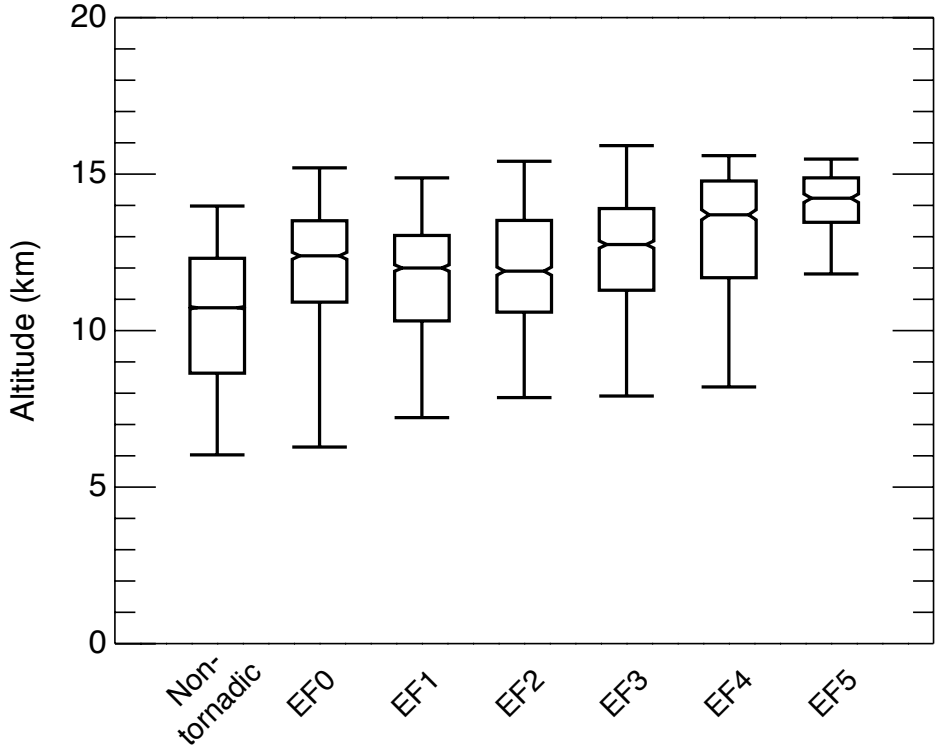

Figure 3.45: Tornado strength box plot for maximum 40-dBZ echo-top altitude, supercells only.

Column-maximum spectrum width shows a nearly identical tendency to the upper-level divergence (Figure 3.46).

Confirming what most of the updraft-related metrics have been showing, the maximum and median implied ascent from the divergence profile depict the same increasing relationship between upward motion and tornado strength (Figures 3.47 and 3.48).

The width of the updraft has recently been hypothesized to be related to tornado strength (Trapp et al., 2017), and it is shown here that this holds true for observations from radar. The upper limit due to calculation restrictions described before prevents much change in the 95th percentile, but the median ascent area magnitude shows a significant increase in updraft width with increasing tornado strength (Figure 3.49).

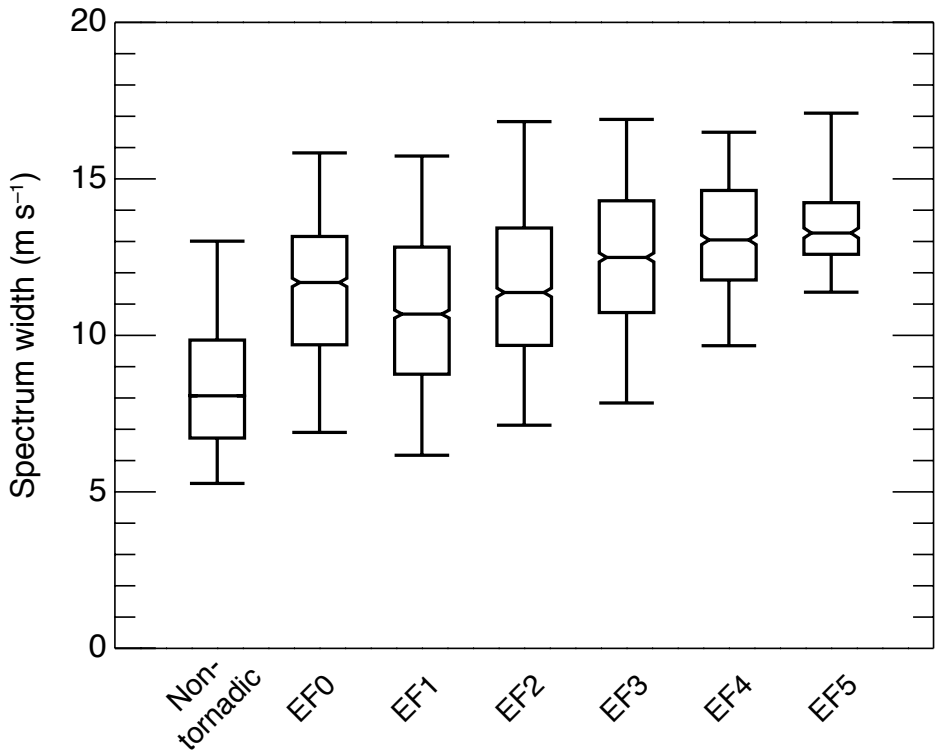

Figure 3.46: Tornado strength box plot for column-maximum spectrum width.

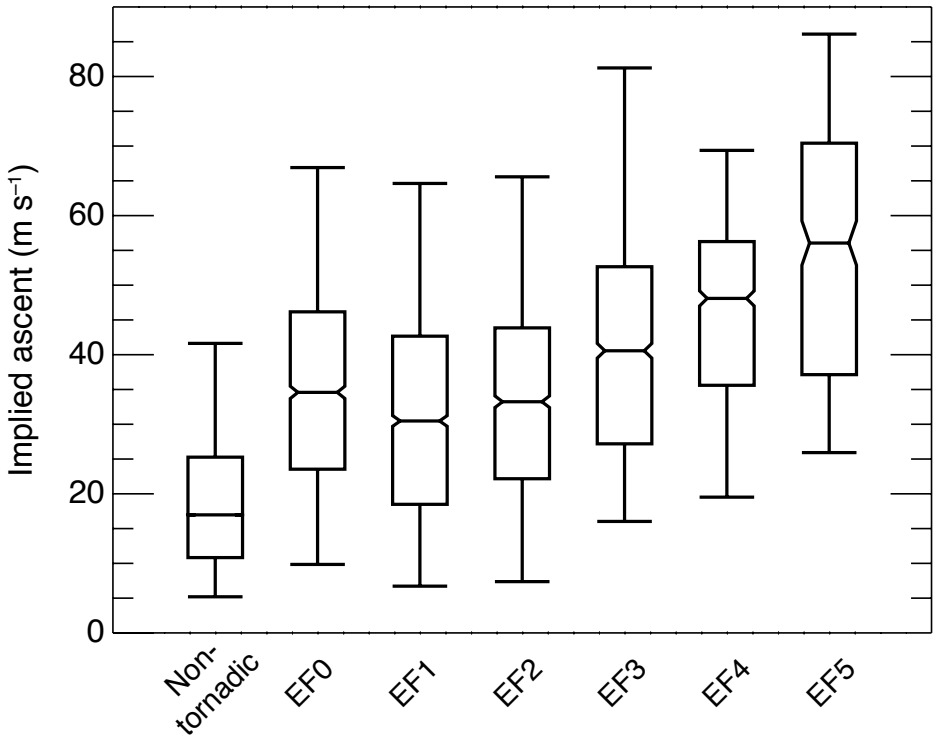

Figure 3.47: Tornado strength box plot for maximum implied ascent from divergence.

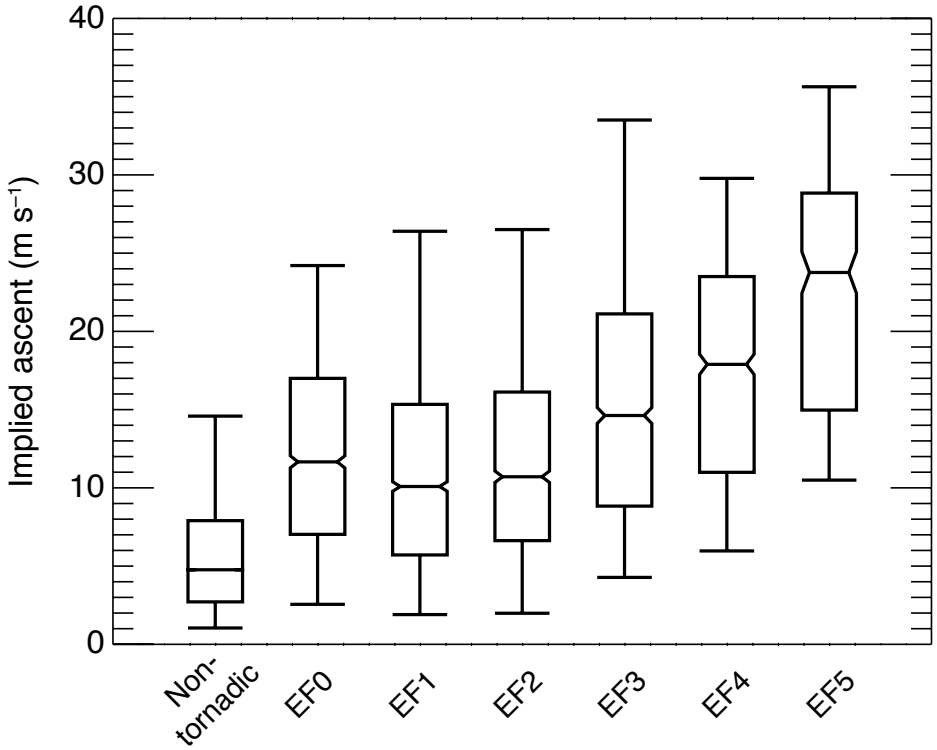

Figure 3.48: Tornado strength box plot for median implied ascent from divergence.

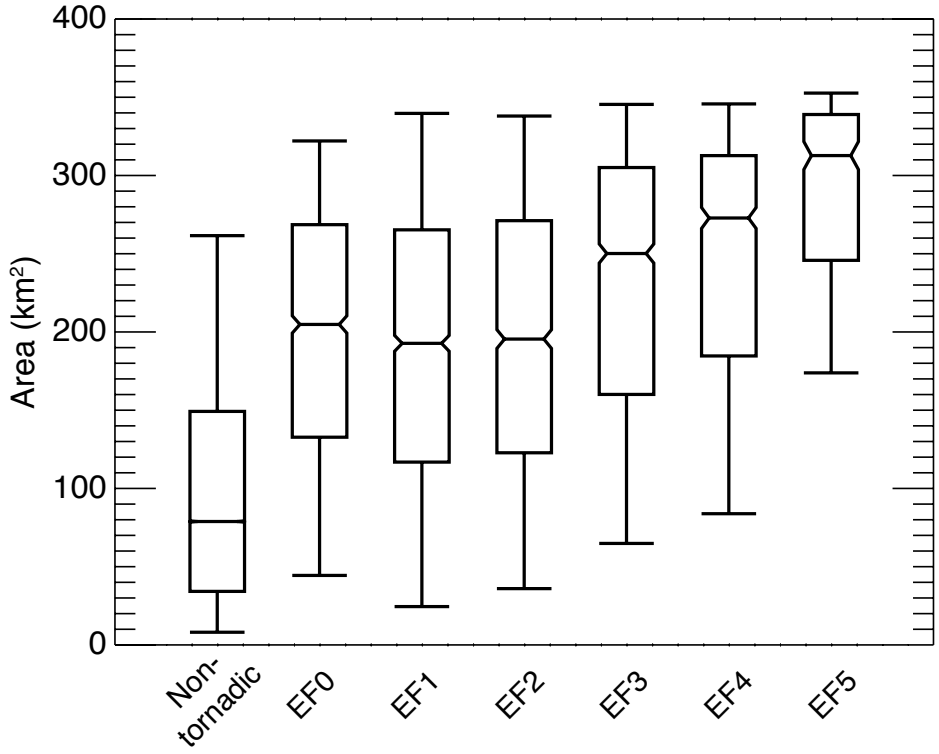

Figure 3.49: Tornado strength box plot for area of implied ascent ≥ 10 m s^{-1} from divergence.

Stronger rotation is associated with stronger tornadoes (Figures 3.50, 3.51, and 3.52). Rotation seems to be less affected by storm type than the updraft-related characteristics, as there is no pronounced dip in the increasing tendency with tornado intensity for EF1 tornadoes. The increase is roughly even for the low-level rotation, while the mid- and upper-level rotation show more separation between EF4+ tornadoes and the rest.

Of the polarimetric variables, correlation coefficient is the only variable that shows any difference in the values for the different tornado strengths (Figure 3.53). Since the data is being evaluated during the tornadoes, the lower ρ_{HV} is likely a debris signature within otherwise meteorological echo exceeding the 45-dBZ threshold used in this analysis. The values during EF5 tornadoes may be extra low due to these tornadoes' ability to lift non-meteorological items capable of producing

echoes exceeding 45 dBZ alone, which removes the need for the debris to be within the meteorological echo in order to be detected.

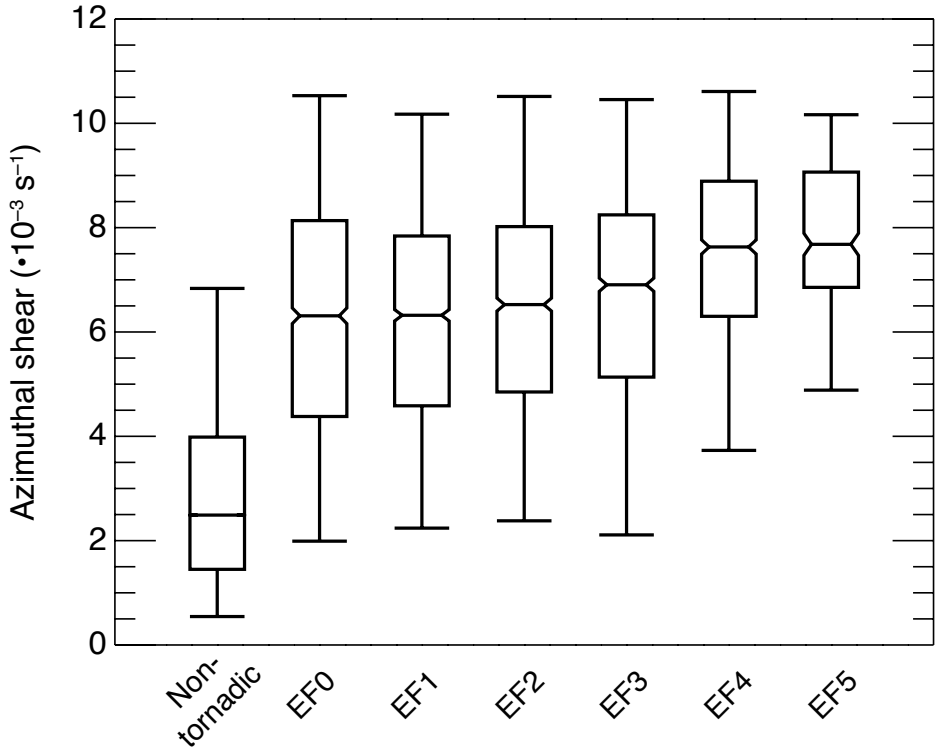

Figure 3.50: Tornado strength box plot for upper-level rotation from radar.

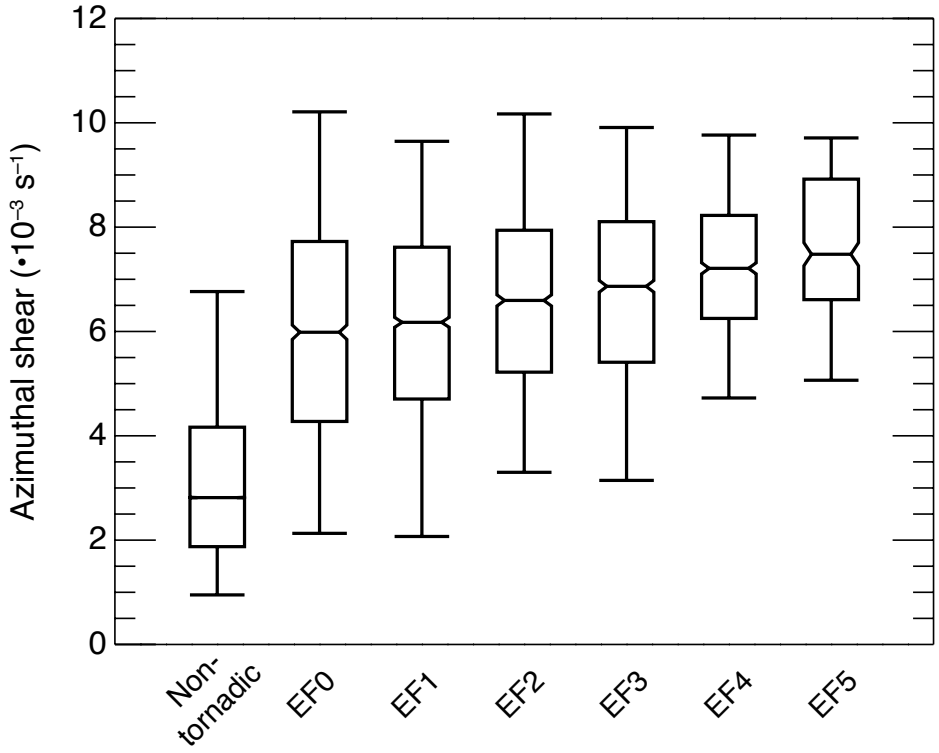

Figure 3.51: Tornado strength box plot for mid-level rotation from radar.

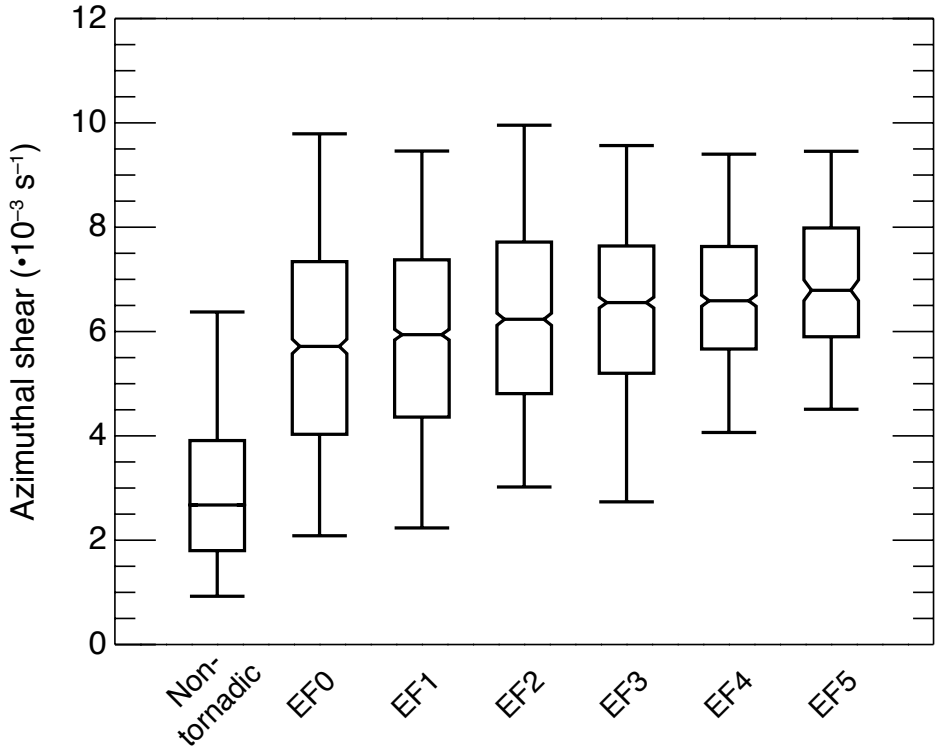

Figure 3.52: Tornado strength box plot for low-level rotation from radar.

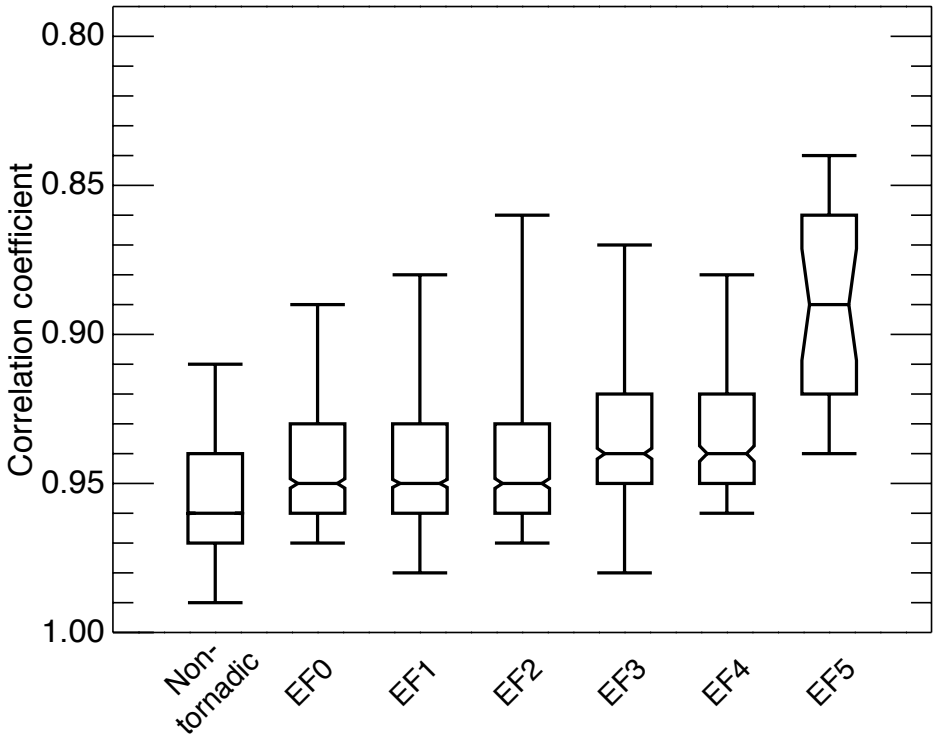

Figure 3.53: Tornado strength box plot for correlation coefficient.

Chapter 4

Summary and Conclusions

Indicators of strong updrafts and rotation are more prominent for tornadic storms than for non-tornadic storms, especially prior to tornadogenesis and during the tornado. This holds true when examining supercells and non-supercells separately, though the differences are slightly less pronounced. While these results are consistent for both radar and satellite variables, larger differences are seen in the radar variables with the instruments used in this study. The separation between the tornadic and non-tornadic storms is significant enough that a simple objective threshold method used to provide a short-term forecast of tornadogenesis is able to perform comparatively to a short-term forecast based on the NWS tornado warnings (i.e., equivalent skill) with higher POD and lead times. Both the separate analysis of the Super Outbreak of April 2011 and the analysis of the different SPC Day 1 tornado risks indicate that metrics of upward motion show more separation between the tornadic and non-tornadic storm populations when the environment has been deemed more favorable for severe storms. The tornadic storms with the strongest and widest updrafts produce the strongest tornadoes on the EF-scale. In addition, the updraft rotation is more powerful for the most intense tornadoes.

The results of this study agree with the current understanding of tornadogenesis within supercells (Markowski and Richardson, 2009; Davies-Jones, 2015). Leading up to a tornado, a mid-level storm circulation develops, followed by a low-level

circulation induced by strong downward motion, which in turn increases the low-level updraft from the resulting in-storm pressure perturbations. The strength of this low-level updraft is what allows a tornado to form through vertical stretching of the air and intensification of low-level rotation. The strong, rotating updraft inferred from upper-level radar and satellite observations of tornadic storms in this study is evidence of the deep rotating updraft associated with the mid-level circulation in the conceptual model. In addition, the increases in inferred updraft strength observed in the time leading up to tornadogenesis at upper-levels may be a vertical extension of the intensification of the low-level updraft. It is possible that vertically-stacked low- and mid-level updrafts and associated rotation also support these signals. However, it is not yet known what factors within the near-storm environment or storms themselves lead to the observed differences in inferred upward motion, but currently used environmental metrics for the 27 severe weather days analyzed here, such as CAPE and effective bulk wind shear (the difference between the horizontal wind at cloud base and that at half the distance to cloud top), show considerable overlap (Figure 4.1). This limited understanding is the primary challenge for improving forecasts of tornadic storms hours to days in advance.

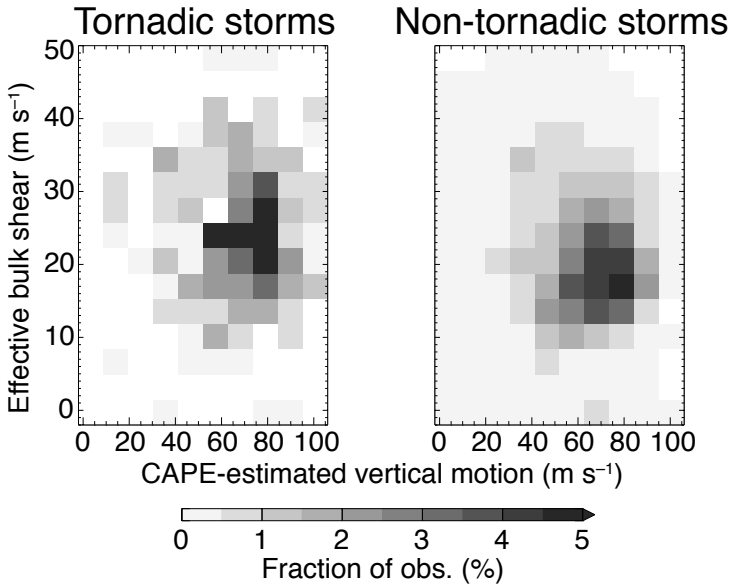

Figure 4.1: Covariation of effective bulk wind shear and CAPE-estimated maximum vertical motion for tornadic and non-tornadic storms.

It is surprising that upper-level rotation and divergence have not provided a better distinction of tornadic storms from non-tornadic storms in the past, especially for supercells. Many previous studies have been limited to a small number of storms (<10) and only considered the time variations within the tornadic storms, which was explored and found to be of little value in this study (e.g., Van Den Broeke, 2017). The size of the storm sample analyzed here may be one reason why this difference was revealed. Others have used either single-radar observations or composites that were generated differently than the GridRad composites, so perhaps the way the wind derivatives are calculated in these composites provide a better picture of these variables than that available to prior studies (e.g., Parker, 2014). It is more likely, however, that the large number of storms and resulting population statistics summarized here were key to reaching these conclusions.

An updraft of a certain strength seems to be a necessary condition for tornadogenesis, and stronger updrafts can produce more intense tornadoes. The same argument is made for the width of the updraft, which Trapp et al. (2017) tied to the strength of the mesocyclone and in turn to tornado strength for simulated storms. Trapp et al. (2017) discussed the swirl ratio in relation to the updraft width, where the swirl ratio increases with increasing updraft width and a strong swirl ratio is needed for stronger tornadoes, and it seems that this reasoning could be extended to weak tornadoes versus no tornadoes. The strong updraft contributes to more tilting of horizontal vorticity into vertical vorticity, which is needed for tornadoes to develop, as well as the stretching of the vertical vorticity near the ground in the later stages of tornadogenesis. The upper-level rotation measured within a tornadic storm distinguishes itself from that of a non-tornadic storm earlier than the low-level rotation, possibly indicating that the process starts in the upper-levels and later extends down in agreement with that found in simulations by Markowski et al. (2003). What is often brought up in the discussion of tornadogenesis that

was not investigated here is the role of the downdraft in forcing preexisting rotation in the lower-levels to extend to the ground to create a tornado (Markowski and Richardson, 2009). Future studies should evaluate the potential of an analogous implied descent product to provide a pathway for identifying time-evolving characteristics prior to tornadogenesis.

In conclusion, multiple dynamical and physical metrics of the strength of upward motion in storms from ground-based weather radar and satellite imagery show that tornadic storms have stronger inferred upward motion than non-tornadic storms. A simple objective threshold technique using the radar observations can match the skill of a NOAA NWS tornado warning-based short-term forecast, while increasing the POD to approximately 71% and lead time to approximately 49 minutes on average. These findings provide an opportunity for improving the forecaster decision-making process used when issuing tornado warnings and, hopefully, saving lives. Increases in the spatial and temporal resolution of visible and IR satellite imagery as GOES-16 becomes operational in November 2017 will likely provide additional value to this process.

Bibliography

Anderson, C. J., C. K. Wikle, Q. Zhou, and J. A. Royle, 2007: Population influences on tornado reports in the United States. *Wea. Forecasting*, **22 (3)**, 571–579.

Anderson-Frey, A. K., Y. P. Richardson, A. R. Dean, R. L. Thompson, and B. T. Smith, 2016: Investigation of near-storm environments for tornado events and warnings. *Wea. Forecasting*, **31 (6)**, 1771–1790.

Apke, J. M., J. R. Mecikalski, and C. P. Jewett, 2016: Analysis of mesoscale atmospheric flows above mature deep convection using super rapid scan geostationary satellite data. *J. Appl. Meteor. Climatol.*, **55 (9)**, 1859–1887, doi: 10.1175/JAMC-D-15-0253.1.

Balakrishnan, N., and D. S. Zrnić, 1990: Use of polarization to characterize precipitation and discriminate large hail. *J. Atmos. Sci.*, **47**, 1525–1540.

Barnes, S. L., 1973: Mesoscale objective map analysis using weighted time-series observations. NOAA Tech. Memo ERL NSSL-62, NOAA, National Severe Storms Laboratory, Norman, OK. [NTISCOM-73-10781].

Bedka, K. M., and K. Khlopenkov, 2016: A probabilistic multispectral pattern recognition method for detection of overshooting cloud tops using passive satellite imager observations. *J. Appl. Meteor. Climatol.*, **55 (9)**, 1983–2005.

Bedka, K. M., and J. R. Mecikalski, 2005: Application of satellite-derived atmospheric motion vectors for estimating mesoscale flows. *J. Appl. Meteor.*, **44 (11)**, 1761–1772.

Bedka, K. M., C. Wang, R. Rogers, L. D. Carey, W. Feltz, and J. Kanak, 2015: Examining deep convective cloud evolution using total lightning, WSR-88D, and GOES-14 super rapid scan datasets. *Wea. Forecasting*, **30**, 571–590, doi: 10.1175/WAF-D-14-00062.1.

Bluestein, H. B., 2013: *Severe convective storms and tornadoes: Observations and dynamics*. Springer, 456 pp.

Brooks, H., and J. Correia, Jr., 2016: Warnings (tornado) facts: Considerations, reflections, and perspectives on 30 years of warning performance metrics in the NWS. *28th Conf. on Severe Local Storms*, Portland, OR, Amer.

Meteor. Soc., 11.5, [Available online at https://ams.confex.com/ams/28SLS/webprogram/Paper298260.html.].

Browning, K., 1965: Some inferences about the updraft within a severe local storm. *J. Atmos. Sci.*, **22 (6)**, 669–677.

Browning, K. A., and R. J. Donaldson, 1963: Airflow and structure of a tornadic storm. *J. Atmos. Sci.*, **20 (6)**, 533–545.

Burgess, D. W., L. R. Lemon, and R. A. Brown, 1975: Tornado characteristics revealed by doppler radar. *Geophys. Res. Lett.*, **2 (5)**, 183–184.

Cintineo, J. L., M. J. Pavolonis, J. M. Sieglaff, and A. K. Heidinger, 2013: Evolution of severe and nonsevere convection inferred from GOES-derived cloud properties. *J. App. Met. Clim.*, **52**, 2009–2023, doi:10.1175/JAMC-D-12-0330.1.

Cintineo, J. L., M. J. Pavolonis, J. M. Sieglaff, and D. T. Lindsey, 2014: An empirical model for assessing the severe weather potential of developing convection. *Wea. Forecasting*, **29 (3)**, 639–653, doi:10.1175/WAF-D-13-00113.1.

Crum, T. D., and R. L. Alberty, 1993: The WSR-88D and the WSR-88D operational support facility. *Bull. Amer. Meteorol. Soc.*, **74 (9)**, 1669–1687.

Davies-Jones, R., 1984: Streamwise vorticity: The origin of updraft rotation in supercell storms. *J. Atmos. Sci.*, **41 (20)**, 2991–3006.

Davies-Jones, R., 2015: A review of supercell and tornado dynamics. *Atmos. Res.*, **158**, 274–291.

Deierling, W., and W. A. Petersen, 2008: Total lightning activity as an indicator of updraft characteristics. *J. Geophys. Res.*, **113**, D16 210, doi:10.1029/2007JD009598.

Doswell, C. A., and D. W. Burgess, 1993: *Tornadoes and Tornadic Storms: A Review of Conceptual Models*, 161–172. American Geophysical Union, doi:10.1029/GM079p0161, URL http://dx.doi.org/10.1029/GM079p0161.

Doswell III, C. A., A. R. Moller, and H. E. Brooks, 1999: Storm spotting and public awareness since the first tornado forecasts of 1948. *Wea. Forecasting*, **14 (4)**, 544–557.

Doviak, R. J., and D. S. Zrnić, 1993: *Doppler Radar and Weather Observations*. 2nd ed., ISBN 0-486-45060-0, Dover Publications, Inc., 31 East 2nd Street, Mineola, NY, 11501.

Dworak, R., K. Bedka, J. Brunner, and W. Feltz, 2012: Comparison between GOES-12 overshooting-top detections, WSR-88D radar reflectivity, and severe storm reports. *Wea. Forecasting*, **27**, 684–699, doi:10.1175/WAF-D-11-00070.1.

Elsner, J. B., L. E. Michaels, K. N. Scheitlin, and I. J. Elsner, 2013: The decreasing population bias in tornado reports across the central Plains. *Weather, Climate, and Society*, **5 (3)**, 221–232.

Feist, M. M., C. D. Westbrook, P. Clark, T. Stein, H. W. Lean, and A. Stirling, 2017: Estimating convective storm turbulence with radar to evaluate the paramerisation of turbulence in NWP models. *38th Conf. on Radar Meteorology*, Chicago, IL, Amer. Meteor. Soc., 68, [Available online at https://ams.confex.com/ams/38RADAR/webprogram/Paper321071.html.].

Forbes, G. S., 1981: On the reliability of hook echoes as tornado indicators. *Mon. Wea. Rev.*, **109 (7)**, 1457–1466.

Fujita, T., 1958: Mesoanalysis of the Illinois tornadoes of 9 April 1953. *J. Meteor.*, **15 (3)**, 288–296.

Garrett, R., and V. D. Rockney, 1962: Tornadoes in northeastern Kansas, May 19, 1960. *Mon. Wea. Rev.*, **90 (6)**, 231–240.

Gravelle, C. M., J. R. Mecikalski, W. E. Line, K. M. Bedka, R. A. Petersen, J. M. Sieglaff, G. T. Stano, and S. J. Goodman, 2016: Demonstration of a GOES-R satellite convective toolkit to "bridge the gap" between severe weather watches and warnings: An example from the 20 May 2013 Moore, Oklahoma, tornado outbreak. *Bull. Amer. Meteor. Soc.*, **97 (1)**, 69–84.

Hayden, C. M., and R. J. Purser, 1995: Recursive filter objective analysis of meteorological fields: Applications to NESDIS operational processing. *J. Appl. Meteor.*, **34 (1)**, 3–15.

Helmus, J., and S. Collis, 2016: The Python ARM Radar Toolkit (Py-ART), a library for working with weather radar data in the Python programming language. *Journal of Open Research Software*, **4 (1)**.

Heymsfield, G. M., and R. H. Blackmer Jr, 1988: Satellite-observed characteristics of Midwest severe thunderstorm anvils. *Mon. Wea. Rev.*, **116 (11)**, 2200–2224.

Homeyer, C. R., 2014: Formation of the Enhanced-V infrared cloud top feature from high-resolution three-dimensional radar observations. *J. Atmos. Sci.*, **71**, 332–348, doi:10.1175/JAS-D-13-079.1.

Homeyer, C. R., J. D. McAuliffe, and K. M. Bedka, 2017: On the development of above-anvil cirrus plumes in extratropical convection. *J. Atmos. Sci.*, **74 (5)**, 1617–1633.

Hubert, L. F., and L. F. Whitney, 1971: Wind estimation from geostationary satellite pictures. *Mon. Wea. Rev.*, **99**, 665–672.

Klemp, J. B., 1987: Dynamics of tornadic thunderstorms. *Annual review of fluid mechanics*, **19 (1)**, 369–402.

Krzywinski, M., and N. Altman, 2014: Points of significance: Visualizing samples with box plots. *Nature Methods*, **11 (2)**, 119–120.

Kumjian, M. R., A. P. Khain, N. Benmoshe, E. Ilotoviz, A. V. Ryzhkov, and V. T. J. Phillips, 2014: The anatomy and physics of $Z_{\rm DR}$ columns: Investigating a polarimetric radar signature with a spectral bin microphysical model. *J. App. Met. Clim.*, **53**, 1820–1843, doi:10.1175/JAMC-D-13-0354.1.

Lemon, L. R., and C. A. Doswell III, 1979: Severe thunderstorm evolution and mesocyclone structure as related to tornadogenesis. *Mon. Wea. Rev.*, **107 (9)**, 1184–1197.

Line, W. E., T. J. Schmit, D. T. Lindsey, and S. J. Goodman, 2016: Use of geostationary super rapid scan satellite imagery by the Storm Prediction Center. *Wea. Forecasting*, **31 (2)**, 483–494.

Liu, C., and S. Heckman, 2011: The application of total lightning detection and cell tracking for severe weather prediction. *WMO Technical Conference on Instruments and Methods of Observation (TECO-2010)*.

Markowski, P. M., and Y. P. Richardson, 2009: Tornadogenesis: Our current understanding, forecasting considerations, and questions to guide future research. *Atmos. Res.*, **93 (1)**, 3–10.

Markowski, P. M., J. M. Straka, and E. N. Rasmussen, 2003: Tornadogenesis resulting from the transport of circulation by a downdraft: Idealized numerical simulations. *J. Atmos. Sci.*, **60 (6)**, 795–823.

McCann, D. W., 1983: The Enhanced-V: A satellite observable severe storm signature. *Mon. Wea. Rev.*, **111**, 887–894.

Mecikalski, J. R., K. M. Bedka, S. J. Paech, and L. A. Litten, 2008: A statistical evaluation of goes cloud-top properties for nowcasting convective initiation. *Mon. Wea. Rev.*, **136 (12)**, 4899–4914.

Menzel, W. P., and J. F. W. Purdom, 1994: Introducing GOES-I: The first of a new generation of geostationary operational environmental satellites. *Bull. Amer. Meteorol. Soc.*, **75 (5)**, 757–781.

Nelson, S. P., 1983: The influence of storm flow structure on hail growth. *J. Atmos. Sci.*, **40 (8)**, 1965–1983.

O'Brien, J. J., 1970: Alternative solutions to the classical vertical velocity problem. *J. Appl. Meteor.*, **9 (2)**, 197–203.

Parker, M. D., 2014: Composite VORTEX2 supercell environments from near-storm soundings. *Mon. Wea. Rev.*, **142 (2)**, 508–529.

Przybylinski, R. W., 1995: The bow echo: Observations, numerical simulations, and severe weather detection methods. *Wea. Forecasting*, **10 (2)**, 203–218.

Radová, M., and J. Seidl, 2008: Parallax applications when comparing radar and satellite data. *The 2008 EUMETSAT Meteorological Satellite Conference.*

Reynolds, D. W., 1980: Observations of damaging hailstorms from geosynchronous satellite digital data. *Mon. Wea. Rev.*, **108 (3)**, 337–348.

Ryzhkov, A. V., T. J. Schuur, D. W. Burgess, and D. S. Zrnić, 2005: Polarimetric tornado detection. *J. Appl. Meteor.*, **44 (5)**, 557–570.

Schmit, T. J., M. M. Gunshor, W. P. Menzel, J. J. Gurka, J. Li, and A. S. Bachmeier, 2005: Introducing the next-generation Advanced Baseline Imager on GOES-R. *Bull. Amer. Meteor. Soc.*, **86 (8)**, 1079–1096.

Schmit, T. J., and Coauthors, 2013: Geostationary operational environmental satellite GOES-14 super rapid scan operations to prepare for GOES-R. *Journal of Applied Remote Sensing*, **7 (1)**, 073 462–073 462.

Schultz, C. J., W. A. Petersen, and L. D. Carey, 2009: Preliminary development and evaluation of lightning jump algorithms for the real-time detection of severe weather. *J. Appl. Meteor. Climatol.*, **48 (12)**, 2543–2563.

Smith, T. M., and Coauthors, 2016: Multi-Radar Multi-Sensor (MRMS) severe weather and aviation products: Initial operating capabilities. *Bull. Amer. Meteor. Soc.*, **97 (9)**, 1617–1630.

Starzec, M., C. R. Homeyer, and G. L. Mullendore, 2017: Storm labeling in three dimensions (SL3D): A volumetric radar echo and dual-polarization updraft classification algorithm. *Mon. Wea. Rev.*, **145 (3)**, 1127–1145.

Stensrud, D. J., and Coauthors, 2009: Convective-scale Warn-on-Forecast system: A vision for 2020. *Bull. Amer. Meteor. Soc.*, **90 (10)**, 1487–1499.

Stensrud, D. J., and Coauthors, 2013: Progress and challenges with Warn-on-Forecast. *Atmos. Res.*, **123**, 2–16.

Stout, G., and F. Huff, 1953: Radar records Illinois tornadogenesis. *Bull. Amer. Meteor. Soc.*, **34**, 281–284.

Thompson, R. L., R. Edwards, J. A. Hart, K. L. Elmore, and P. Markowski, 2003: Close proximity soundings within supercell environments obtained from the rapid update cycle. *Wea. Forecasting*, **18 (6)**, 1243–1261.

Trapp, R. J., G. R. Marion, and S. W. Nesbitt, 2017: The regulation of tornado intensity by updraft width. *J. Atmos. Sci.*, doi:10.1175/JAS-D-16-0331.1.

Van Den Broeke, M. S., 2017: Polarimetric radar metrics related to tornado life cycles and intensity in supercell storms. *Mon. Wea. Rev.*, **145 (9)**, 3671–3686.

Wakimoto, R. M., and J. W. Wilson, 1989: Non-supercell tornadoes. *Mon. Wea. Rev.*, **117 (6)**, 1113–1140.

Wexler, R., and R. H. Blackmer Jr, 1982: Radar reflectivities and satellite imagery of severe storms 20 May 1977. *Mon. Wea. Rev.*, **110 (7)**, 719–724.

Williams, E., and Coauthors, 1999: The behavior of total lightning activity in severe Florida thunderstorms. *Atmos. Res.*, **51 (3)**, 245–265.

Xu, X., M. Xue, and Y. Wang, 2015: The genesis of mesovortices within a real-data simulation of a bow echo system. *J. Atmos. Sci.*, **72 (5)**, 1963–1986.